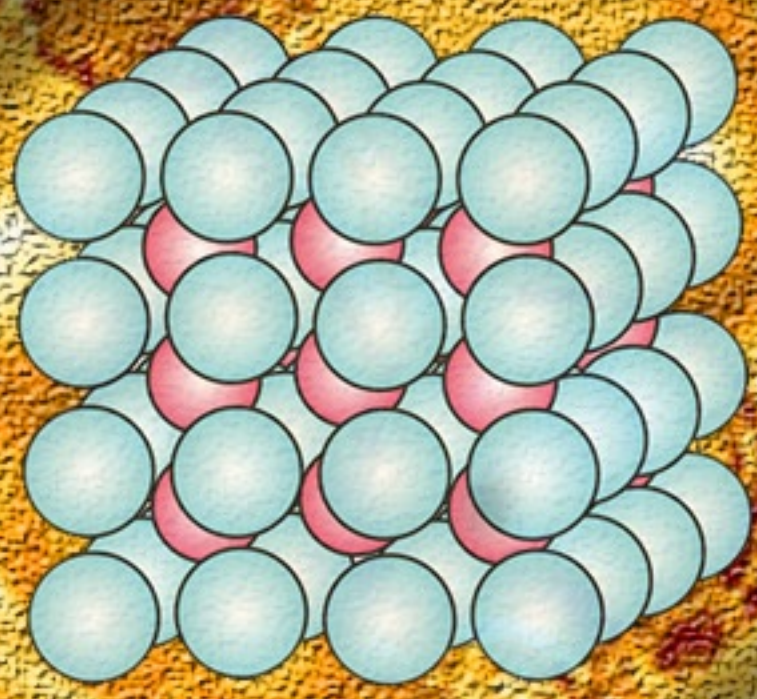
INTERNATIONAL SCIENTIFIC JOURNAL

"MATERIAL SCIENCE"



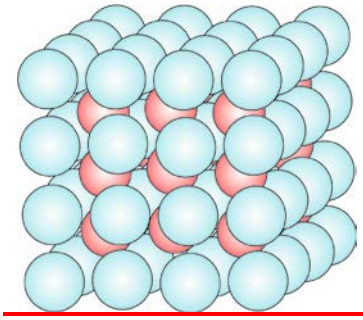
„NONEQUILIBRIUM PHASE TRANSFORMATIONS"

YEAR VII, ISSUE 2/2021

ISSN PRINT 2367-749X
ISSN WEB 2534-8477

PUBLISHER: SCIENTICIC TECHNICAL UNION OF MECHANICAL ENGINEERING INDUSTRY 4.0

108 Rakovski str., 1000 Sofia, Bulgaria
tel./fax (+359 2) 986 22 40, tel. (+359 2) 987 72 90,
office@stumejournals.com, www.stumejournals.com



INTERNATIONAL SCIENTIFIC JOURNAL

MATERIALS SCIENCE. NON-EQUILIBRIUM PHASE TRANSFORMATIONS

PUBLISHER:

SCIENTIFIC TECHNICAL UNION OF MECHANICAL ENGINEERING "INDUSTRY 4.0"

108, Rakovski Str., 1000 Sofia, Bulgaria
tel. (+359 2) 987 72 90,
tel./fax (+359 2) 986 22 40,
office@stumejournals.com

ISSN PRINT 2367-749X, ISSN WEB 2534-8477
YEAR VII, ISSUE 2/2021

EDITORIAL BOARD

CHIEF EDITOR

Prof. Tsanka Dikova, BG

DEPUTY EDITOR:

Dr. Alexander Krugljakow, Germany
Prof. Sergey Dobatkin, Russia
Prof. Sergey Nikulin, Russia
Prof. Victor Anchev, Bulgaria

MEMBERS:

Prof. Adel Mahmud, Iraq
Prof. Anna Proikova, Bulgaria
Prof. Bekir Sami Yilbas, Saudi Arabia
Prof. Dermot Brabazon, Ireland
Prof. Dipten Misra, India
Assoc. Prof.Eugeniy Grigoriev, Russia
Prof. F. W. Travis, United Kingdom
Prof. Gennagiy Bagluk, Ukraine
Assoc. Prof. Ibrahim E.Saklakoglu, Turkey
Prof. Iis Sopyan, Malaysia
Prof. Ivan Parshorov, Bulgaria
Prof. Ivanja Markova, Bulgaria
Prof. Janez Grum, Slovenia
Prof. Jens Bergstrom, Sweden
Prof. Leszek Dobrzanski, Poland
Prof. Ludmila Kaputkina, Russia
Prof. Nikolai Dulgerov, Bulgaria
Prof. Omer Keles, Turkey
Prof. Plamen Danev, Bulgaria
Prof. Rui Vilar, Portugal
Prof. Rusko Shishkov, Bulgaria
Prof. Saleem Hashmi, Ireland
Dr. Sefika Kasman, Turkey
Prof. Seiji Katayama, Japan
Prof. Souren Mitra, India
Dr. Sumsun Naher, United Kingdom
Prof. Svetlana Gubenko, Ukraine
Prof. Sveto Cvetkovski, Macedonia
Prof. Ventsislav Toshkov, Bulgaria
Prof. Yovka Dragieva, Bulgaria

C O N T E N T S

Comparative studies of mechanical characteristics of polycrystalline aluminum alloy AMg6 and nanocomposite n-AMg6/C60 under mechanical tensile tests and cyclic reversible loads.
Viacheslav Prokhorov, Ivan Evdokimov, Aleksandr Korobov, Natalia Odina, Natalia Shirgina 42

Modification of the properties of nanocomposites based on carbon nanostructures
Halyna Mykhailova, Mykola Yakymchuk, Iryna Galstian, Evgen Len, Oleksandr Gerasimov 46

Investigation of the mg supersaturated solid solution decomposition in the mg-dy-sm alloys
Lazar Rokhlin, Tatiana Dobatkina, Irina Tarytina, Elena Lukyanova, Olga Ovchinnikova 49

Effect of additional alloying on stabilization of structural state and mechanical properties of industrial magnesium-rich Al-Mg alloys
Alla Berezina., Tetiana Monastyrska., Oleh Molebny 52

Structure and magnetic properties of 1.4541 stainless steel
Demidenko Olga, Vetcher Alexander, Popescu Ana Maria, Constantin Virgil, Neacsu Elena Ionela, Donath Cristina 56

Microstructure and performance characteristics of experimental forged billets of ultrafinegrained structure two-phase titanium alloy VT8M-1
Grigory Dyakonov, Tatyana Yakovleva, Andrey Stotskiy, Irina Semenova 58

Structure-phase transformations in LiF powders and crystals irradiated in nuclear reactor and 60Co gamma-source
Elvira Ibragimova, Shovkat Buzrikov, Nurmuhamad Iskandarov, Malika Mussaeva, Khamdam Nazarov 60

Morphological and structural features of electrospark coatings
Auchynnikau Yauheni, Pinchuk Tatiana, Eisymont Yauhenia, Mihailov Valentin, Kazak Natalia, Bahanovich Ludmila 64

Application of sprayed bronze powders of the brsn10ph1 and BRSN5ZN5PB5 grades for applying protective coatings by gas-flame spraying
Aliaksandr Ilyushchanka, Ruslan Kusin, Yugeniy Manoila, Iryna Charniak, Aliaksei Kusin, Syargei Yurchanka, Artsiom Staselka, Anhelina Maiseyeva, Iryna Kurylchyk, Vladimir Semenov 67

Knowledge for material science. Part II
Stefan Bushev 70

Comparative studies of mechanical characteristics of polycrystalline aluminum alloy AMg6 and nanocomposite n-AMg6/C_{60} under mechanical tensile tests and cyclic reversible loads.

Viacheslav Prokhorov[1,2,*], Ivan Evdokimov[1], Aleksandr Korobov[3], Natalia Odina[3], Natalia Shirgina[3]
[1]Technological Institute for Superhard and Novel Carbon Materials, Moscow, 108840 Russia
[2]Moscow Institute of Physics and Technology (State University), Moscow, 141701 Russia
[3]Moscow State University, Moscow, 119991 Russia
*E-mail: pvm@tisnum.ru

Abstract: *Comparative experimental studies of the mechanical characteristics of polycrystalline aluminum alloy AMg6 and nanocomposite based on it n-AMg6/C_{60} during tension tests, as well as the effect of strain hardening on these characteristics during multi—cycle loading-unloading processes up to the destruction of the sample, are presented. The limits of strength and ductility, as well as the hardness and, by ultrasonic method, all independent second order elastic coefficients were measured.*
KEYWORDS: Multi-cycle loading, strain hardening, aluminum alloy, nano-composite, microhardness, mechanical and elastic properties,

1. Introduction

One of the modern methods used for improving the mechanical physical properties of metals and alloys is nanostructuring, i.e., formation of nanostructure in the entire volume of material [1]. In the last few years, there has been advanced progress in the development of nanostructuring techniques, which lead to new combinations of properties, such as high strength, higher hardness, record fatigue life, etc. [2-4].

More than 150 aluminum alloys are used in the fabrication of industrial products. AMg6 alloy belongs to the Al–Mg–Mn system, containing 93.68% aluminum, 5.8–6.8% magnesium, and 0.5–0.8% manganese and other impurities [5, 6].

Being well-welded at room and higher temperatures, it combines good strength and plastic characteristics. This set of properties favored the wide application of this alloy in the aerospace industry, building, and automobile engineering, while the corrosion resistance in various media, including seawater, explains its successful use in shipbuilding. In order to improve the mechanical properties of aluminum alloys, they are preliminarily exposed to mechanical deformation and heat treatment. It is, however, difficult to increase the strength characteristics of magnesium-containing AMg6 via quenching, as this alloy is not thermally hardenable.

The higher values of mechanical characteristics in nanocomposite carbon-hardened AMg6 alloy prepared via the milling in a ball mill with the subsequent extruding were acquired in [3]. The elongation at break in nanocomposite AMg6 was increased to 10.5–14.1% at higher hardness of 1.5–1.7 GPa.

The second-order elastic coefficients (SOECs) for nanomaterials are almost equal to those of the appropriate initial microcrystalline objects. This conclusion is, however, valid for materials with the low interface fraction (the atom content at the interface to the amount of atoms in the bulk). At the crystallite size of ≤10 nm, when this fraction is dozens of percent, the elastic characteristic values are expected to additively reduce owing to the inner porosity in the nanomaterial. Obviously, the pronounced decrease in the elastic characteristics can be avoid by filling the voids of nanoparticle joints with a material possessing high elastic and strength properties (i.e., by forming a nanocomposite), whereas the formation of the chemical bounds between this material and the nanoparticle surface can also favor the increase in the elastic moduli [7].

The second- and third-order elastic coefficients in polycrystalline AMg6 alloy and the *n*-AMg6/C_{60} nanocomposite were experimentally determined in our previous work [8-10].

In the present work these studies are continued and effect of reversible mechanical loading-unloading on the mechanical and elastic properties of n-AMg6/C_{60} nanostructured composite was experimentally investigated.

Experimental studies on the influence of loading–unloading processes on the mechanical, linear, and nonlinear properties of the strain-hardening polycrystalline aluminum alloy AMg6 carried out in our work [11]. The stress–strain curve is measured for AMg6 samples under high-cycle loading–unloading up to fracture of a sample. The microhardness of the sample is measured before and after its fracture. It has been found that the loading–unloading process leads to strain hardening of the AMg6 alloy.

This paper presents the results of comparative experimental studies of the mechanical characteristics of polycrystalline aluminum alloy AMg6 and nanocomposite based on it n-AMg6/C_{60} during tension tests, as well as the effect of strain hardening on these characteristics during multi—cycle loading-unloading processes up to the destruction of the sample, are presented.

2. Experimental procedures

2.1. Sample preparation and characterization

Nanocomposite n-AMg6/C_{60} were prepared from a commercial castle polycrystalline alloy. The alloy has the following chemical composition: Mg - 6.124%, Mn - 0.5977%, Fe - 0.351%, Si - 0.310%, Zn - 0.203%, Ti - 0.0843%, Cu - 0.086%, Al - the rest main part.

A mixture of small chips of the alloy with the addition of 0.3 wt.% fullerite C_{60} was treated by refinement and homogenization in a planetary mill in 60 min work cycles. The resulting product consists of 200-500 micron agglomerates of nanoparticles. The coherent scattering length (CSL) distribution in powdered samples showed the mean nanoparticle size ~ 40-60 nm according to the X-ray analysis.

The resulting product consists of 200-500 micron agglomerates of nanoparticles. The coherent scattering length (CSL) distribution in powdered samples showed the mean nanoparticle size ~ 40-60 nm according to the X-ray analysis.

Figure 1 shows the SEM images of *n*-AMg6/C_{60} nanocomposite powder particles after milling.

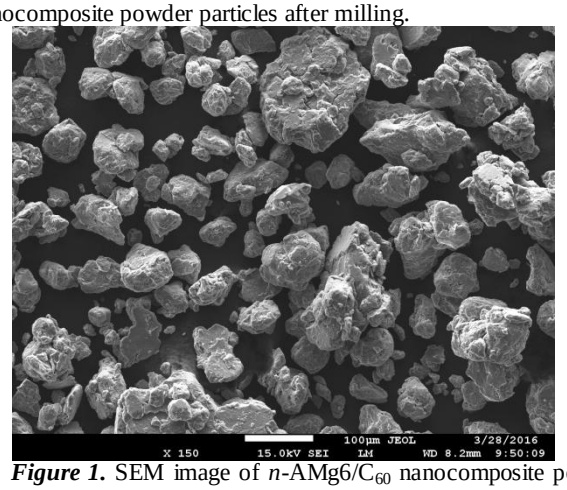


Figure 1. SEM image of *n*-AMg6/C_{60} nanocomposite powder particles after milling.

Then, the milled nanopowder was pre-compacted in a cylindrical mold with a diameter of 180 mm at a temperature of 250 ^{0}C and a pressure of 200-300 MPa.

The resulting compact was subjected to extruding at a temperature of 300 ^{0}C with a reduction of cross-sectional area at least 4 times (in this case to a diameter of 90 mm). The recrystallization process is hindered by grain boundary modification

with fullerite C_{60}; the latter plays the role of compacted samples' stabilizer.



Figure 2. *Nanocomposite n-AMg6/C_{60} after extrusion*

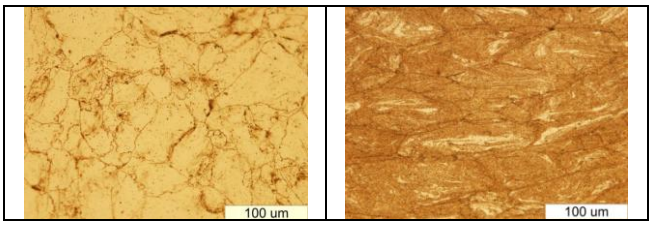


Figure 3. *The metallography images of the microstructures of the initial AMg6 alloy (a) and nanostructured nAMg6/C_{60} (b) after extrusion, obtained on a BX51 Olympus microscope.*

As is seen, the aluminum grains after extrusion are oriented along the extrusion axis and there are no pores between the grains. It is worth mentioning that the microstructure of the extruded nanocomposites inherits the morphology of powders after their milling (Fig.1). As is seen, the grain size in the sintered material (Fig. 3b) corresponds to the aggregate dimensions and agglomerates in the nanocomposite powder (Fig. 1). This inherity allows tuning the structure in the nanocomposite at the preparation stage that opens the wide abilities in the management of the properties of the final product [8].

Samples for research were made from the extruded billet.

2.2. Measurements of density, hardness, ultrasound velocities and elastic constants

Eighteen samples with the shape of a cuboid of 20mm×20mm×40 mm size were cut from different areas of the extruded rod; two from the central and eight from peripheral parts of the extruded n-AMg6/C_{60} rod. For comparison three samples of the same size were made from billet alloy AMg6. The opposite sides of the samples were polished and strictly parallel.

The study of the density via the hydrostatic weighing revealed that the density of the extruded samples is 2.63 ± 0.02 g/cm3, which corresponds to 99% of the specific density of the AMg6 alloy. The density of samples was measured on a KERN-770-60 balance equipped with a Sartorius YDK 01 LP console.

Microhardness measurements were performed on metallographic sections cut out from different parts of the specimens. The surfaces of the specimens were grinded and polished using a LaboPol2(Struers) apparatus. The microhardness of metallographic sections was measured according to GOST 2999-75 State Standard by DuraScan20 hardness gauge by applying a 50-g load on Vickers indentor during 12 s.

The second order elastic constants in specimens of parent AMg6-alloy and n-AMg6/C_{60} were determined from measurement of the densities and velocities of longitudinal and shear balk acoustic waves (BAWs): $\rho_0 V_L^2 = C_{11}$, $\rho_0 V_T^2 = C_{44}$, where ρ_0 - the material's density, V_L and V_T - the velocities of longitudinal and shear BAWs. The velocity V of elastic waves was measured by a pulsed "reflection" method using the formula $V = 2L/\tau$, where L is the sample length and τ is the time of double passage of the acoustic pulse through the sample.

2.3. Tensile tests

The tensile tests were carried out using an Instron 5982 Multipurpose Floor-mounted System for Electromechanical Tests (Germany). When the samples obtained by extrusion were subjected to the tensile test, the load direction coincided with the wire axis. The load speed was 0.2 mm/min.

The tensile properties were evaluated for standard-shape samples (the neck diameter of 4 mm and the length of 50 mm) prepared from the AMg6 precursor and *n*-AMg6/C_{60} extruded composite. The general view of the experimental setup and the samples prepared for the mechanical tests is illustrated in Fig. 4.

Figure 4. Instron 5982 test machine-based installation and test samples

Figure 5 shows typical deformation diagrams of the samples of the initial AMg6 (Fig.5a) and the nanocomposite n-AMg6/C_{60} (Fig. 5b).

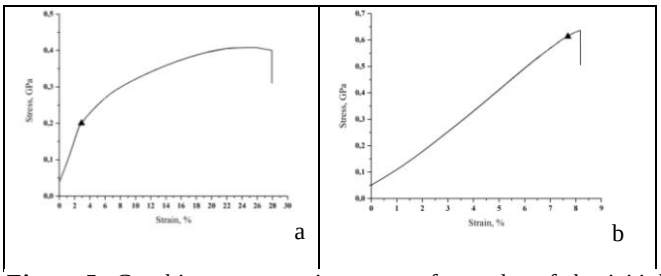


Figure 5. *Graphics stress-strain curves of samples of the initial alloy AMg6 (a) and noncomposite n-AMg6/C_{60} (b).*

Presented in Fig. 5 data show that the yield strength ($\sigma_{0,2}$) tensile nanostructured n-AMg6/C_{60} increased from the value of 210 MPa (for the original alloy AMg6) up to 640 MPa. It is worth noting that along with the increase in strength, there is a sharp drop in the plasticity of the nanostructured n-AMg6/C_{60}. This behavior is typical for nanostructured materials and is associated with the difficulty of implementing the mechanisms of intergranular slippage and migration of dislocations in the volume of the material.

2.4. Reversible tensile-compressive tests with ultrasound measurements

The effect of static reversible mechanical deformations on the mechanical and linear and nonlinear elastic properties of the initial AMg6 alloy was investigated in our previous work [9]. In [10], for polycrystalline AMg6 aluminum—magnesium alloy and n-AMg6/C_{60} nanocomposite fabricated on its basis, the results of



ultrasonic measurements of second-order elastic constants as functions of hydrostatic pressure up to 1.6 GPa were presented. In this paper, we complement these data with the results obtained for n-AMg6/C_{60} nanocomposite specimens subjected to multiple

loading— unloading cycles.

The mechanical device producing reversible tensile-compressive strains in the specimens under study was constructed by us on the basis of a 20-ton press (produced by the MATRIX company) [11]. The measuring system included a Ritec RAM-5000 automated ultrasonic system, a DS09104A four-channel digital oscilloscope, and a mechanical device producing controlled reversible tensile—compressive strains in the material under study (Fig. 6). The ultrasonic Ritec RAM-5000 SNAP SYSTEM operated in a pulsed mode and was intended for measuring linear and nonlinear elastic properties of solids.

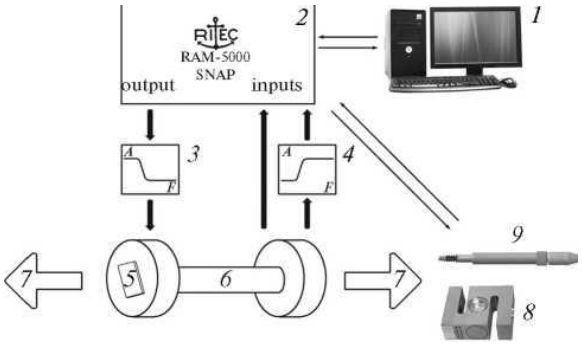


Figure 6. *Experimental setup:* (1) *personal computer, (2) Ritec automated ultrasonic system,* (3) *high-frequency filter, (4) low-frequency filter,* (5) *lithium niobate piezoelectric transducer, (6) specimen,* (7) *tensile external force generated by a screw jack, (8) anyload pressure gauge, and (9) Waycon elongation detector.*

The system implemented static method for measuring the o—e stress—strain curve under reversible stress variation in the specimen under study and pulsed method of measuring the velocity and absorption of bulk acoustic waves and determining all the components of the second-order elasticity tensor in solids (Fig. 7).

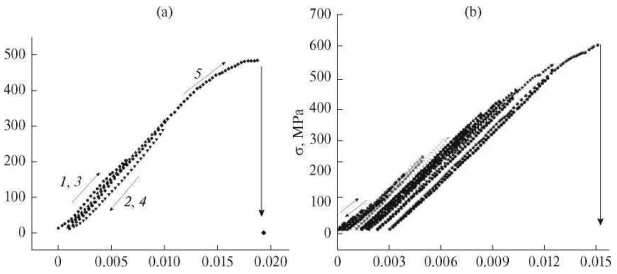


Figure 7. Stress-strain curves, σ—ε, for specimens (a) 1 and (b) 2 of n-AMg6/C_{60} alloy under cyclic stress variation.

3. Results and discussion

3.1 Microhardness

For n-AMg6/C_{60} nanocomposite specimen, microhardness measurements were performed on metallographic sections cut out from different parts of the n-AMg6/C_{60} specimen subjected to cyclic deformation down to fracture (Fig.7): from part 5, which was almost unstrained under cyclic loading—unloading, and from part 6, which experienced considerable plastic strain down to fracture. Microhardness was measured at five points, which were spaced at 2 mm and positioned along the diameter, and at another five points, which were spaced at 6 mm and positioned at the surface of the head of the dumbbell with a diameter of 25 mm (Fig.8). The microhardness values were averaged over the results of five measurements.

Figures 7a and 7b represent the results of measuring the stress-strain curves, σ = σ (ε), for two specimens under cyclic stress variation. In the course of reversible loading—unloading, residual strains observed at zero tensile stress σ = 0 were virtually absent for both specimens. Specimen 2 underwent fracture after 13 loading—unloading cycles at σ ~ 610 MPa and ε ~ 0.016. For specimen 1, fracture occurred after three loading—unloading cycles at σ ~ 486 MPa and ε ~ 0.02. The difference in the stress and strain values corresponding to fracture of specimens 1 and 2 points to considerable hardening of material in specimen 2, as compared to specimen 1, because specimen 2 was subjected to greater number of loading— unloading cycles. For both specimens, no formation of a characteristic "neck" was observed in the near-fracture region. This fact testifies to brittle fracture of specimens (Fig. 8).

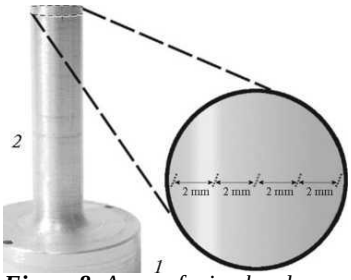


Figure 8. *Areas of microhardness measurements.*

For metallographic specimens with a circular cross section 8 mm in diameter (Fig. 8, part 2), which were cut out normally to the cylindrical axis of the specimen, microhardness was measured at five points, which were spaced at 2 mm and positioned along the diameter, and at another five points, which were spaced at 6 mm and positioned at the surface of the head of the dumbbell with a diameter of 25 mm (Fig. 8, part 1). The microhardness values were averaged over the results of five measurements.

For unstrained part *1* of n-AMg6/C_{60}, the measured values of microhardness *H* were *H* = 1.29 ± 0.03 GPa. For part *2* of n-AMg6/C_{60}, the average value was H_{av} = 1.74 ± 0.04 GPa. The microhardness distribution along the diameter perpendicular to the axis of the specimen was measured. One can see that, at the edges of the diameter, microhardness is greater, as compared to the inner region of strained part *2*. This is related to the fact that, as the specimen is machined by a lathe, the external side of the deformed part of the specimen is subjected to additional mechanical loading, which causes additional hardening of the cylindrical surface of the specimen.

3.2. Linear elastic properties (second-order elastic constant)

Obtained average values of linear elastic characteristics are presented in Table 1. The values of modules for nano-alloy and ingot alloy are the same within the error range. In [xz], we found a significant difference in the nonlinear elastic constants. The study of nonlinear elastic characteristics is beyond the scope of this work.

Experimental measurements of stress—strain curves allowed us to estimate the values of Young's modulus for linear portions of the loading—unloading characteristic of specimen 1. The results are shown in Table 2. For the loading portions of the stress—strain curve, the values of Young's modulus are smaller, as compared to those for unloading portions. This is related to hardening of the specimen under load.

TABLE 1. *Linear elastic characteristics of AMg6 and nanostructured AMg6/C_{60} alloys*

Material	ρ(±0.005) g/cm^3	V_L(±0.06) km/s	V_T(±0.03) km/s	C11 (±1) GPa	C44(±0.4) GPa	*E* (±1) GPa	*B* (±1) GPa	σ (±0.004)
AMg6	2.630	6.30	3.14	104	26.0	69.3	69.8	0.334
n-AMg6	2.622	6.325	3.18	105	26.5	70.6	69.7	0.331

Table 2. *Estimates of Young's modulus for n-AMg6/C_{60} composite from stress—strain curves*

E, GPa, portion 1	*E*, GPa, portion 2	*E*, GPa, portion 3	*E*, GPa, portion 4	*E*, GPa, portion 5
31.4 ± 0.03	34.9 ± 0.03	32.7 ± 0.03	33.2 ± 0.03	28.8 ± 0.03

Simultaneously with measuring the stress—strain curve in the course of reversible loading—unloading cycles by the pulsed method for specimens 1 and 2, we measured the dependences of velocity *V* of longitudinal bulk acoustic waves on varying tensile stress *a* (Figs. 7a and 7b). After two loading-unloading cycles, the velocity increased by 0.2% and, after 12 loading-unloading cycles, it increased by almost 0.5%, as compared to the unloaded specimen. At the instant of fracture, the velocity of bulk elastic waves in the specimen decreased by approximately 16%, as compared to the unloaded specimen.

4. Conclusions

Effect of reversible mechanical loading-unloading on the mechanical and elastic properties of n-AMg6/C_{60} nanostructured composite was experimentally investigated.

For n-AMg6/C_{60} nanostructured composite specimens, stress-strain curves, $\sigma = \sigma(\varepsilon)$, were measured under cyclic variation of stress applied to the specimens. In the experiments, almost no residual strains were detected in n-AMg6/C_{60} composite specimens and the stress-strain curves contained no zones corresponding to plastic strain. It was found that reversible mechanical loading—unloading of n-AMg6/C_{60} specimens caused their hardening.

5. Acknowledgments

The work was done using the Shared Research Facilities "Research of Nanostructured, Carbon and Superhard Materials" FSBI TISNCM.

6. Literature

[1] R. Z. Valiev and I. V. Aleksandrov, *Volumetric Nanostructure Metal Materials. Synthesizing, Structure, and Properties* (Akademkniga, Moscow, 2007) [in Russian].

[2] G. S. Bezruchko, S. V. Razorenov, and M. Yu. Popov, Tech. Phys. 59 (3), (2014). P. 378.

[3] N. Lvova, I. Evdokimov, and S. Perfilov, Adv. Mater. Res. 1119, (2015), P.9.

[4] A. Evdokimov, S. A. Perfilov, A. A. Pozdnyakov, et al., Inorg. Mater.: Appl. Res. 9 (3), (2018), P. 472.

[5] Construction Materials: A Handbook, Ed. by B. N. Arzamasov (Mashinostroenie, Moscow, 1990) [in Russian].

[6] A. P. Babichev, N. A. Babushkina, and A. M. Bratkovskii, in Handbook of Physical Quantities, Ed. By E. S. Grigoriev and E. Z. Meilikhov (Energoatomizdat, Moscow, 1991; CRC Press, Boca Raton, Florida, United States, 1997).

[7] V. M. Prokhorov, V. D. Blank, R. H. Bagramov, S. A. Perfilov, and G. I. Pivovarov, AIP Conf. Proc. **1569**, (2013), P. 389.

[8] A.I. Korobov, A.I. Kokshaiskii, V.M. Prokhorov, I.A. Evdokimov, S.A. Perfilov, A.D. Volkov. Physics of the Solid State, 58, (2016), P.2472.

[9] . Volkov, A.I. Kokshaiskii, A.I. Korobov, V.M. Prokhorov, Acoustical Physics, 61, (2015), P. 651.

[10] Prokhorov V., Gromnitskaya E. Material Science. Non-Equilibrium Phase Transformations. 3, (2017), P.111.

[11] A.I. Korobov, N.V. Shirgina, A.I. Kokshaiskii, V.M. Prokhorov, Acoustical Physics, 65, (2019), P. 151.

Modification of the properties of nanocomposites based on carbon nanostructures

Halyna Mykhailova, Mykola Yakymchuk, Iryna Galstian, Evgen Len, Oleksandr Gerasimov
G. V. Kurdyumov Institute for Metal Physics of the N.A.S. of Ukraine
36 Academician Vernadsky Boulevard, UA-03142 Kyiv, Ukraine
E-mail: mihajlova.halina@gmail.com

***Abstract**: The electrical and mechanical properties of nanocomposites based on carbon nanostructures has been studied. It is sown that at a concentration of carbon nanotubes of 15-30 wt. %, the electrical resistance of the samples decreases to 1 order, while its mechanical properties change insignificantly, which is due to the transfer of free electrons from the metal to the CNT, which is comparable to the number of electrical contacts between the constituent elements of the composite and the competition between the numbers of tunneling and ohmic contacts.*

***KEY WORDS:** CARBON NANOTUBES, ELECTRICAL RESISTIVITY, COMPOSITE, MECHANICAL PROPERTIES*

Introduction

Carbon nanotubes (CNTs) attract the attention of scientists from many countries of the world last 30 years. This interest is due to their unusual properties: they combine high strength and elasticity, heat and electrical conductivity. Mechanical deformation and defects influence the electronic structure, concentration of charge carriers, electrical, emission and other properties of CNT. Defects arise both in the process of synthesis (growth and gas admixtures) of CNT, and with external influences, especially in radiation. They reject the form of CNT from the rectilinear, change the conditions of passage of current, affect the concentration of charge carriers, Fermi energy and electrical conductivity.

The properties of the array of CNTs, as well and materials that containing its, differ from the properties of individual nanotubes. Individual CNT may have a metallic type of conductivity, array of CNTs may not be conductivity. This is due to the fact that in the initial array of CNTs, the distances between adjacent nanotubes can be very large, the contacts between them are small and mostly tunnel, that is no formed the conductive network. It can be achieved by increasing the area of contacts between adjacent tubes (reducing the volume between them) or adding of a small amount of CNT to the dielectric matrix promotes the appearance of the electrical conductivity of the composite [1-6], the value of which can vary in a wide range of values. This variation in the value of electrical conductivity is due to the complex interaction of various factors, the most important of which - the presence of CNTs with different types of intrinsic conductivity, their concentration and types and magnitudes of contact resistance between CNTs.

Nanostructured composite materials are characterized by adjustable anisotropy and gradient structure of properties due to a certain orientation of the fibers in the matrix, which can be achieved by using mainly powder technologies. Nanofibers, carbon nanotubes, including those functionalized by metals, oxidation and hydroxidation, nanoparticles of irregular or spherical shape, including metal particles and feet, are used as nanosized fillers of composite materials.

The main factors influencing the properties of metal-matrix composites, which are reinforced with CNT, are the following: differences in the properties of CNT, the degree of decoupling of agglomerates and the uniform distribution of CNT in the metal; method and degree of compaction of a mixture of metal powder and CNT; wide variation of the ratio of length to diameter of CNT (aspect ratio); possible chemical reactions between carbon and metal, leading to the formation of carbides [7].

Metal-based composites have the potential to replace traditional materials in the automotive, aerospace and other industries. This is facilitated by their excellent mechanical, physical, thermal properties, the ratio of their strength to weight, which is important for the different industry [8, 9].

Composite materials such as metal-CNT acquire new qualities that were not present in any of their original pure components, it allows the use of such composites in the creation, for example, materials for "cold" cathodes of photothermal converters, for which are important as high conductivity and surface geometry, namely, the presence of separately located elements of the composite surface in the form of sharp CNT needles, around which the electric field strength can increase by several orders of magnitude, which increases the proportion of electrons leaving the cathode not due to thermal emission but tunneling. through reduced by the electric field potential barriers at the tips of CNTs. The possibility of realizing the effect of "cold" emission requires a more careful study of promising for these purposes metal-nanocarbon composites, in particular their mechanical and electrical properties.

Experiment

In bulk, carbon nanotubes do not form a conductive environment. However, under compressed, they become conductive due to the increase in the number and density of electrical contacts both between adjacent nanotubes and between them and the electrodes. It is necessary to distinguish between the electrical conductivity of individual CNTs and the material of which they are elements. Peculiarities of the atomic structure and its defects are decisive for the electrical conductivity of individual CNTs, and for the case of the CNT array, in addition to the existing types of CNT defects and impurities, the number and density (type) of contacts between adjacent nanotubes are important [10, 11, 12].

In this work, the electrical conductivity of the CNT ensemble was measured according to the original method [13]. The electrical characteristics of the sample were taken by using a device consisting of an insulating framework, a press matrix, two electrodes, one of which is movable. When the piston is lowered, the sample is loaded, its volume decreases, the density of the powder material increases and conductive paths are created in it, while the electrical conductivity increases rapidly (by orders of magnitude), which is accompanied by the transition of the CNT array to the conductive state. This occurs at a certain density of the powder sample containing the amount of CNTs greater than the threshold, when the contacts between the CNTs form percolation pathways that ensure the conductivity of the material. After the maximum achievable under the conditions of this experiment compression of such material, the piston was gradually raised, the material was partially relaxed, and simultaneously with the unloading also measured the electrical conductivity. The cessation of the relaxation expansion of the material during the lifting of the piston was recorded by a sharp decrease in electrical conductivity, which accompanied the opening of the electrical circuit due to the loss of contact of the powder with the moving electrode.

Nanosystems appeared at the brightness of the sparks, which were deposited from metal particles of cuprum and multy wall carbon nanotubes with different amount of residues (Cu + *c*% wt. CNT). Particles of Cu powder are small linearly sized from 20 nm to 1 micron. CNT was received by the method of CVD from the gas phase on catalysts containing Al/Fe/Mo transition metals in propylene vapors at a temperature of 923-1023 K, according to mass spectrometry contain water. The nanocomposites of the Cu – CNT system have been adjusted to the mechanical mixing in the primary components in the different proportions.

Results

Figure 1 shows the dependence of the electrical resistivity Ω of samples in processes of compression the bulk mass of particles Cu (*a*), MCNT (*b*) and their mechanical mixture containing 65 wt.

% CNT (*b*) in load and unload deformation. All curves Ω(ρ) have hysteresis, which indicates the course of inelastic processes. The minimum value of Ω(ρ) is fixed at a density of ρ = 0.07 g/cm^3 and is equal 2.38 (Ohm · cm), then, with increasing ρ to 0.09 g/cm^3, decreases by half and than practically does not change as a result of the partial orientation of the CNT in the plane of the electrodes and the increase in the contribution to the electrical conductivity of the tunnel current. Its proceed by formation of a three-dimensional grid of CNT - ways of transferring electric charges along the axis of nanotubes, and tunneling through the Van der Waals gap between adjacent nanotubes.

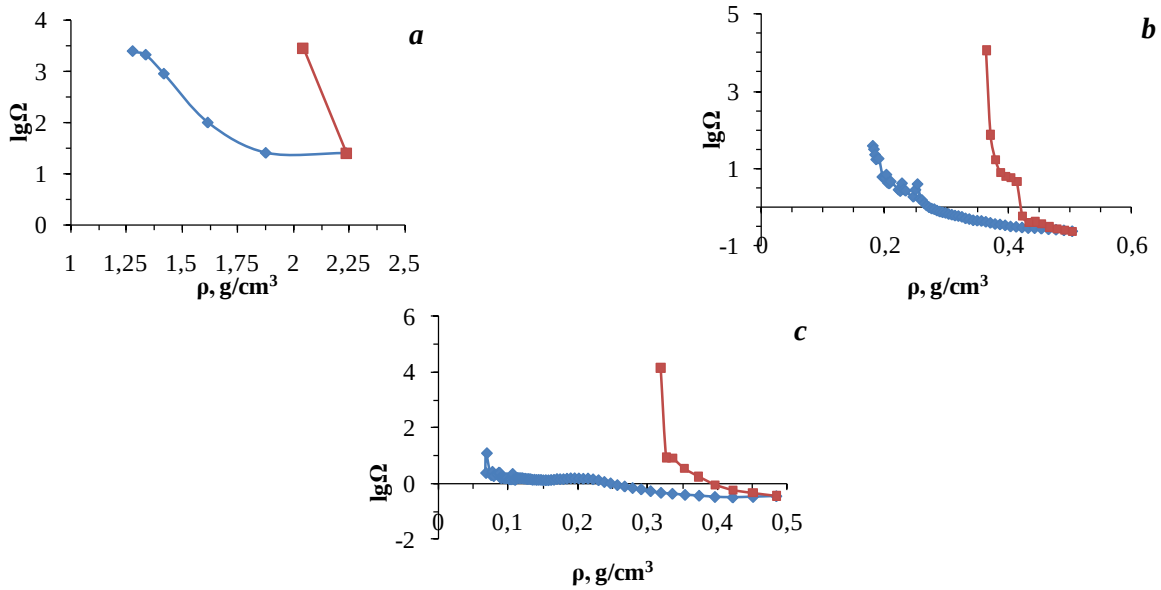


Fig. 1. *Dependences of electrical resistivity Ω of metal–carbon composites with different content of carbon nanostructures on the density ρ of the material in the process of loading–unloading.*

As the process of unloading the volume filled with nanotubes increases, the electrical contacts between the CNT and with the electrodes are maintained due to the elastic relaxation (Fig. 1, *c*) of the pre-compressed simple. The reverse type of the curve Ω(ρ) practically repeats the direct course in the part ρ, after which a rapid increase in the value of Ω by 5 orders of magnitude at ρ = 0.32 g/cm^3, apparently due to a decrease the total area of contacts between nanotubes and with electrodes, the process ends with a break in the electrical circuit (Ω = ∞). Nanocomposites with different percentages of CNT were investigated. The thermo-EMF for these composites has also been adjusted, it is shown that the increase in the carbon component has been increased for the growth of the Seebeck's efficiency. The results are presented in table 1.

Increased concentration of CNT up to 3,92 wt. almost does not affectto the electrical resistivity, but adding of 16 wt. % change it for 8 times compared to the original copper powder. The efficiency of the increase in the concentration of electrical power at the CNT, the degradation of its products, with the indicated concentration. These effects are due to the increase in the concentration of conduction electrons in CNTs, where their mobility is higher, at these concentrations. Increasing the concentration of CNT up to 60 wt. % reduces the electrical resistance by 2 orders of magnitude (table 1), after which it is practically not eliminated. The latter is due to the presence of water in CNT.

It is known that CNTs have a low concentration of conduction electrons (n_e=1.3·10^{19} cm^{-3}), which have a high mobility (μ_{CNT}~10 m2/V·s) [14], and metals, have a high concentration of electrons (~ 10^{22}) with very low mobility. This means that the rapid decrease in the resistivity in the nanosystem is due to an increase in the concentration of electrons in the CNT with a slight change in mobility. During the contact of copper particles with CNTs ($\varphi_{Cu} \approx \varphi_{CNT}$), electrons will pass from the metal to the CNT and increase their concentration in it.

Table 1. Electrophysical parameters of nanocomposites Cu + c wt.% CNT

	Ω, Ohmcm	α, μV/K	ε, %
0	25		43
3,92	23,80	18	63
16,16	3,38	29,9	63
26,26	1,50	25,71	68
40	0,82	27,5	72
50	0,46	27,57	60
60	0,25	28,02	65
64,4	0,23	28,5	64
70,5	0,28	28,86	71
75	0,27	28,56	70
77,5	0,30	28,6	53
80,4	0,28	28,29	72
90	0,29	24,75	69
100	0,32	37,77	86

The increase in the concentration of current carriers in the CNT due to the transfer of charge from the metal should lead to a decrease in resistance. a decrease in resistance by an order of magnitude during the establishment of electrical contacts between CNTs and metal is observed only at a certain concentration of CNTs. Charge transfer means that CNTs have an excess of charge and metal particles lack them. As a result, CNTs and metallic particles must have a Coulomb attraction. It is obvious that at concentrations 60 wt. % and more the mechanism of electron transfer from metal to CNT works most effectively.

Conclusions

Adding to the CNT metal particles resistivity increases more than an order of magnitude, as a result of the transition of electrons from metal to CNT, the mobility of which is greater than in metals, leading to Coulomb interaction between different components and streamlining the system.

References

1. Yao Zh., Postma H. W. Ch., Balents L., Dekker C., Imaging and Characterization of Molecules and One- Dimensional Crystals Formed within Carbon Nanotubes *Nature*, V. 402. 1999.P. 273.
2. Curran S. A., Talla J., Dias S., Zhang D.,Carroll D. Electrical transport measurements of highly conductive carbon nanotube / poly (bisphenol A carbonate) composite *J. Appl. Phys.*V. 105. 2009. P. 073711.
3. Ahmad K., Pan W., Shi S. L. Electrical conductivity and dielectric properties of multiwalled carbon nanotube and alumina composites *Appl. Phys. Lett.*V. 89. 2006.P. 133122.
4. Sandler J. K. W., Kirk J. E., Kinloch I. A., Shaffer M. S. P., Windle A. H. Ultra-low electrical percolation threshold in carbon-nanotube-epoxy composites *Polymer*.V. 44. 2003. P. 5893.
5. Bryning M. B., Islam M. F., Kikkawa J. M., Yodh A. G. Very Low Conductivity Threshold in Bulk Isotropic Single - Walled Carbon Nanotube – Epoxy Composites *Adv. Mater.*V. 17. 2005. P. 1186.
6. Kymakis E., Alexandou I., Amaratunga G. A. Electrical Properties of Soluble Carbon Nanotube / Polymer Composite Films *Synthetic Metals.*V. 127. 2002. P. 59.
7. Sundaram R. M., Sekiguchi A., Sekiya M., Yamada T., Hata K. *R. Copper / carbon nanotube composites: research trends and outlook Soc. Open Sci.*V. 5.Iss. 11. 2018. P. 180814.
8. Collins P. G. Extreme oxygen sensitivity of electronic properties of carbon nanotubes *Science*.V. 287. 2000. P. 1801.
9. Li Guo- ran, Wang Feng, Jiang Qi- wei, Gao Xue- ping, Shen Pan- wen. Carbon Dioxide Capture by Superbase-Derived Protic Ionic Liquids *Carbon, Advantante Chemie*.V. 49. 2010.P. 3653.
10. Nishchenko M.M., Mykhailova H.Yu., Arkhipov E.I., Koda V.Yu., Prikhodko G.P., Sementsov Yu.I. Electrical conductivity of an array of multilayer carbon nanotubes during compression deformation Metallofizika i Noveishie Tekhnologii. T. 31. № 4. 2009.P. 437.
11. Mikhailova G.Yu., Nishchenko M.M., Pimenov V.N.,Starostin E.E., Tovtin V.I. Thermoelectric and Elastic Properties of Carbon Nanotubes Irradiated with High-Energy Electrons *Inorganic Mater.: Appl. Res.*V. 10.No. 5. 2019.P. 1052.
12. Nishchenko M.M., Mikhailova G.Yu., Kovalchuk B.V., Sidorchenko I.M., Anikeev V.V., Shevchenko N.A., Poroshin V.M., Prikhodko G.P. Thermoelectric Properties of an Array of Carbon Nanotubes under Uniaxial Compression after Annealing Metallofizika i Noveishie Tekhnologii. T. 40. № 2. 2018.P. 169.
13. Zhang S., Ji Ch., Bian Zh., Liu R., Xia X., Yun D., Zhang L., Huang Ch., Cao A. Single-wire dye-sensitized solar cells wrapped by carbon nanotube film electrodes *NanoLett.* V. 11. (2011).P. 3383.
14. Mavrinsky A.V., Andriychuk V.P., Baitinger E.M. Thermoelectromotive force of powdered tubulens // News of the Chelyabinsk Scientific Center. - 2002. - No. 3. - P. 16-20.

Investigation of the mg supersaturated solid solution decomposition in the mg-dy-sm alloys

Lazar Rokhlin, Tatiana Dobatkina, Irina Tarytina, Elena Lukyanova, Olga Ovchinnikova
Institution of Russian Academy of Sciences. A.A. Baikov Institute of Metallurgy and Material Science RAS, Russia

Abstract: *Kinetics and phase transformations during decomposition of the supersaturated Mg solid solution in the Mg-Dy-Sm alloys at different Dy/Sm content ratios were investigated in this work. The solid solution decomposition occurs upon aging at a temperature of 200°C, at which strengthening of the alloys was expected to be highest. With increasing Dy/Sm ratio, the solid solution decomposition gradually decelerates. Addition of Dy to the Mg-Sm alloys intnsifies the age hardening, and the addition of Sm to the Mg-Dy alloys also promotes the hardening. The Mg solid solution decomposition in the ternary Mg-Dy-Sm alloys is accompanied by the formation of the GP-zones, ordering, and the precipitation of plate-like particles in certain planes of the Mg crystal lattice. Such processes are typical of solid solution decomposition in the binary Mg-Re (Nd, Sm, Y, Gd, Tb, Dy) alloys.*
KEYWORDS*: MAGNESIUM ALLOYS, RARE-EARTH METALS, SOLID SOLUTION DECOMPOSITION, PHASE TRANSFORMATION*

1. Introduction

Magnesium alloys attract a great attention now as the structural materials of low density. They are advantageous for various applications, especially in aerospace and automotive industries, where the weight saving of the constructions is very important [1-3]. As all other structural materials, magnesium alloys should have high strength, which is generally increased by using various alloying additions. Recent investigations show that the highest strength of magnesium alloys at near room and elevated temperatures can be obtained by alloying with certain rare-earth metals [4,5]. In particular, the rare-earth metals belonging to different subgroups such as the cerium subgroup including elements from La to Eu of the lanthanum row and the yttrium subgroup including Y and the elements from Gd to Lu of the lanthanum row apparently differ in the action on magnesium. The Mg-Dy-Sm alloys attract interest because the strength properties of the Mg alloys with rare-earth metals are greatly determined by the decomposition of supersaturated Mg solid solution upon heat treatment. The binary Mg alloys with Sm (cerium subgroup) and Dy (yttrium subgroup) are characterized by high strengthening upon such process, but differ in some important specific features [4]. The aims of this work were as follows:

1) Determination of the decomposition kinetics of the supersaturated Mg-based solid solution in the ternary Mg-Dy-Sm alloys, especially the kinetics of the alloy strengthening upon the decomposition.

2) Establishment of the effect of dysprosium to samarium concentration ratio on the decomposition rate of supersaturated Mg solid solution and the maximum strengthening, which can be achieved upon this process.

2. Materials and methods

The alloys were prepared by melting the initial metals taken in certain proportions in the electrical resistance furnace in crucibles of low-carbon steel under flux preventing Mg melts from burning at air. The prepared melts of the alloys were cast into mould of stainless steel to ingots of 15 mm in diameter and 90 mm in length.

The alloy compositions and their heat treatment regimes were chosen with allowance for the equilibrium Mg-Dy-Sm phase diagram [6]. The ingots of the prepared alloys were solution treated by annealing at 520ºC for 6 hours and quenched in room-temperature water for obtaining supersaturated solid solutions of Mg-based alloys. The decomposition of Mg solid solution upon aging at 200^{o}C was monitored by the measurements of hardness and electrical resistivity. The structure was examined by optical microscopy and transmission electron microscopy (TEM).

.

3. Results and discussion

The results of the hardness measurements upon isothermal aging of the Mg-Dy-Sm alloys are shown in Fig.1. Analysis of the data indicates the certain specific features of the age hardening of the ternary Mg-Dy-Sm alloys as compared with that of the binary Mg-Dy and Mg-Sm alloys.

The first feature is that the addition of Dy to the Mg-Sm alloys and increase in the Dy content generally increase the hardness of the alloy. The hardness maxima reached upon aging of the alloys become higher with increasing Dy content and, correspondingly, with increasing Dy/Sm ratio. The second feature of the age-hardening of the Mg-Dy-Sm alloys is that this process occurs by two stages differing in kinetics. At the first stage, the hardness changes slowly and insignificantly, but at the second stage the hardness increases abruptly and reaches maximum. The existence of the two stages manifests itself differently in different alloys. In the binary Mg-Sm alloy and in the ternary alloys with the smallest Dy contents they are virtually absent.

The results of the electrical resistivity measurements of the alloys upon isothermal aging are presented in Fig.2. The resistivity increases successively with increasing total content of the rare-earth metals in the alloys in accordance with the possibility to have more quantities of the soluble atoms in the supersaturated Mg-based solid solutions. Decrease in the electrical resistivity with increasing aging time exhibits the depletion of the Mg-based supersaturated solid solutions since the rare-earth atoms go out of them. Meanwhile, the electrical resistivity curves display kinks reflecting the certain stages of this process. In general, the stages of the solid solution depletion illustrated by the electrical resistivity curves correspond to the above mentioned two stages of the solid solution decomposition traced by the hardness measurements. Optical microscopy was found to be insufficiently informative for investigation of the alloy structures

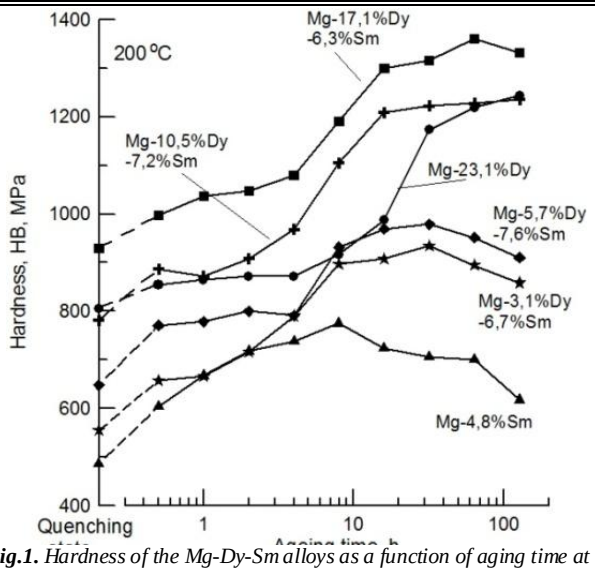


Fig.1. *Hardness of the Mg-Dy-Sm alloys as a function of aging time at 200°C*

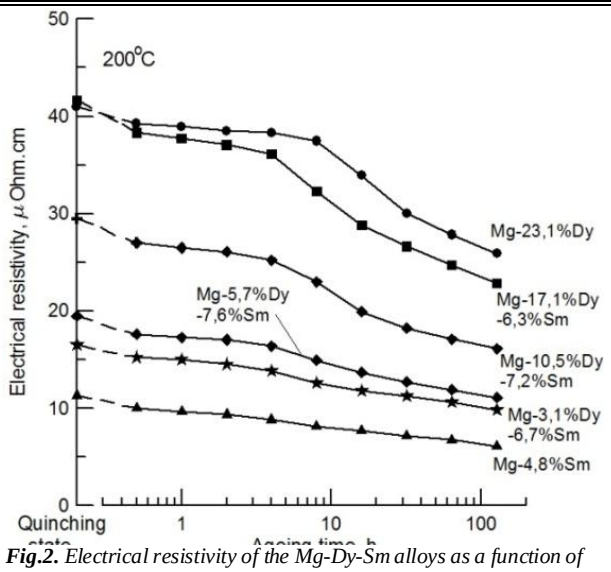


Fig.2. *Electrical resistivity of the Mg-Dy-Sm alloys as a function of aging time at 200°C*

The TEM examination revealed some precipitated particles, but no signs of the initial stage of the solid solution decomposition were exhibited by the solid solution grains of the ternary Mg-5.7%Dy-7.6%Sm alloy with small Dy content after solution treatment. Such signs are usually represented by lines of two-dimensional diffraction and superlattice reflections. The typical structure of the alloy and its diffraction pattern are shown in Fig. 3. Separate extinction lines are seen in the TEM structure image (Fig.3a) and the isolated large reflections of the Mg-based solid solution are seen in the corresponding diffraction pattern (Fig. 3b).

The next stage of the decomposition of the Mg based solid solution in the Mg-5.6%Dy-7.6%Sm alloy was observed by weakness or disappearance of the straight lines indicating the existence of GP-zones and the appearance of new superlattice reflections typical of the decomposition of the Mg-based solid solution in the binary Mg-Dy alloys [7] and other Mg-based alloys containing the rare-earth metals of yttrium subgroups (Y, Gd, Dy) with the formation of the metastable β′ phase with base-centered orthorhombic lattice (cbco) [8]. The images of the Mg grain fields remained uneven, but rougher than before, without any clearly visible precipitates (Fig.4a). The arrangement of the superlattice reflections become more complex, but all of them are observed within the basal planes or their tracks in the reciprocal Mg lattice. All superlattice reflections are present at all Mg [100]* radius-vectors of the Mg reciprocal lattice, dividing them to four equal parts. One of such diffraction patterns is shown in Fig.4b. The diffraction patterns obtained from the Mg lattice in the Mg-5.7%Dy-7.6%Sm alloy confirmed also the similarity of the alloy structure at this stage of the Mg-based solid solution decomposition to that observed in the binary Mg-Dy and other Mg-based alloys with rare-earth metals of the yttrium subgroup (Y, Gd, Dy), which contain the metastable (cbco) β′ phase. This state of the solid solution decomposition in the Mg-5.7%Dy-7.6%Sm alloy corresponds to the hardness maximum after aging at 200°C for 32 h.

At the latest stage of the solid solution decomposition of the Mg-5.7%Dy-7.6%Sm alloy at 250°C (softening after hardness maximum), coarse plate-like crystals are formed, which are present on three planes in the Mg hexagonal lattice. The micrograph of this structure presented in Fig.5a exhibits the plate-like shape of the precipitated particles. The particles are clearly outlined in the structure. The diffraction pattern taken from the area shown in Fig.5a is presented in Fig.5b. The number of superlattice reflections is smaller, and they are very fine. Nevertheless, the reflections can be distinguished only in the tracks of the basal planes of the Mg reciprocal lattice. (It would be reasonable to suppose that the coarse plate-like precipitates belong to one of the equilibrium phases ($Mg_{41}Sm_5$ or $Mg_{24}Dy_5$ [6])).

Taking into consideration the Mg-Dy-Sm phase diagram [6], two processes of the decomposition of the Mg based supersaturated solid solution could be expected in the ternary Mg-Dy-Sm alloys. Each of them should be completed with the formation of two equilibrium phases existing in the adjoining Mg-Dy and Mg-Sm binary systems, $Mg_{24}Dy_5$ and $Mg_{41}Sm_5$, respectively. Only such binary compounds are in equilibrium with Mg solid solution in the ternary Mg-Dy-Sm system.

4. Conclusions.

1. The decomposition of the Mg based supersaturated solid solution in the Mg-Dy-Sm alloys becomes successively less intense with increasing Dy/Sm concentration ratio.

2. The decomposition of the Mg based supersaturated solid solution occurs by two main stages. At the first stage, the strengthening of the alloys is insignificant and, at the second stage, the hardness abruptly increases, reaches maximum and decreases with increasing aging time.

3. Addition of Dy to the Mg-Sm alloys enhances their age hardening. On the other hand, the addition of Sm to the Mg-Dy alloys also increases their strengthening. The highest hardness of the Mg-Dy-Sm alloys is reached at a Dy/Sm ratio of about 1.5.

4. The decomposition of the Mg based supersaturated solid solution in the Mg-Dy-Sm alloys is accompanied by the formation of precipitates typical of the binary Mg-Sm and Mg-Dy alloys. They include GP-zones in the form of the rods directed along the hexagonal axis of the Mg lattice, ordering of the Mg_3Cd type (β″), formation of the metastable base-centered orthorhombic (cbco) β′ phase, and equilibrium phases. The highest hardness is reached due to the formation of the metastable cbco β′ phase. The precipitation of supposedly equilibrium phase is also observed at the grain boundaries of the Mg based solid solution.

5 The plate-like precipitates formed upon the decomposition of the Mg based supersaturated solid solution in the ternary Mg-Dy-Sm alloys contain both Dy and Sm in different ratios.

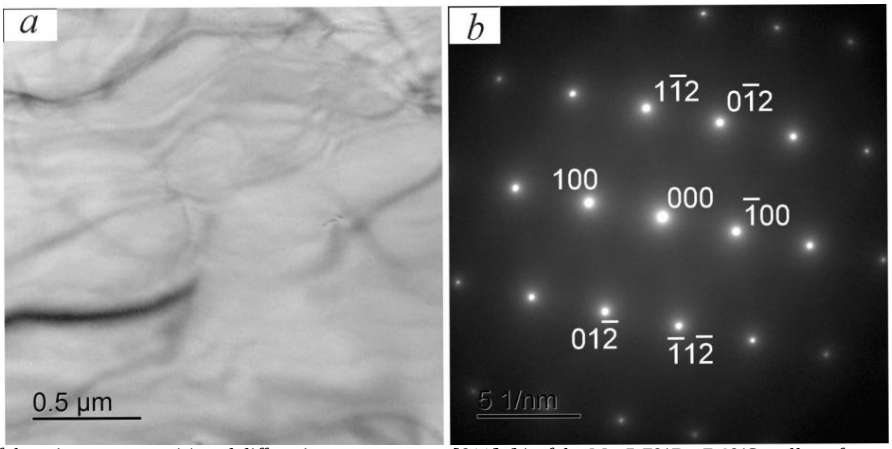


Fig.3. *TEM image of the microstructure (a) and diffraction pattern, zone [011] (b) of the Mg-5.7%Dy-7.6%Sm alloy after solution treatment and natural aging*

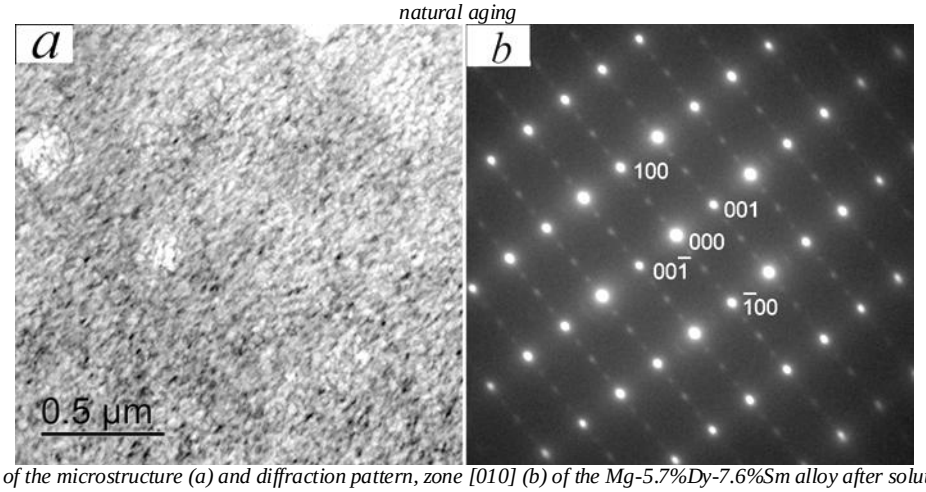


Fig. 4. *TEM image of the microstructure (a) and diffraction pattern, zone [010] (b) of the Mg-5.7%Dy-7.6%Sm alloy after solution treatment and aging at 200°C for 32h*

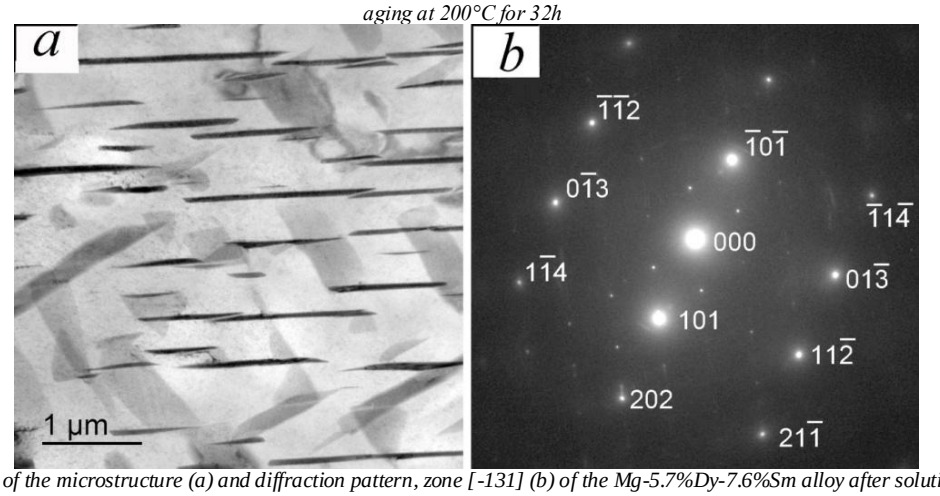


Fig.5. *TEM image of the microstructure (a) and diffraction pattern, zone [-131] (b) of the Mg-5.7%Dy-7.6%Sm alloy after solution treatment and aging at 250°C for 128 h.*

5. References

1. L. Mordike, T. Ebert, Magnesium: properties-applications-potential, Mater. Sci. Eng. A. 302 (2001) 37-45.
2. Jain Chao-chi, Koo Chun-hao, Creep and corrosion properties of the extruded magnesium alloy containing rare earth, Mater. Trans. 48 (2007) 265-272.
3. Z. Yang, J.P. Li, J.X. Zhang, G.W. Lorimer, J. Robson, Review on research and development of magnesium alloys, Acta Metall. Sin. (Engl. Lett.). 21 (2008) 313-328.
4. L.L. Rokhlin, Magnesium alloys containing rare earth metals. London and New York, Taylor & Francis, (2003).
5. Zhu S., Easton M.A., Abott T.B., Nie J-F., Dargusch M.S., Hort N., Gibson M.A, Evaluation of Magnesium Die-Casting for Elevated Temperature Applications: Microstructure, Tensile Properties, and Creep Resistance, Metall. Mater. Trans. A. 46 (2015) 3543-3554.
6. E.A. Lukyanova, L.L.Rokhlin, T.V.Dobatkina, I.G.Korolkova, I.E.Tarytina, Investigation of the Mg-rich part of the Mg-Dy-Sm phase diagram,J. Phase Equilib. Diff. 37 (2016) 664-671.
7. L.L. Rokhlin. Investigation of the supersaturated solid solution decomposition in the alloys of magnesium with dysprosium, Fiz. Met. Metalloved. 55 (1983) 733-738 (in Russian).
8. J.-F. Nie, Precipitation and Hardening in Magnesium Alloys, Metall. Mater. Trans. A. 43 (2012) 3891-3939.

Effect of additional alloying on stabilization of structural state and mechanical properties of industrial magnesium-rich Al-Mg alloys

Alla Berezina., Tetiana Monastyrska., Oleh Molebny
G.V. Kurdyumov Institute for Metal Physics of the NAS of Ukraine, Kyiv, Ukraine
E-mail: beres@imp.kiev.ua, monast@imp.kiev.ua, moleb@imp.kiev.ua

Absract: *Influence of small Sc, Ag, Zr, Ti, Mn addition on the stabilization of the structural state, the formation mechanisms and kinetics of the phase growth during the aging, and also technological casting properties in the industrial Al-Mg alloys were investigated. It has been established: maximum strengthening in these alloys is reached after the nature aging due to the precipitation of ordered Al_3Mg phase that is isomorphic to the matrix. However, under prolonged nature aging the stable Al_3Mg_2 phase is precipitated in the matrix and on the grain boundary. It is accompanied by fall of the plasticity and decreasing the volume fraction of the strengthening Al_3Mg phase. It is succeeded completely to prevent the formation of the stable phase under prolonged nature aging in the alloys quenched in the oil and additional alloyed by Sc or Ag. Also Ag affects the cracking under the crystallization of alloys favorably. Using the complex of the Zr, Ti, Mn and Sc alloying elements increases the strength properties of the alloy at the quenched state slightly, but accelerates the formation of the stable phase during the nature aging.*

KEYWORDS*: Al-Mg ALLOYS, PRECIPITATION STRENGTHENING, STRUCTURE, NATURAL AGING, STABLE PHASE, METASTABLE PHASE*

1. Introduction

It is known that Al-Mg alloys have a high solubility of Mg in Al, but they are not strengthened during the ageing [1]. The study of the kinetics and the morphology of the ageing of Al-Mg alloys (the concentration of Mg was from 3% to 15%) showed that the alloys are aged with the formation of the stable icosahedral giant Samson Al_3Mg_2 phase [2]. The phase particles are formed heterogeneously on the defects and on the grain boundaries, they are not strengthening particles.

Al-(8-12)%Mg alloys are basic alloys of durable lights corrosion-resistant casting alloys with satisfactory castings properties. An essential disadvantage of these alloys is the sensitivity of the properties of these alloys to the natural ageing. In the process of natural ageing the alloys are strengthening on 25-70% depending on the concentration of Mg and duration of ageing, while the plasticity reduces from 20 to 2%. It was found [3,4] that the hardening in these alloys during the natural ageing is related to the precipitation of fine of coherent phase of Al_3Mg ordering as $L1_2$ (β''-phase). Decreasing of plasticity is related to the presence of areas free of precipitating of strengthening β''-phase. These areas appear due to the formation of the stable Al_3Mg_2 phase on the boundaries of grains.

In our earlier studies [5,6,7] structural changes during aging process of the modeling Al-(10-14)%Mg alloys alloyed with (0.1–0.3)%Sc, (0.15–0.5)%Ag were investigated. It allowed determining the optimal concentrations of Mg, Sc and Ag that allows stabilizing the structural state in the alloy under prolonged nature aging.

The objects of this investigation are the industrial Al8 and Al27 alloys on the base of Al-10%Mg additional alloyed by 0.15%Sc and 0.1%Ag. The aim of the investigation is the study of the Sc, Ag influence on the structural change, the mechanical and casting properties this alloys.

2. Experimental

The experimental alloys were melted on a base of industrial high-strength corrosion-resistant alloys Al8 (alloy A, table 1) and Al27 (alloy D, table 1). In addition the alloys were alloyed with Sc, Ag, Zr, Ti, Mn. The alloys were prepared using aluminium A99, magnesium Mg95. The refractory elements were additional alloyed by the ligatures: Al-2%Sc, Al-4%Zr, Al-5%Ti and Al-5%Mn. The alloys were melted in the graphite crucible in the resistance furnace under the protective Ar atmosphere. The compositions of the melted alloys are summarized in the Table 1.

For investigation of the structural and phase transformation in Al – Mg alloys the hardness, X - ray methods; metallography and transition electron microscopy (TEM) methods were used. TEM was performed using JEM-2000FXII instrument in the transition and scanning mode. The hardness was measured by Vikkers method at loading of 5 kg and the duration for the 12c. The stress-strain properties and technological casting properties such as the fluidity, shrinkage and the ability to the shrinkage cracks [8] have been investigated.

Table 1. The chemical composition of the melted alloys

Alloys	Mg	Si	Mn	Ti	Zr	Sc	Ar
A	9.74	-	-	-	-	-	-
B	10.5	-	-	-	-	0.13	-
C	10.5	0.07	-	-	-	-	0.08
D	9.2	-	0.36	0.23	0.13	-	-
E	10.5	0.06	0.33	0.36	0.3	0.12	-

3. Results and discussion

3.1. Smelting of the trial compositions of industrial alloys, alloyed with optimum elements (Ag, Sc etc); selection of their homogenization and quenching regimes

The metallographic investigation of the structure of the alloys in the initial state has been carried out. The structure of the A, B, C alloys is dendritic. The nonequilibrium Al_3Mg_2 phase is located at the grain boundary and in the interdendritic space (Fig. 1). The dendritic parameter is not affected by the additional alloying of the A alloy with 0.13% Sc (alloy B) or by 0.08% Ag (alloy C) (Table 2).

Table 2. The dendritic parameter d of the studied Al-Mg alloys

d, μm	Alloys		
	A	B	C
d_{min}	10	8	10
d_{max}	14.5	13.5	14
d	12.6	11.1	12.2

In the D and E alloys the undendritic crystallization structure is observed. In this structure the excess phase is substantially observed on the grain boundary. Large intermetallides of the refractory compound Ti, Zr, Mn are present in the matrix (Fig. 1).

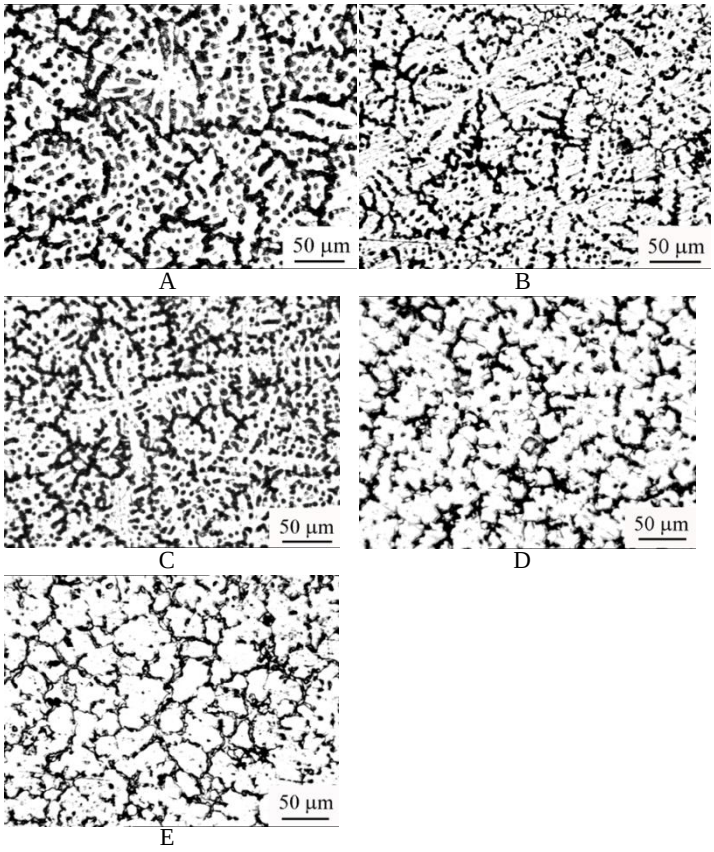


Fig. 1 The structure of the cast alloys.

The grain sizes *D* and sizes of the primary particles of intermetallides *d* are summarized in the Table 3. (The number of measured grains was $N_d \geq 200$ and the number of measured particles was $n_d \geq 50$). The volume fraction of particles is increased in the E alloy under additional alloying by Sc.

Table 3. The grain sizes and the intermetallide sizes in the C and D alloys

Alloys	The grain size, μm			The intermetallide size, μm		
	D_{min}	D_{max}	D	d_{min}	d_{max}	d
D	11.6	82.7	46	1	21.4	3.7
E	5.0	71.0	44	1.5	35.2	4.1

According to earlier investigations the homogenization condition at 430 ºC during 20 hours was chosen. For decreasing the internal stress in the alloy the quenching was carried out from the homogenization temperature in the oil at the temperature of 50 ºC.

3.2. The investigation of ageing processes

Influence of the transition metals Sc, Zr, Ti and Mn on the structural state of the ingots during high-temperature heat by the homogenization and under the aging at the region of the formation of stability β-phase was studied.

The study of the macrostructure of the ingot of the A alloy, where the antirecrystallization elements are absent, has shown that wide variance of grain sizes along the profile of the ingot is observed after homogenization: a hoop from big grain (size of 3-2.5 mm) with fine-grained centre with the grain size of 0.3-0.5 mm (fig. 3). Addition of 0.13 %Sc to this alloy puts out such heterogeneousness in the ingot (alloy B). The processes of the anomalous collecting recrystallization of the grains with the formation of separate big grains have a place after alloying with Ag (alloy C). In alloys of Al-27 type (alloys D and E) containing the high concentration of the anticrystalization elements the homogeneous fine-grained structure with the grain size of 40-60 μm is kept after the homogenization (fig. 2).

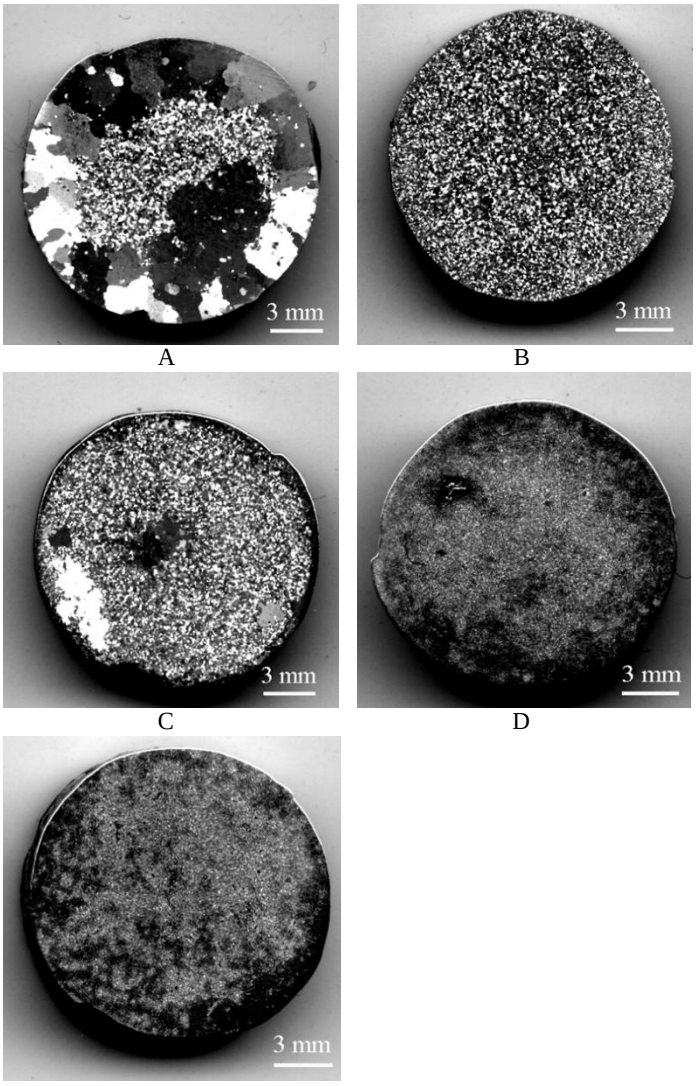


Fig. 2 The macrostructure of the alloys homogenized at 430 ºC for 20 hours.

The non-equilibrium Al_3Mg_2 phase of crystallization origin is observved after homogenization. After following aging at 220 ºC during 25 hours the equilibrium β phase is precipitated uniformly on the grain in the alloys of Al-8 type (alloys A, B, C) and nonuniformly in the alloys of Al-27 type (fig. 3). Decrease the aging temperature to 130 ºC, when the β´- phase is precipitated results in the formation of rosette nonuniformly in the B, C and E alloys.

Obtained results shown that the using the complex alloying with the transition metals Sc, Zr, Ti and Mn (C and E alloys) results the modification of the ingot structure. The small grain of the ingot with the size of 40-60 μm is observed after the homogenization at 430 ºC during 20 hours. The strong antirecrystallization effect is observed. After following aging in these alloys the equilibrium phase precipitates heterogeneously in the main at the region connecting with the grain boundary. In the alloys alloyed only with Sc and Ag, in which the recrystallization takes place (alloys B, C), the distribution of the β-phase is uniform.

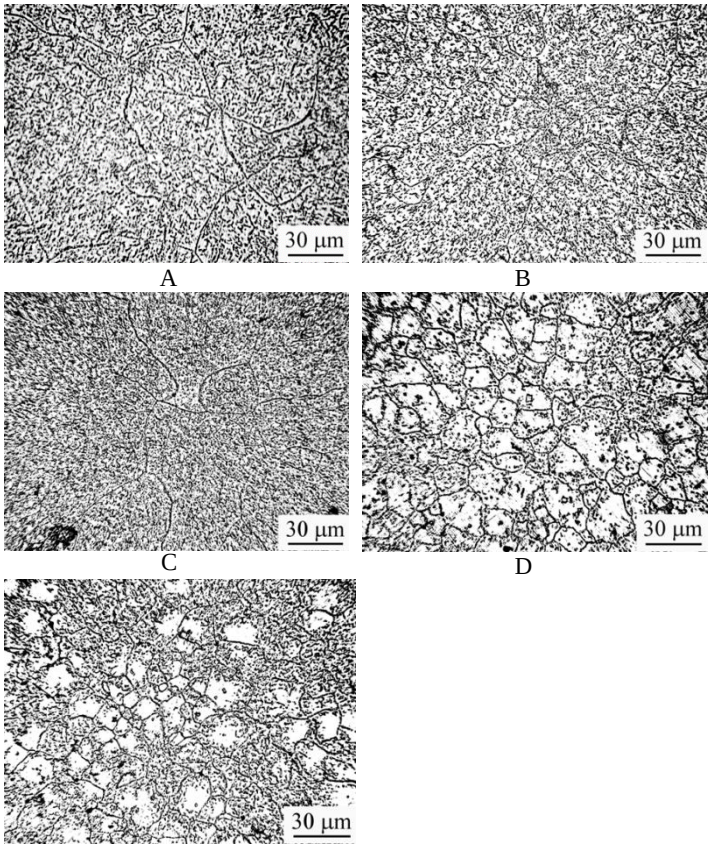


Fig. 3 The structure of the alloys aged at 220 °C for 25 hours.

3.3. The temperature and time stability of structural states. The mechanical properties of the alloys

Investigation of the change of strength properties of alloys during the aging at the region of the formation of the hardening β' phase showed that the maximal strengthening is reached after aging at 130 ºC during 50 hours. The hardness values of the alloys in the initial state and after the natural aging are summarized at the Table 4.

Table 4. The hardness change depending on the thermal treatment (HV, kgs/mm^2)

Alloys	As cast	Homogenization 430ºC 20 hours + quenching in the oil 50ºC	Aging 220ºC 25 hours	Aging 130ºC 50 hours	Natural aging, 2 years
A	94	104.4	107.3	127.2	140
B	86.2	101.6	108.8	133	145
C	97.8	97.8	98.4	125.4	139.6
D	93.4	78.8	97.8	134	112.4
E	105.1	118.3	115.8	130.4	138.8

The TEM study of all alloys after aging at 130 ºC for 50 hours showed that the plate-like hexagonal β' phase squeezing the dislocations to the matrix is present (alloy A, fig. 5). The branching of the plate of the β' phase and the appearance of cellular contrast between plates have a place. It indicates the formation of the equilibrium unstrengthening β phase. The fine-dyspersed particles of the Al_3X (X= Sc, Zr) phase with size of 20-30 nm are present in the matrix of the B, D, E alloys (Fig. 4, alloy D). These particles are coherently connected with the matrix. The density of their precipitation is $N_v \sim 10^6$ 1/sm^3.

Maximum strengthening is reached after the natural aging due to the continuous decomposition with precipitation of the strengthening metastable β'' phase which is coherent to the matrix and forms the static deformation. The density of the precipitation of these particles with the size of 2-3 nm reaches to ~ 10^{18} 1/sm^3 (Fig.4, alloy B).

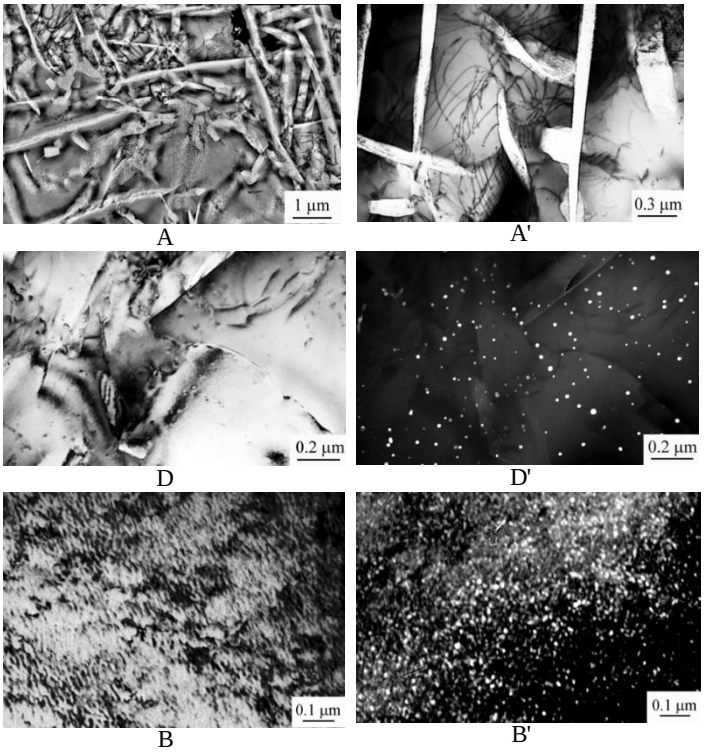


Fig. 4 The morphology of the precipitations in the alloys. A, B, D – bright - field, A', B', D' – dark – field.

The metallographic study of the structure of A, B and C alloys after prolonged natural aging (10 years) showed that it is impossible to prevent the formation of the stable unstrengthening phase in the matrix under quenching of this alloys in the water after homogenization (Fig. 6, A and B alloys). It should be noted that the presence of Sc and Ag decreases volume fraction of this phase significantly. The quenching in oil heated to 100 ºC decreases the internal stress in the matrix and the formation of the β′and β - phases in the B and C is completely inhibited (Fig. 5, B′ and C alloys).

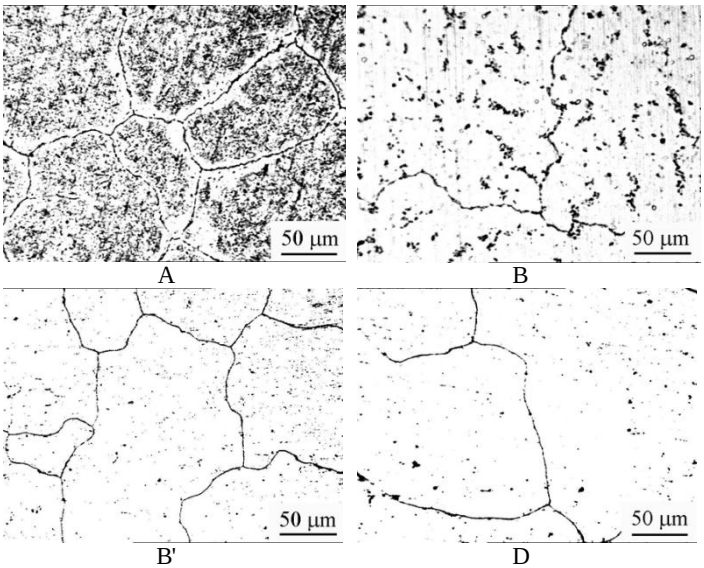


Fig. 5 The structure of the naturally aged alloys during 10 years. A, B - the water quenching, B', C - the oil quenching.

The test probe was used to determine the alloys casting properties. It allows defining the fluidity, the linear shrinkage and the degree of the cracking simultaneously under cast. The test probe is the U-liked mould that is split in vertical plane. The mould was uncovered after the cast of the probe and the solidification of the alloy. The fluidity of the alloy was determined by the length of filling of the U-liked canal. The crack width as the distance between relevant points located on the axis line of the probe canal was defined with the accuracy about 0.05mm. The linear shrinkage in the complex probe was determined by the shrinkage of the central stick obtained in the vertical canal. The relative value of the linear shrinkage was defined. Obtained casting and stress-strain properties of the experimental alloys are summarized in the Table 5.

Table 5. The casting and stress-strain properties of the experimental alloys

Alloys	The casting properties			The stress-strain properties					
	The fluidity mm	The relative linear shrinkage %	The cracking mm	Homogenization at 430ºC, 20 hours, the quenching in the oil			The nature aging during 2 hours		
				σ_B, MPa	σ_{τ}, MPa	δ, %	σ_B, MPa	σ_{τ}, MPa	δ, %
A	213	1.04	0.26	360	190	20	310	240	2
B	227.7	1.08	0	360	200	20	440	300	25
C	198.6	1.05	0	355	185	20	420	280	20
D	218.4	1.07	0	430	200	15	410	250	1
E	227.3	1.00	0.23	450	200	12	400	230	1

4. Conclusion

1. Maximum strengthening in these alloys is reached under the nature aging due to the precipitation of ordered Al_3Mg phase that is isomorphic to the matrix. However, under prolonged nature aging the stable Al_3Mg_2 phase is precipitated in the matrix and on the grain boundary. It is accompanied by fall of the plasticity and decreasing the volume fraction of the strengthening Al_3Mg_2 phase. The formation of the stable phase is accelerated under the formation of the internal stress by the quenching of the alloys.
2. It is succeeded completely to prevent the formation of the stable phase under prolonged nature aging in the alloys of Al-8 type additional alloyed with Sc (~0,15%) or Ag (~0,15%) and quenched in the oil.
3. The Sc alloying removes the tendency of the alloys to form the shrinkage crack and facilitates to increase the fluidity. Also Ag affects the cracking under the crystallization of alloys favorably.
4. Using the complex of the Zr, Ti, Mn and Sc alloying elements increases the strength properties of the alloy at the quenched state slightly, but accelerates the formation of the stable phase during the nature aging.

5. References

[1] Stroganov G,B,, Moskva, Vysokoprochnyye liteynyye alyuminiyevyye splavy, Metallurgiya, 1985 (in Russian).

[2] Mondolfo L.F., Aluminium Alloys: Structure and Properties, Boston, Butterworth, 1976.

[3] Gault C., A.Dauger and P. Boch - Decomposition of aluminium-magnesium solid solutions studied by ultrasonic measurements of elastic properties and electron microscopy, Acta Met., 28, 1980, 51.

[4] Sato T., Y. Kojima, T. Takahashi, Modulated structures and GP Zones in Al-Mg Alloys Metall. Trans., 13A, 1982, 1373.

[5] Berezina A.L., T.A. Monastyrskaya, O.A. Molebny - Structure stabilization Al-(10-14)%Mg alloys during the long-term natural ageing, Mater. Science Forum, 519-521, 2006, 1853.

[6] Berezina A.L., T.A. Monastyrskaya, O.A. Molebny, Vlijanie mikrolegirovanija Sc na stabil'nost' strukturnyh sostojanij v litejnyh Al-Mg splavah pri dlitel'nom estestvennom starenii. Metallofizika i novejshie tehnologii, 29, 2007, 67 (in Russian).

[7] Tetiana O. Monastyrska, Alla L. Berezina, Oleh A. Molebny, Svitlana L. Polyvoda, Andrii V. Kotko, Mykola A. Skoryk. Peculiarities of nanostructured state formation in heat-treatable Al-Mg alloys, Applied Nanoscience, 10(8), 2020, 2731.

[8] Nehendzi Ju.A., Kupcov I.V. Kompleksnaja test proba dlja opredelenija litejnyh svojstv splavov. Leningrad, Nauka, 1967 (in Russian).

Structure and magnetic properties of 1.4541 stainless steel

Demidenko Olga[1], Vetcher Alexander[1], Popescu Ana Maria[2], Constantin Virgil[2], Neacsu Elena Ionela[2], Donath Cristina[2]
Scientific–Practical Materials Research Centre NASB, Minsk, Belarus [1]
"Ilie Murgulescu" Institute of Physical Chemistry, Bucharest, Romania[2]
orion_minsk@tut.by

Abstract: *The influence of corrosion action of Mediterranean, Black and Aegean sea waters on 1.4541 stainless steel structure and magnetic properties is studied. Samples of investigated stainless steel was exposed by marine corrosion action at 25ºC. Crystal structure before and after corrosive action of all sea waters types was characterized by X-ray diffraction (XRD) in CuKα-radiation at room temperature. Temperature dependences of the specific magnetization were studied by the ponderomotive method in the temperature range of 77 - 1100 K in the magnetic field of 0.86 Tesla. It revealed, that crystal structure and specific magnetic characteristics of 1.4541 alloy are resistant to corrosion action of Mediterranean, Black and Aegean sea waters.*
Keywords*: SEA WATERS, HYSTERESIS LOOPS, XRD ANALYSES, MAGNETIZATION*

1. Introduction

Number of industries has no alternative to use a corrosion-resistant steels and alloys based on nickel. Most of metal ware is operating in natural environments. Application field of stainless steels and alloys is very wide: from the heavy engineering industry and power engineering to mechanics and electronics. A problem of corrosion resistance of such materials is still actual. Therefore, a clear data of marine corrosion resistance, mechanical and physical properties of stainless steels, stability properties, the temperature ranges of usage and knowledge of their processing and exploitation is a key to significant economy.

Stainless steel containing 13% chromium and additionally alloyed with nickel, as well as a small amount of silicon and manganese, shows high anti-corrosion properties [1, 2]. Corrosion resistance is the main and most important property of high chromium stainless steels, as corrosion losses can be enormous. The chromium content in steel over 12% provides high resistance to oxidation and heat resistance [3, 4]. It was found that varying the carbon content in the range of 0.08-0.25% affects the quality characteristics and changes the properties. The published results are ambiguous, which allows us to continue and expand the study of this issue.

The problem of corrosion resistance of stainless steels and alloys based on chromium and nickel, like nickel-based alloy 1.4541, is still relevant. Therefore, leading research centers carry out comprehensive studies of such materials [5-7]. The research results presented in the scientific references do not allow explaining and predicting the corrosion resistance during operation under conditions of exposure to sea water.

The aim of this work is to study the effect of the corrosive effects of sea waters with different salt content on the structure and magnetic properties of functional nickel-based alloy 1.4541. The relevance of the goal and objectives is that, to ensure long service life in an aggressive marine environment, it is necessary to use corrosion-resistant materials with specific features of the crystal structure, capable of ensuring the resistance of the material to external factors, in particular to the effects of sea waters.

2. Experimental part

Chemical composition of investigated 1.4541 samples was: C-0.08%, Si-1%, Mn-2%, P-0.045%, S-0.03%, Cr-18%, Ni-11%, Fe-68%,Ti-0.15%. Corrosion tests of functional 1.4541 alloy were carried out at a temperature 25ºC in the waters of the Aegean, Black and Mediterranean seas.

X-ray analysis of the investigated alloy before and after corrosion action of sea waters was carried out on the modified and automatized apparatus "DRON-2" in CuKα – radiation in the $20° \leq 2\theta \leq 100°$ angle range at room temperature. X-ray patterns are received with automatic recording of the reflexes intensities with a 0.03° scaning step and the exposure time of 2-3 s. For the purpose the crystal cell parameters determining were scanned the separate reflexes with a step of 0.01° with the exposure to 10 seconds. The processing of X-ray patterns is carried out using the FullProf Suite program, which is based on the Rietveld method to clarify the parameters of the crystal cell. The lattice parameter determination error was ± 0.0003 nm. The average crystallite size is calculated by the Debye-Scherrer formula.

The temperature dependences of the specific magnetization were studied before and after corrosion action of sea waters in the 77 – 1100 K temperature range by the ponderomotive method in a magnetic field of 0.86 T. The relative error in determining of the specific magnetization value is about 4%. We also studied the field dependences of magnetization on a vibration magnetometer of the universal measuring system "Liquid Helium Free High Field Measurement System" from "Cryogenic Ltd" at 77 and 300 K in fields up to 14 T.

3. Results and discussion

X-ray phase analysis of the alloy 1.4541 (Fig. 1) showed that the alloy contains two phases – γ-phase of iron sp. gr. $Fm\bar{3}m$ and α'-phase sp. gr. $Im\bar{3}m$. The unit cell parameter was 0,3595 nm for γ-phase and 0,2877 nm for α'-phase of iron with phase ratio 6/1. The average crystallite size is 16,86 nm, and the dislocation density $3{,}52 \cdot 10^{-3}$ nm^{-2}.

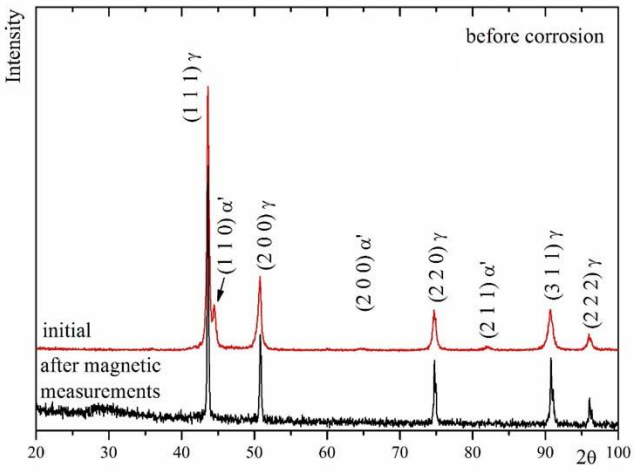


Fig. 1 *X-ray patterns of 1.4541 before and after high temperature annealing .*

Fig. 2 shows the temperature dependence of the specific magnetization of the 1.4541 alloy before corrosive action. At liquid nitrogen temperature, the specific magnetization is 12,4 A·m^2·kg^{-1}. Curie temperature determined from dependence $\sigma^2 = f(T)$, equals 890 K. It should be noted that the $\sigma = f(T)$ dependence at cooling is completely different from $\sigma = f(T)$ at heating, that is, the heating of the 1.4541 alloy to 1060 K is irreversible. The specific magnetization value at nitrogen temperature decrease in 5,5 times,

and to be 2,25 $A \cdot m^2 \cdot kg^{-1}$. For understanding this fact, it was carried out X-ray study of 1.4541 samples after high temperature annealing during specific magnetization measurements, results of which are presented as comparison on fig.1. X-ray phase analysis showed that such treatment causes phase α'–γ transformation, on the X-ray there are only reflexes from austenitic γ-phase. Slow cooling of the alloy leads to recrystallization of the alloy, the average grain size increases to 41,71 nm, and the dislocation density increases to $5,75 \cdot 10^{-3}$ nm^{-2}. Magnetic hysteresis loops at 77 K and 300 K (Fig. 3) also confirm the presence of only austenitic γ-phase. As a result of heating the sample to 1100 K, the martensitic-phase of iron disappears, and the alloy becomes completely austenitic.

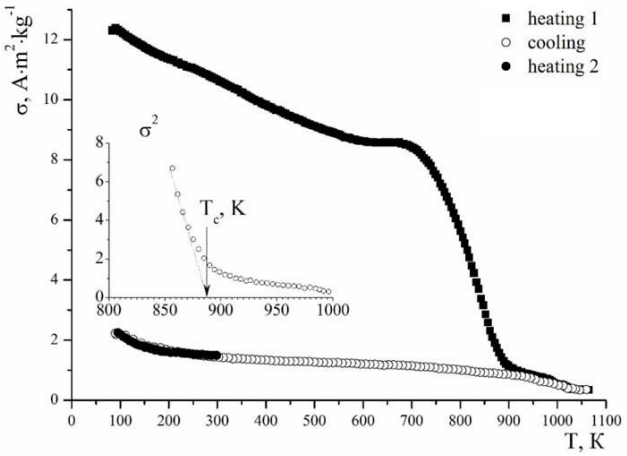


Fig. 2 *Temperature dependences of the specific magnetization of the 1.4541 alloy before the corrosive effect of sea waters*

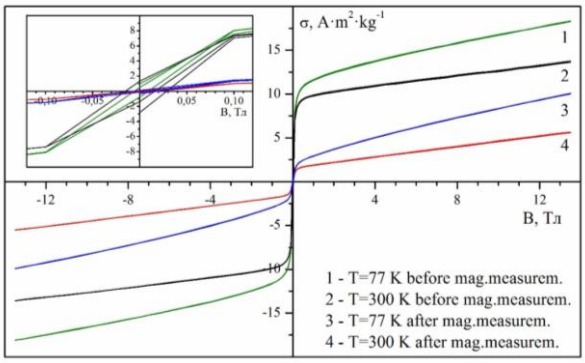


Fig. 3 *Magnetic hysteresis loops of the 1.4541 alloy before and after high-temperature annealing at 77 K (1 and 2) and 300 K (3 and 4)*

Figure 4 shows the diffraction patterns of the 1.4541 alloy before the corrosion action of different sea waters. The analysis of the diffraction patterns showed that crystal structure of 1.4541 in case of longtime exposure in seawater has good corrosion resistance, the structure of the alloy was preserved. Table 1 shows the crystal cell parameters of the α' and γ-phases of 1.4541 alloy, as well as the average grain size and dislocation density. Formation of iron oxides and hydroxides on the surface of the samples is not observed.

4. Summary

It was found that 1.4541 alloy has two crystalline phases – austenic γ-phase $Fm\bar{3}m$ sp. gr. and ferritic α'-phase $Im\bar{3}m$ sp. gr. The cell parameter a before corrosion action is 0.3595 nm for the γ-phase and 0.2877 nm for the α'-phase with a phase ratio of 6/1. X-ray patterns analysis after different seawaters action showed that in all cases 1.4541 alloy structure was preserved. The formation of iron oxides and hydroxides on the surface of the samples is not observed.

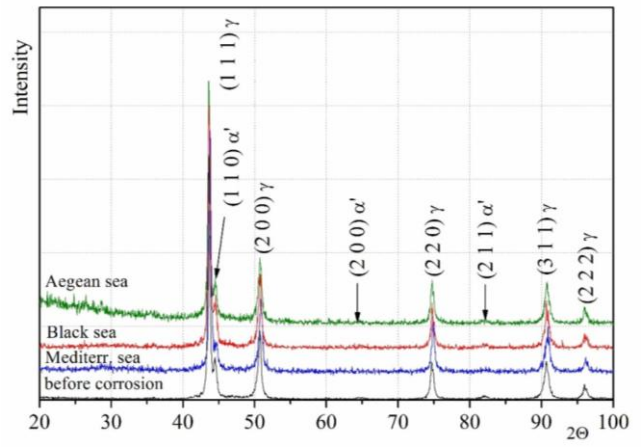


Fig. 4 *X-ray patterns of 1.4541 before and after corrosion action of seawaters .*

Table 1: *Crystal cell parameters of the α 'and γ-phases of the 1.4541 alloy, the average grain size and the density of dislocations.*

Corrosion media	γ-phase a, nm	α'-phase a, nm	average crystallite size d, nm	dislocation density $\delta \cdot 10^{-3}$, nm^{-2}
Before corrosion	0,3598	0,2879	16,86	3,52
Mediterranean Sea	0,3596	0,2874	16,08	3,86
Black sea	0,3589	0,2870	16,61	3,62
Aegean sea	0,3597	0,2879	16,15	3,83

5. Acknowledgments

The financial support of the Romanian Academy and the Research Foundation of NAS of Republic Belarus (bilateral project 2018-2020) is acknowledged.

6. References

1. S.S.M.Tavares, J. M. Pardal, T. R. B. Martins, M. R. da Silva, Journal of Materials Engineering and Performance, **26**, **6**, 2512 (2017).
2. B. Liu, X. Wei, W. Wang, J. Lu, J. Ding, Solar Energy Materials and Solar Cells, **170**, 77 (2017).
3. L. Tale, C. Keller, International Journal of Mechanical Sciences, **146–147**, 527 (2018).
4. Z. Wang, T.A. Palmer, A.M. Beese, Acta Materialia, **110**, 226 (2016).
5. S.S. Sawant, B.D. Gajbhiye, S. Tyagi, C.S. Sona, R. Divya, C.S. Mathpati, A. Borgohain, N.K. Maheshwari. Indian Chemical Engineer, **59**, **3**, 242 (2017).
6. S. Wang, J. Ding, H. Ming, Z. Zhang, J. Wang, Materials Characterization, **100**, 50 (2015).
7. V.N. Rubchevsky, Yu.A. Chernyshov, V.V. Zelensky, A.I. Savenyuk, S.V. Nesterenko, UgleKhimicheskiy Zhurnal, **3-4**, 41 (2013).

Microstructure and performance characteristics of experimental forged billets of ultrafine-grained structure two-phase titanium alloy VT8M-1

Grigory Dyakonov*, Tatyana Yakovleva, Andrey Stotskiy, Irina Semenova
Institute of Physics of Advanced Materials, Ufa State Aviation Technical University, 12 K. Marx str., Ufa 450008, Russia
Dgr84@mail.ru

Abstract: *The UFG structure in the VT8M-1 alloy was formed by rotary swaging (RS). Experimental forged billets of ultrafine-grained structure (UFG) were obtained by isothermal die forging (IDF). The structural parameters and the homogeneity of the UFG structure were analyzed. Microstructure and mechanical properties of experimental workpieces of the ultrafine-grained VT8M-1 alloy produced by isothermal die forging was analyzed. The relationship between the microstructure and mechanical properties of the forged workpieces of the UFG VT8M-1 alloy is discussed.*
Key words: *TWO-PHASE TITANIUM ALLOYS, ULTRAFINE-GRAINED STRUCTURE, ROTARY SWAGING, FORGED BILLETS, STRENGTH*

1. Introduction

Among structural materials, titanium alloys are widely applied in aviation and engine building due to their high specific strength, corrosion resistance and specific hot strength [1]. For example, the two-phase Ti alloy VT8M-1 (Ti-5.7Al-3.8Mo-1.2Zr-1.3Sn) is applied in modern engine building for the production of compressor blades. Compressor blades operate under the severe conditions of high static and dynamic loads, corrosive attack and temperature exposure. In this connection, a higher set of requirements is imposed on them, such as a combination of high strength, ductility, fracture toughness and fatigue resistance.

The conventional technology for the fabrication of blade workpieces from Ti alloys, having a rather complex surface configuration, is die forging [2]. It is known that the temperature of isothermal forging for coarse-grained Ti-based materials is about 950 °C, and the use of UFG billets in the shape-forming of blades creates an opportunity to implement isothermal forging at lower temperatures of 750-780 °C. The decrease in the forging temperature is related to the manifestation of superplasticity in UFG materials at lower temperatures and higher strain rates [3]. Such a temperature range makes it possible to preserve a homogeneous UFG structure, which ensures a higher level of properties in an experimental item.

2. Material and experimental procedure

For the investigation, we used the VT8M-1 alloy (VSMPO-AVISMA Corporation, Russia) with the following composition: Ti–5.7Al–3.8Mo–1.2Zr–1.3Sn–0.16Fe (wt.%). The β-transus temperature in the alloy is 980 ± 5 °C. The ultrafine-grained structure of the VT8M-1 alloy was formed by rotary swaging (RS) at 750 °C with a gradual reduction along the diameter of the billets from 70 to 32 mm (true strain e ≈ 1.56, the strain rate was higher than 300 mm s-1).

An experimental forging simulating a compressor blade was produced by IDF at a temperature of 780±10°C (figure 1).



Fig. 1. *Experimental forging produced from the UFG alloy VT8M-1.*

The microstructure was characterized by scanning electron microscopy (SEM) using a JSM 6390 microscope, and by transmission electron microscopy (TEM) using a JEM-2100 microscope. Tensile mechanical tests of flat specimens with a gage length of 16 mm and a width of 3 mm, cut out from the root and airfoil of the experimental forging, were performed using an Instron universal testing machine at room temperature with a strain rate of 1×10-3 s-1 in compliance with ASTM E8/E8M.

In this connection, the aim of the present paper is to study the effect of isothermal forging at lower temperatures on the microstructure of the UFG VT8M-1 alloy, and also to evaluate the mechanical properties of the produced workpiece.

3. Results and discussion

The microstructure of the forged workpieces produced by IDF (T=780 °C) is shown in figure 2. The SEM study of the microstructure of the forgings revealed a similar character of microstructure in the airfoil part and in the root part. The primary α-phase grains are elongated along the deformation direction and their thickness is 2-3 μm (figure 2 a,c). As it was noted above, such an elongated shape formed at the stage of processing by rotary swaging.

TEM study at a larger magnification revealed (figure 2b,d) that the microstructure of the (α+β)-region is represented by equiaxed recrystallized and deformed grains, the average grain size in the root part being larger than that in the airfoil and amounting to 0.9 and 0.7 μm, respectively. This is related to the fact that in the more massive root part, cooling after forging is slower than in the airfoil, which promotes more intensive recrystallization processes.

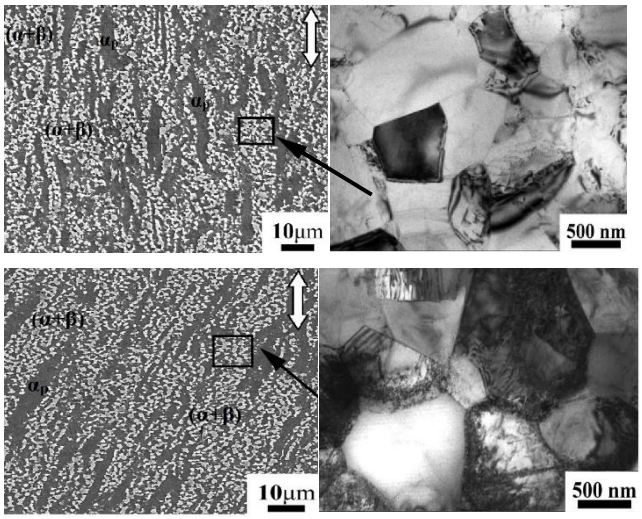


Figure 2. *Microstructure of the experimental forging: (a,b) the airfoil of the forging; (c,d) the root of the forging; (a,c) SEM; (b,d) TEM. The arrow indicates the draw direction.*

The mechanical properties of the specimens are listed in table 1. In the longitudinal direction of the experimental forging's airfoil (figure 1) strength declines to 1100 MPa as compared to the condition after RS (UTS = 1290 MPa), but at the same time ductility increases visibly, in particular, the uniform and percentage

elongations grow to 7 and 15%, respectively (table 1). Such a decline in strength in conditioned by a decrease in dislocation density, the propagation of recrystallization and an increase in the sizes of small globular grains of the α- and β-phases (from 0.3 to 0.7 μm) (figure 2). The mechanical properties of the specimens in the longitudinal and cross directions of the airfoil zone have some differences. In particular, the ultimate tensile strength (UTS) in the cross section of the airfoil is slightly higher (1118 MPa), while the ductility, percentage and uniform elongations are lower. This is apparently conditioned by the presence of the inherited after RS metallographic and crystallographic texture in the forged workpiece.

Therefore, the results of this investigation demonstrates a possibility in principle of preserving a UFG structure during the shape-forming of an item by isothermal forging, and correspondingly, of preserving enhanced mechanical properties.

Table 1. *Mechanical properties of the Ti alloy VT8M-1 in different conditions.*

Condition	UTS, MPa	YS, MPa	Elong., %
As-received	1056±10	967±5	13±0.5
RS	1290±5	1195±10	9±1
Airfoil zone longitudinal direction	1100±30	947±25	15±1
Airfoil zone cross direction	1118±10	1048±20	10±0.6

4. Conclusions

1. The UFG structure with ultrafine α- and β-grains ~ 0.3 μm was obtained by the rotary swaging. This type of UFG structure leads to an increase in the ultimate tensile strength to UTS = 1290 MPa and some decline in elongation to δ=9%, as compared to the initial condition.

2. It is shown that as a result of isothermal forging at a temperature of 780°C, the high strength workpiece retains the ultrafine grain size which increased to 0.7 μm due to the processes of recovery and recrystallization.

Acknowledgements

The reported study was funded by RFBR, project number 20-38-70105\20.

References

1 Leyens C and Peters M 2003 Titanium and Titanium Alloys. Fundamentals and Applications (Weinheim: Wiley-VCH Verlag GmbH) p 513

2 Ermachenko A G, Lutfullin R Ya and Mulyukov R R 2011 Rev. Adv. Mater. Sci. 29 (1) 68

3 Salischev G A, Imaev R M, Imaev V M and Gabdulin N K 1993 Mater. Sci. Forum. 113 (115) 613

Structure-phase transformations in LiF powders and crystals irradiated in nuclear reactor and 60Co gamma-source

Elvira Ibragimova[1,2], Shovkat Buzrikov[1], Nurmuhamad Iskandarov[2], Malika Mussaeva[1] and Khamdam Nazarov[2]
Institute of nuclear physics Academy of sciences[1]; Center for advanced technologies, Ministry of innovation development[2], Tashkent, Uzbekistan; E-mail: ibragimova@inp.uz , buzrikov@inp.uz , mussaeva@inp.uz , nur1979@mail.ru , nazarov1111@mail.ru

Abstract: XRD, SEM-EDS and FTIR were used for studying stable products of nuclear reactions of "branching decay" in LiF exposed to intensive 1.17 and 1.33 MeV ^{60}Co γ-radiation to dose 10^9 R and mixed neutron+γ-fluxes of WWR to fluencies 10^{17}-10^{18} cm^{-2}: $^{19}F_9 + \gamma \rightarrow {}^{11}B_5 + {}^{7}Li_3 + {}^{1}H_1$ or $\rightarrow {}^{16}O_8 + {}^{3}T_1$ and $^{19}F_9 + {}^{1}n_0 \rightarrow {}^{20}Ne_{10}$ or $\rightarrow 2^{10}B_5$ in addition to the known ^{6}Li$(n,\alpha)^3$T. The main part of impact radiation is absorbed in micron subsurface layer, so the following radiation induced structure-phase transformations are highly inhomogeneous: hillocks of LiF-B_2O_3 and LiBH, LiO_2 nanofilm and LiH nanocones are detected on LiF surface. It explains impossibility of annealing LiF-detectors.
KEYWORDS*: LiF, NEUTRON IRRADIATION; GAMMA IRRADIATION; NUCLEAR FISSION; NANOPARTICLES, PHASE TRANSFORMATION, XRD, FTIR, SEM-EDS*

1. Introduction

LiF crystals have been used as scintillators, tunable laser elements on color centers, and thermal-luminescence dosimeters of nuclear radiation; but aggregation of anion vacancies and assembling of Li colloids at long-term radiolysis restrict to the low dose limit of multiple use the detectors in the irradiation – thermal anneal repetition mode [1-4]. Tritium fuel was suggested to be bred in-reactor by Li transmutation reactions ^{6}Li(n,α)T and ^{7}Li(n,n'α)T [2]. Various oxide ceramics such as Li_2O, Li_2SiO_3, Li_2ZrO_3, $LiAlO_2$ were considered for using in the breeding blanket. But microstructural damages (swelling, sintering, microcracking, decomposition) can affect tritium diffusion mechanism.

The earliest (1950-1970 years) articles described inhomogeneous defect production at irradiations of thin and thick LiF crystals with fluencies of thermal neutrons within 10^{16}–10^{18} cm^{-2} inducing reactions ^{6}Li$(n,\alpha)^3$T and ^{7}Li$(n,\alpha)^2$He, incompatible changes of X-ray lattice parameters and macroscopic density (measured from dilatation due to vacancy generation) for neutron irradiated thin LiF crystals. The authors estimated the interstitial atom concentration as 8600 per one Li fission [5]. Seitz suggested that 2.1 MeV α-particles emitted from Li produce atom displacements, derived relation (1900/2) $\sigma\phi t \sim 7\times10^{-20}\phi t$ (integral fluency in cm^{-2}) and calculated the number of Li replaced by tritium (initial energy 2.7 MeV upon emission) in the distance of 10 μm, so at the fluency 5×10^{19} cm^{-1} each atom is displaced once [6]. But experiments did not confirm it. Microscopic examination of the high dose slow (<0.1 MeV) neutron irradiated samples after 24 hours annealing at 700 C has found bubbles (*helium* gas pockets) six microns in size and *square* cross-section [7]. Residual low angle scattering is believed to be due to ^{3}H and ^{4}He formed by fission of Li that can't be annealed. Later Li colloids and vacancy aggregates were found after higher fluencies by means of XRD and SEM [1,2,8-12].

Besides irradiations in atom reactors, Frenkel pairs and defect aggregates in anion sublattice were induced with soft X-rays and even with vacuum UV-photons and detected by optical spectroscopy [2,3,9,12]. Therefore alternative non-elastic mechanism for Frenkel defect production became dominant, namely non-radiative decay of the localized excitons [13,14]. Compton scattering of 662 keV γ-radiation in lithium fluoride was used for studying the electron momentum distribution [15]. Our earlier experimental XRD analysis showed that after ^{60}Co γ-irradiations at 500-1000 R/s 300 K to doses 10^8 - 10^9 R (such irradiations simulate the effect of γ-component of the reactor with the maximum of energy distribution at 1.3 MeV) there appeared weak reflections of Li nanocrystals of 8 nm size in LiF:Cu scintillator crystals, and the reflection of LiOH nanophase of 28 nm in LiF:OH laser mode lock [16,17]. Non-linear laser effects in LiF:OH were attributed to aggregated anion vacancy centers generated by ^{60}Co γ-flux [18].

When the energy of γ-quanta is >1.022 MeV, then interacting with a nucleus field such a quant is transformed into an electron-positron pair, in this way a localized long living positronium was found in KCl/NaCl [19]. One should mention that at low Z nuclei photo-effect and Compton scattering of γ-quanta are not effective, therefore in the case of ^{60}Co the absorption of γ-quanta 1.17 and 1.33 MeV by light nuclei may be dominant followed by generation of electron-positron pairs and beta-decays. No paper was found related to possible nuclear reactions with F, however odd nucleus $^{19}F_9$ (following the magic $^{16}O_8$) needs much less energy for releasing a nucleon: such as peripheral reaction ^{19}F$(p,\alpha)^{16}$O or ^{19}F$(n,\gamma)2(^{10}B_5)$. Nobody studied LiF where both Li and F would transmute under neutron and γ-irradiation and how it could affect the breeding and phase composition [2]. So γ-flux accompanying the neutron flux could contribute to the lattice defect production, but nobody took into account it, except lattice heating effect [19].

2. Experiments

The aim of this research was to elucidate separately the contribution from nuclear reaction to radiolysis and structure-phase transformations in undoped LiF under influence of the fission neutron (mean square energy 1.3 MeV) fluencies within 10^{17}-10^{18} cm^{-2} (when the maximal lattice expanding occurred [5-8]) and γ-quanta (0.1-6 MeV) fluencies 10^{18}-10^{19} cm^{-2} in the center of WWR-SM reactor core and the maximal ^{60}Co γ-ray (1.17 and 1.33 MeV) dose of 10^9 R (simulating the γ-component of reactor irradiation to 10^{18} cm^{-2}). The set of complementary surface sensitive techniques including X-ray diffraction (XRD), local element analysis by *K*-lines (EDS), scanning electron microscopy (SEM), infrared reflection and transmission (FTIR) spectroscopy. In order to determine local defect structures a crystal or powder sample is rotating [20]. It should be mentioned that EDS cannot detect Li, He and H [21], however it can determine B, C, O and F loss from ratios.

3. Results

We first compared the element and phase composition of external and internal cut surfaces of crystals and powders prior and after irradiations and found significant inhomogeneity at the scale of mm, which is close to the calculated by Seitz penetration depth ~2-3 mm in LiF [6].

3.1 XRD and EDS

All measurements were done 1 year after irradiation so as to get stable isotopes and relaxed equilibrium phase mixture.

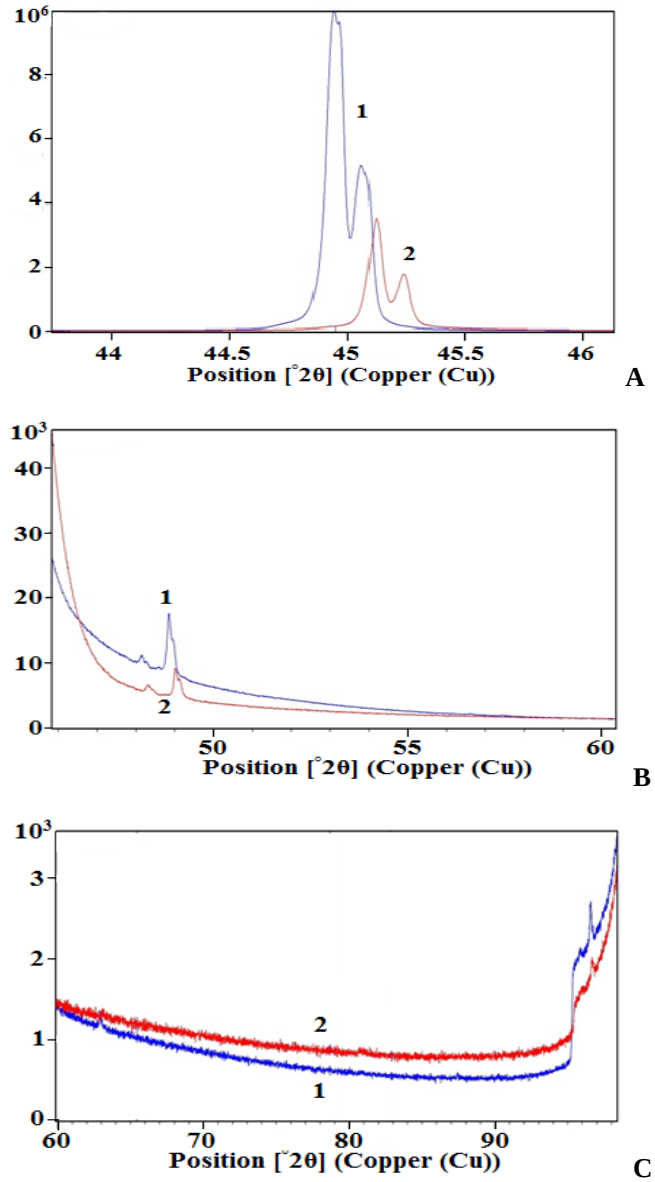


Figure 1. XRD spectra (with Ni filter) of cleaved surface of LiF crystal: 1- pristine and 2- γ-irradiated to10^9 R: A) (200) reflection of cubic LiF and $Li_2F_2B_6O_9$; B) orthorhombic Li_2O_2 and LiO_2; C) both weak peaks belong cubic LiH aside strong (400) peak of the dominant phase. Y-axis are given in counts with the factors 10^3 and 10^6 respectively.

Table 1 Phase and element composition of LiF powder and crystal after gamma and neutron irradiations respectively. Irradiation induced phases are marked with red bold font.

XRD data			EDS data from 4 spots	
Phase composition	Content, vol %		Element	Mass %
Non –irradiated crystal and powder sample (reference)				
LiF	97		C+B	2.49 – 3.74
LiH	3		O	0.52 – 0.81
Li_2O_2	<1		F	95.45 – 96.84
Powder sample γ-irradiated to 10^9 R				
$Li_2F_2B_6O_9$	**84**		C+B	24.89 – 46.42
LiH	4		O	2.71 – 22.70
LiO_2	**12**		F	35.61 – 72.39
Neutron fluency 10^{17} cm^{-2} in the WWR core 2 hours				
LiF	62		C+B	2.80 – 15.21
Li/LiH	**3**/24		O	0.72 – 5.62
$LiBH_{2-4}$	**3**		F	79.17 – 96.48
B/B_2O_3	**1/4**			
$Li_2F_2B_6O_9$	**3**			
10^{18} cm^{-2} 20 hours				
LiF	53		C+B	22.07 – 25.46
LiB_3O_5	**35**		O	2.53 – 3.13
$LiBH_4$	**8**		F	71.54 – 74.81
$LiB_{0.88}$	**4**			

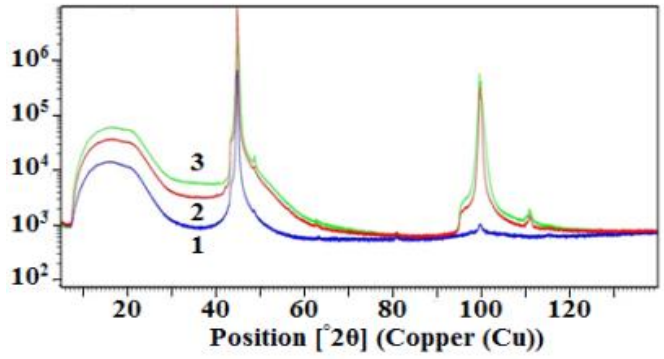


Figure 2. XRD spectra of LiF crystals after irradiation in WWR to the fast neutron fluencies: 1) 10^{17}, 2) 10^{18} cm^{-2}, 3) 0.7×10^{18} cm^{-2} irradiated at the maximal flux in WWR core.

Scale factors ~0.002 for cubic LiH and Li oxides (Table 1) are much less than 0.297 for LiF, which means that these phases are thin and situated on the surface of LiF, as will be shown below by SEM. After the γ-irradiation the phases formed on the surface are thin (scale factors 0.054 for $Li_2F_2B_6O_9$ and 0.011 for LiO_2), however the matrix LiF cannot be detected underneath. The dominant cubic phase turned out the best fitting the reflection profiles and angular positions. Unlike early XRD experiments, when only Li phase was found and the shifted (h00) reflections after heavy irradiation were attributed to the defect induced lattice deformation [5,7,9] and abnormal scattering by tiny inclusions [8,10,11], modern profile High Score code and data base PDF2 (2013) allowing precise lattice and phase analysis found 3%Li and 1%B phases. Decay of F and generation of B and O is confirmed by the local EDS, listed in right columns. Unfortunately SSD (129 eV) cannot resolve *K*-lines of B (0.1834 keV) and C (0.277 keV). Since XRD did not find carbonate, C+B line can be ascribed to B. Table 1 demonstrates highly inhomogeneous element distribution over the irradiated surface as compared to the pristine, and also increase of B content due to the related decrease of F. It shows that in 2 hours of irradiation in the reactor core ~30% F disappears even more effectively (due to fission initiated both by neutrons and 6 MeV γ-quanta from Oxygen in water moderator) than Li considered in [1-12]. More 18 hours make obviously less effect in fission of F (only 10%). Significant decrease in (400) reflection of LiF after the neutron fluency 10^{17} cm^{-2} (may be because of small sample or density decrease due to generation of gaseous product – He from Li [11] and Ne from F). Maximal small angle scattering and broadening occurs after higher fluencies.

Neutron irradiation to the fluency of 10^{17} cm^{-2} caused the growth of Li/LiH, generation of B/B_2O_3, $LiBH_{2-4}$ and $(LiF)_2(B_2O_3)_3$. A higher fluency of 10^{18} cm^{-2} increases significantly the level of incoherent scattering at lattice defects and anisotropic broadening of the basic reflections.

3.2 FTIR

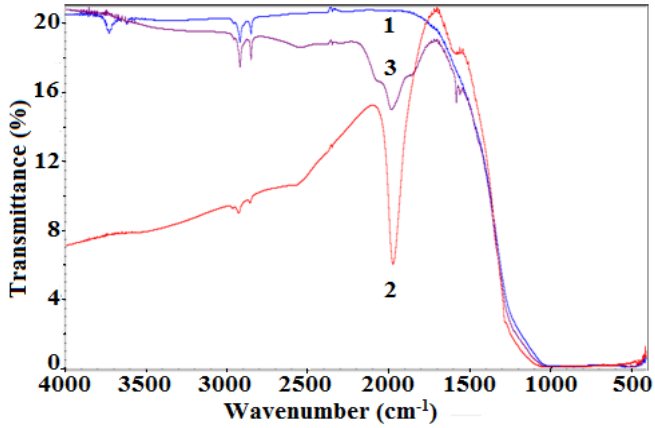
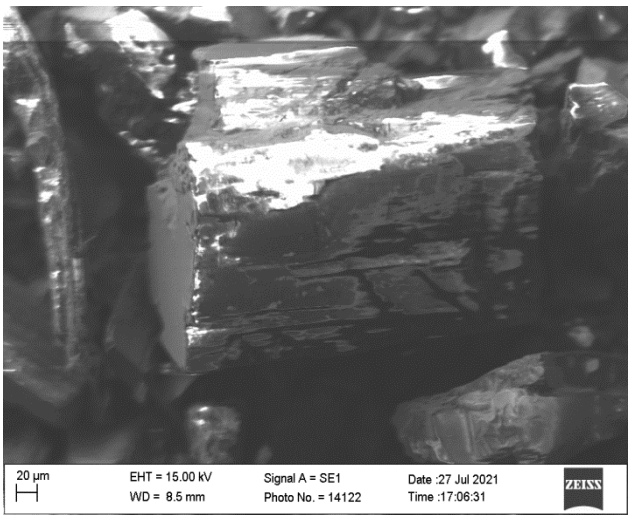


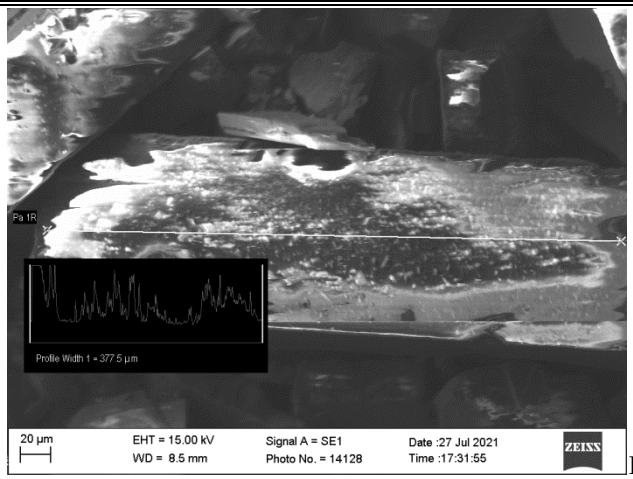
Figure 3 FTIR transmission (%) spectra of LiF crystals: 1- non-irradiated, 2- ^{60}Co γ-irradiated to the dose 10^9 R, 3- irradiated in WWR to the fast neutron fluency 10^{17} cm^{-2}.

Non-irradiated sample has weak bands at 3750 - 3650 cm^{-1} relate to monomer OH groups, and weak doublet at 2800-2900 cm^{-1} attributes to LiH, and basic Li-F stretching band at 1000 cm^{-1} and weak Li-F deformation band at 1300 cm^{-1}. After exposure to γ-10^9 R very broad scattering region is caused by LiO_2 nanophase, and intensive band at 2000 cm^{-1} and also band at 1500 cm^{-1} appeared due to B_2O_3 and B-H bonds. Since the neutron fluency 10^{17} cm^{-2} made much less damage than 10^9 R gamma, the intensities of the induced bands are small too. These FTIR data are in a good agreement with XRD and EDS listed in Table 1.

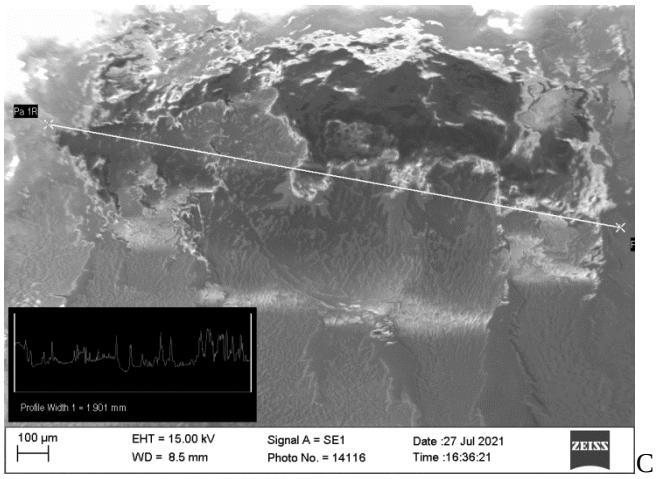
3.3 SEM and local EDS



A



B



C

Figure 4. SEM image of LiF powder: A) pristine, B) ^{60}Co γ-irradiated to 10^9 R, C) fast neutron 10^{18} cm^{-2}. Inset: profile.

Because of charging LiF dielectric surface under focused electron beam figures 4 show submilli-fragments of powder and micrometer profiles. Thin phases on the irradiated surface look as multiple hillocks (B) and walls of open bubbles and stripes (C). These gamma and neutron doses seem to produce comparable damages. The image (C) resembles earlier photo of LiF crystal surface coated with carbon after 10^9 R [23]. Stripes of LiH and LiBH phases are electric conductors and decrease charging by e-beam.

4. Discussion

4.1 Gamma-induced nuclear reactions in LiF

Unlike β-particles and electromagnetic radiation of ~ keV producing high ionization during linear energy loss, ~1 MeV γ-quanta can transfer the total energy in one interaction with one nucleus, especially a light one with A<40, called "branching decay" or "stripping decay" [19]. To explain our results, the following reactions are suggested: $^{19}F_9 + \gamma \rightarrow {}^{11}B_5 + 2{}^3T_1 + 2{}^1H_1$ or $\rightarrow {}^{11}B_5 + {}^7Li_3 + {}^1H_1$ or $\rightarrow {}^{16}O_8 + {}^3T_1$ or $\rightarrow {}^{18}O_8 + {}^1H_1$ and $^{16}O_8 + \gamma \rightarrow {}^{10}B_5 + {}^6Li_3$ and $^{18}O_8 + \gamma \rightarrow {}^{11}B_5 + {}^7Li_3$. Indeed, the nuclear fission barrier $E \sim A/Z^2$ for F(0.23) and O(0.25) is much less than that of Li(0.77) and B(0.44).

Gamma-radiation in the WWR reactor with various energies > 0.1 MeV includes electron-positron annihilation

band at 0.511 MeV, line 2.2 MeV characteristics of $p+n \rightarrow D+\gamma$, lines 4.4 MeV of ^{12}C (graphite) and 6.1 MeV of ^{16}O (water), and lines of other nuclei recoils from excited states [19]. So it seems incorrect to consider reactions only with thermal neutrons [2,5-9] and ignore γ-component from 0.5 up to 6 MeV capable of nuclei disintegration, and not only electron subsystem [3,13,14]. Quantum theory was developed for chemical reactions of LiF molecules with H atoms and HF molecules with Li atoms excited in the presence of electromagnetic fields at low temperatures [22]. The authors showed that electric fields may enhance the probability of chemical reactions and modify reactive scattering resonances by coupling ***the rotational states*** of the reactants. The nuclear reactions excite rotation of nuclei too.

4.2 Neutron-induced nuclear reactions in LiF

Besides well known reactions of Li with thermal neutrons mentioned in the introduction [2,5-9], we also considered reactions of slow neutron with F: $^{19}F_9 + {}^1n_0 \rightarrow {}^{20}Ne_{10} \rightarrow 2^{10}B_5$ resulting in Ne bubbles or B solids. In very rigid LiF ionic lattice α-particles after Li decay can be captured by a neighbor: $^{19}F_9 + {}^4\alpha_2 \rightarrow {}^{23}Na_{11}$ and make an anti-site replacement defect. But due to charge instability it will move to the nearest vacant Li site and make impurity cation Na^+.

Radiation induced H, B and O nuclei being in excited state effectively form chemical compounds with Li in thin subsurface layer of neutron penetration. Boron having much larger neutron capture cross-section than Li finally decays into Li and H. Such nuclear reactions provide reasonable explanation for the measured phase composition.

5. Conclusion

Gamma-quanta 1.17 and 1.33 MeV from ^{60}Co source are absorbed by Li and F nuclei and produce stable isotopes H, He, B and O by the "branching" reactions. Then being in the excited state they easily make chemical compound and form crystal phases, observed on the irradiated surface of LiF.

At the neutron+gamma exposure in the WWR reactor core both neutrons and accompanied gamma-quanta are absorbed by Li and F nuclei and produce stable isotopes B and O by the reactions of neutron or alpha capture.

Besides Frenkel pairs, Li colloids and vacancy aggregates, usually called radiolysis, these nuclear reactions generate tiny phases under and on the surface, therefore the expired LiF detectors cannot be thermally annealed in principle.

Set of XRD, SEM-EDS and FTIR can be used for studying stable products of nuclear reaction without emission other than radioisotope $^3T_1$ and the related structure-phase transformations in light element compounds exposed to > 1 MeV ^{60}Co γ-radiation and mixed neutron+γ-fluxes.

This work was supported at the INP by Science Research Program under President Decree No 4526 of 21.11.2019 and at CAT on the applied research project PS-2017-0919163 supported by Ministry of innovation development of Republics Uzbekistan.

6. References

[1] Hobbs L.W., A.E. Hudges, G. Chassagne. Direct observation of alkali metal colloids in alkali halide crystals. *Nature* **252** (1974) 383.

[2] Johnson R.A., A.N. Orlov, Physics of Radiation Effects in Crystals. Elsevier Science Publ B.V., 1986. p. 387.

[3] Baldacchini G., Colored LiF: an optical material for all seasons, *J. of Luminescence* **100** (2002) 333.

[4] Salah N. Nanocrystalline materials for the dosimetry of heavy charged particles: A review. *Radiation Physics and Chemistry* **80** (2011) 1-10

[5] Binder D. and W.J. Sturm. Equivalence of X-ray lattice parameters and density changes in neutron irradiated LiF. *Physical Review* **96** (1954) 1519-1522

[6] Seitz F. and J.S. Koehler. *Solis State Physics* **2** (1956) 90, 443

[7] Smallman R.E. and B.T.M. Willis. An X-ray study of neutron irradiated lithium fluoride. *Philosophical Magazine* **2** (1957) 1018-1026. DOI:10.1080/14786435708238208

[8] Lambert M., Ch. Mazieres, A. Guinier. Precipitation de lithium dans les monocristaux de fluorure de lithium irradies aux neutrons thermiques. *J. Phys. Chem. Solids* **18** (1961) 129-138.

[9] Knutson S.D., H.O. Hooper, P.J. Bray. A nuclear magnetic resonance study of decomposition in neutron-irradiated LiF *J. Physics Chemistry of Solids*, **27** (1966) 147.

[10] Kolontsova E.V., I.V. Telegina, V.L. Zefirova. Effect of irradiation conditions on defect structure of LiF single crystals. In: Radiation effects in solids. Kiev, Naukova dumka, 1977. p. 102-110.

[11] Dubinko V.I., A.A. Turkin, D.I. Vainstein, H.W. den Hartog. Theory of the late stage of radiolysis of alkali halides. *J. Nuclear Materials* **277** (2000) 184-198.

[12] Izerrouken M., N. Souami, L. Guerbous, S. Djaroum, M. Kadouma, A.Sari, A. Meftah. Li colloids formation study induced by reactor neutrons in LiF single crystals. *Nuclear Instruments and Methods* **B 266** (2008) 2745.

[13] Stoneham A. M. Theory of radiation defects *Nuclear Instruments and Methods in Physics Res.* **A 91** (1994) 1-11.

[14] Siscafus K.E., Kotomin E.A. Radiation Effects in Solids. Amsterdam: Uberuaga Springer B. P., 2007. Ch. 7.

[15] Vijayakumar R., Shivaramu, Ramamurthu, N., Ford M.J. Compton scattering study of electron momentum distribution in lithium fluoride using 662 keV gamma-radiation. *Physica B: Condensed matter*, **403** (2008) 4309-4313

[16] Mussaeva M.A., E.M. Ibragimova, M.U. Kalanov, M.I. Muminov. Formation of nanodefects in LiF crystals under gamma irradiation. *Physics of the Solid State* **48** (2006) 2295.

[17] Ibragimova E.M., M.A. Mussaeva, M.U. Kalanov, N.M. Mukhamedshina, V.N. Sandalov. Lithium nanoparticles in lithium fluorite crystals. *J. Phys. Conf. Ser.* **391** (2012) 012172.

[18] Bryukvina L.I. and E.F. Martynovich. *Physics of the Solid State*. **54** (2012) 2056.

[19] Friedlander G., J.W. Kennedy,G.S. Macias, J.M. Miller. Nuclear and radiochemistry. New York: J.Willey&Sons 1981

[20] Holder C.F. and R.E. Schaak. Tutorial on Powder X-ray Diffraction for Characterizing Nanoscale Materials. *ACS Nano* **13** (2019) 7359-7365

[21] Allen L.J., A.J. D'Alfonso, B. Freitag, D.O. Klenov. Chemical mapping at atomic resolution using energy-dispersive X-ray spectroscopy. *MRS Bulletin* **37** (2012) 47-52

[22] Tscherbul T.V., R.V. Krems. Quantum theory of chemical reactions in the presence of electromagnetic fields. *J. Chemical Physics* **129**(3) (2008) 034112

[23] Mussaeva M.A., E.M. Ibragimova. Electron microscopy and elemental composition of the near-surface layer of electron-irradiated LiF crystals. *Technical Physics Letters* **45** (2019) 155–158. https://doi.org/10.1134/S1063785019020299.

Morphological and structural features of electrospark coatings

Auchynnikau Yauheni[1]., Pinchuk Tatiana[2], Eisymont Yauhenia.[1], Mihailov Valentin[3], Kazak Natalia[3], Bahanovich Ludmila[4]
Yanka Kupala State University of Grodno[1]-Grodno, Republic of Belarus
State Scientific Institution "O.V. Roman Powder Metallurgy Institute"[2] – Minsk, Republic of Belarus
Institute of Applied Physics[3] – Chisinau, Moldova
State Scientific Institution "Physical-Technical Institute of the National Academy of Sciences of Belarus"[4] - Minsk, Republic of Belarus

E-mail: ovchin@grsu.by, iscentr@tut.by, eisymont@grsu.by, valentin.mihailov@gmail.com, bakhanovich2@yandex.by

Abstract: *The morphology of the coatings has a significant effect on the tribological characteristics of the contacting bodies. Depending on the relief of the surface layers of the coatings, the resistance of the modified substrates to corrosion is determined. It is known that the processes of friction and corrosion have a decisive influence on the performance of products. To reduce the influence of these processes, various protective coatings are used, including those formed by the method of electrospark alloying. The aim of this work was to study the morphology and structure of electrospark coatings formed by layer-by-layer electrospark alloying. In the course of the studies carried out, it was found that these coatings are morphologically heterogeneous, with a large number of cracks and splats.*

KEYWORDS: MORPHOLOGY, COATING, ELECTRIC DISCHARGE, ALLOYING, PLASMA

1. Introduction.

The fundamental role in the failure of products and parts of mechanisms and machines is the processes of friction and corrosion. In this regard, it is necessary to use multifunctional protective coatings formed by various technological processes. The determining factor when using coatings is the economic aspect. So, at present, most of the protective coatings are formed using imported technologies and materials. When creating coatings, complex technologies are used that are expensive. In this regard, it becomes necessary to create new technological methods for the formation of multifunctional coatings based on domestic raw materials [1] - [3].

In the agro-industrial complex, multicomponent systems of organic and inorganic origin are widely used to restore and form the surfaces of friction parts and protect them from corrosion and mechanical wear. As a result of a synergistic combination of metallic and non-metallic components, high deformation-strength, tribotechnical, physicochemical characteristics are achieved [1] - [3].

One of the promising methods is electrospark alloying (ESA). The essence of the method lies in the process of deposition of molten material on the surface to be treated with an electric spark discharge. In some cases, melting of the material is achieved by the formation of plasma in a spark discharge, which significantly changes the properties of the layers being formed. The process of melting and deposition of the master alloy occurs in an air and inert gas environment [4]. The formation of coatings by the method of electrospark alloying is carried out on installations such as UR-121, IM101, SE-5.01, IMPULS-1A, SPARK-1000, etc. Low internal stress coatings can be obtained by preheating the part with a gas burner flame. The molten particles are deposited on a preliminarily prepared substrate, form strong adhesion or chemisorption bonds, and cool to form a hard coating [4]. Supercooling (106 Kc^{-1}) or high particle cooling rates can lead to the formation of unusual amorphous and metastable phases, which are unusual for materials obtained by other technologies. The method of electrospark alloying is characterized by a number of advantages: the possibility of applying coatings to products made of practically any conductive material.

The aim of this work is to study the morphology and structure of electrospark coatings formed by the layer-by-layer method.

2. Materials and Procedures

Nanocomposite electrospark coatings based on nitrides, carbides, silicides of titanium and aluminum were applied by the method of electrospark alloying on Impuls-1A installations. Various grades of metals were used as substrates: BT 6; 40X13 The coatings were applied both to the metal as delivered, and the steel substrate was hardened to HRC 53-60 and polished to a purity not lower than grade 10. The studied objects were multicomponent coatings obtained from metal compounds, the compositions of which are shown in table 1. The coatings were formed using the Impuls-1A installation (manufactured by the Institute of Applied Physics of the Academy of Sciences of Moldova). Modes of obtaining coatings are shown in Table 1. The morphology of coatings was investigated on a scanning electron microscope "MIRA3 TESCAN". The microscope is equipped with detectors for secondary electrons SE and backscattered electrons BSE, which allow the study of samples in two modes. The study of the elemental composition was carried out using an INCA 350 micro X-ray spectrum analyzer (Oxford Instruments, England). Detectable elements from B to U. Minimum element detection limit - 0.5%

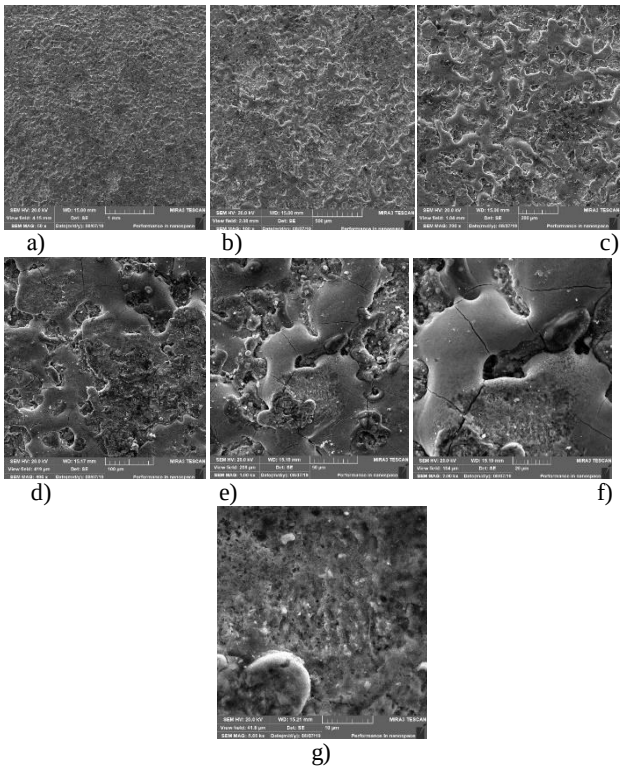
Table 1 - Modes of formation of coatings, compositions of electrodes

Sample	Coating formation parameters		
	coating formation mode, J	substrate	electrode composition
№1	0,9	40X13	Ti+Al+C
№2	0,9	40X13	Ti+Si+C
№3	0,9	40X13	Ti+Al+N
№4	0,9	40X13	Ti+C
№5	0,9	40X13	W+C

3. Results and discussion.

During the formation of nanocomposite coatings by the methods of electrospark alloying, surface layers with a developed morphology are formed (Figures 1 - 4). According to the data of scanning electron microscopy, ESA coatings formed on a 40X13 steel substrate have a developed morphology. Thus, with an increase in resolution, the formation of the morphology of coatings of the "pebbled skin" type is observed. Those. coalescence of molten cathode droplets occurs during deposition on the substrate surface with the formation of voids. The geometrical dimensions of these formations depend on the cathode material and the modes of coating formation. TiC coatings produce a smoother texture, which is reflected in its corrosion characteristics. A sufficient number of cracks are observed in the structure of the coatings, which affect the strength and adhesion characteristics of the coatings.

The obtained materials are in good agreement with the literature data [5]. The coatings formed by ESA on chromium-nickel stainless steel with titanium at a current of 2.0 - 2.5 A were distinguished by the presence of particles characteristic of electrospark coatings - plaits, which are melted particles of the transferred material (Figure 5, a). Similar plaits were observed in TiAlN coatings formed on a titanium substrate (Figure 3, b).

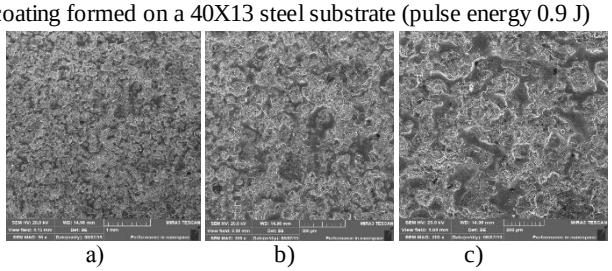


a) b) c)

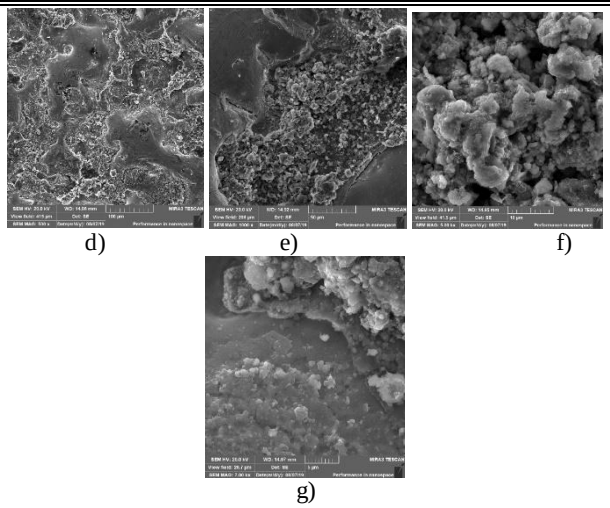
d) e) f)

g)

Figure 1 - Morphology of the TiAlC electrospark coating formed on a 40X13 steel substrate (pulse energy 0.9 J)



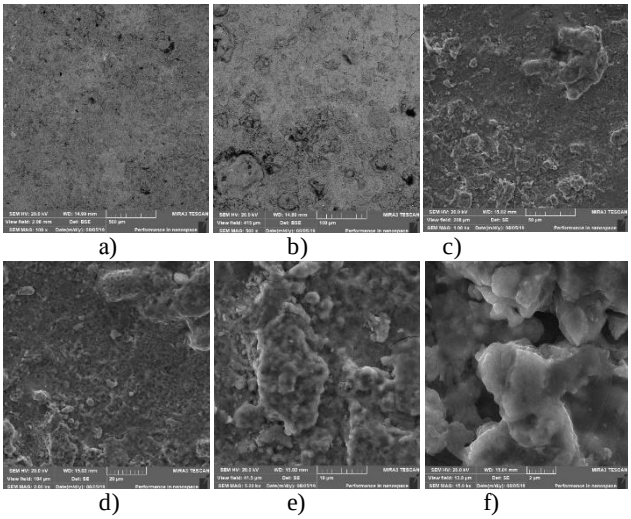
a) b) c)



d) e) f)

g)

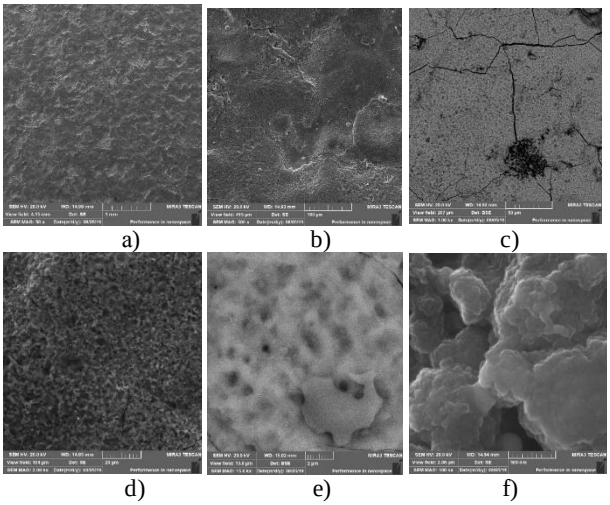
Рисунок 12 – Morphology of TiSiC electrospark coating formed on a 40X13 steel substrate (pulse energy 0.9 J)



a) b) c)

d) e) f)

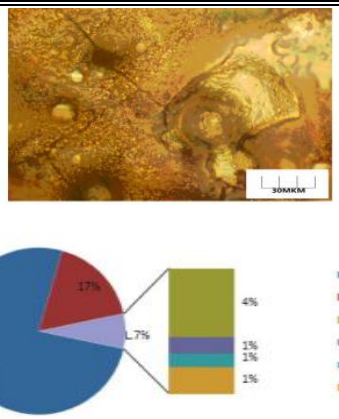
Figure 3 – Morphology of TiAlN electrospark coating formed on BT6 substrate (pulse energy 0.9 J)



a) b) c)

d) e) f)

Figure 4 – Morphology of an electrospark TiC coating formed on a VT6 substrate (pulse energy 0.9 J)

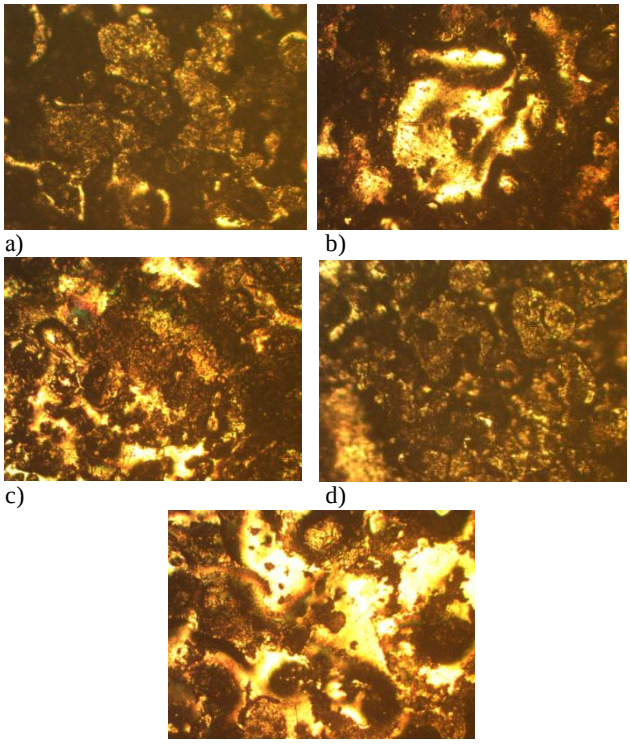


a - surface image; b - distribution of the average linear size of structural elements

Figure 5 - Morphology of the coating formed by ESA at a current of 0.8 - 1.0 A [5]

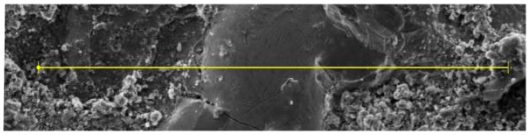
Scanning electron microscopy data are in good agreement with the results of optical studies (Figure 6).

A chemical analysis of the surface layers of electrospark coatings showed the formation of structures in the form of drops, in which iron is the main component. Thus, during electrospark alloying, intensive mixing of the electrode and substrate material occurs, and the formation of surface structures with an increased iron content is possible (Figure 7).

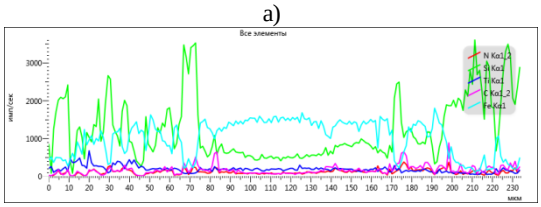


a – TiAlC, b – TiSiC, c – TiAlN, d – TiC, e – WC

Figure 5 - Morphology of electrospark coatings formed on a steel substrate 40X13



a)



b)

Figure 6 - Distribution of chemical elements in the surface layers of the electrospark TiSiC coating formed on the VT6 substrate (pulse energy 0.9 J)

4. Conclusions

Thus, the investigated electrospark coatings are characterized by a developed morphology. A sufficiently large number of pores is observed in the coatings obtained by this method, which affects the physicomechanical characteristics of these research objects. The most common defects are cracks and braids.

References.

1. Tribotechnical characteristics of composite coatings based on zirconium carbonitride subjected to cryagenic treatment/ Y. Auchynnikau [and others.] // Machines. Technologies. Materials.- 2018.- № 4.- C.118-121.
2. Hybrid methods for handening of superhard vacuum coatings/ Y. Auchynnikau [and other] // Machines. Technologies. Materials.- 2019.- № 10.- C.451-453
3. Y.V. Auchynnikau, V.A. Gubanov, Nanocompositive fluorine-containing coatings, Fundamental problems of radio electronic instrument making, 16 (2), 2016, p. 54–57.
4. Kazak n., Mikhailov v., Ivashcu s., Shkurpelo a., Auchynnikau E. Tribotechnical characteristics of nanostructured coatings formed by eil method / Proceedings of 10th international scientific conference balttrib 2019, 2019, p.114-118
5. Filimonova A.V., Mezentsov S.A. The structure of coatings formed by electrospark alloying of steel 12X18H10 with titanium // Modern scientific knowledge: theory, methodology, practice: Collection of scientific papers based on the materials of the VIII International Scientific and Practical Conference. / Smolensk, (June 10, 2019) - Smolensk, 2019 .- p. 107 - 112.

Application of sprayed bronze powders of the brsn10ph1 and BRSN5ZN5PB5 grades for applying protective coatings by gas-flame spraying

Aliaksandr Ilyushchanka [1, 2], Ruslan Kusin [3], Yugeniy Manoila [4], Iryna Charniak [2], Aliaksei Kusin [2], Syargei Yurchanka [2], Artsiom Staselka [2], Anhelina Maiseyeva [2], Iryna Kurylchyk [3], Vladimir Semenov [5]
State research and production powder metallurgy association[1] – Minsk, Republic of Belarus
State Scientific Institution "O.V. Roman Powder Metallurgy Institute" [2] – Minsk, Republic of Belarus
Belarusian state agriculture technical university [3] – Minsk, Republic of Belarus
Self-Supporting Enterprise "Institute of Welding and Protective Coating" [4] – Minsk, Republic of Belarus
Ufa State Aviation Technical University [5] – Ufa, Russia
E-mail: alexil@mail.belpak.by, 19081877@mail.ru, irinacharniak@tut.by, 2312444@mail.ru, semenov-vi@rambler.ru

Abstract: *Information on a small-size installation for production of atomized powders of copper-based alloys is presented. The process of obtaining pulverized powders of BrSn10Ph1 and BrSn5Zn5Pb5 grades by induction melting and melt gas atomization, intended for hardening of new and restoration of worn surfaces by gas-flame coating, as well as protection against corrosion of parts is studied. The quality of the coatings obtained using the manufactured powders has been confirmed.*
KEYWORDS*: EQUIPMENT FOR POWDER PRODUCTION, SPRAYED BRONZE BRSN10PH1 AND BRSN5ZN5PB5 POWDERS, INVESTIGATIONS, PROPERTIES, GAS-FLAME SPRAYING*

1. Introduction

The simplicity and cost-efficiency of the application of coatings by gas-flame spraying for strengthening new and restoring worn-out surfaces, as well as for the protection of parts of various functional purposes against corrosion, make this method attractive [1, 2]. Available equipment for gas-flame spraying of powders, consisting of a sprayer and a gas control panel, as well as powder materials for applying coatings are required to implement this method [3]. As materials, sprayed powders of bronze powders based on copper are widely used.

The purpose of the work is to obtain sprayed powders of tin-phosphorous bronze BrSn10Ph1 and lead bronze BrSn5Zn5Pb5 for applying protective coatings.

2. Результаты эксперимента и их обсуждение

To solve this problem, the small-sized equipment was developed to study the processes of powder production based on copper (Fig. 1).

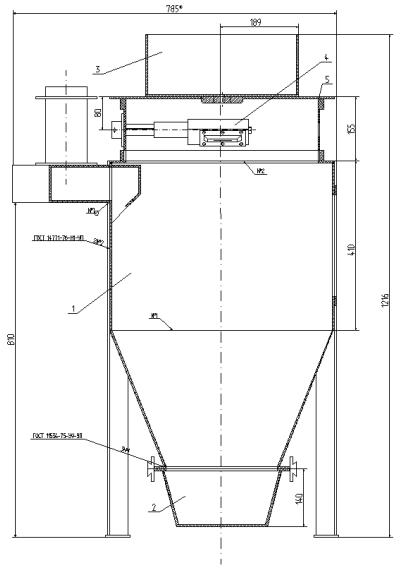


Fig. 1*. Equipment for production of metal powders by spraying a metal melt by gas flow:*
1 – body; 2 – bottom plate; 3 – metal reservoir;
4 – nozzle; 5 – cover

The production of experimental samples of sprayed bronze powders of BrSn10Ph1 and BrSn5Zn5Pb5 grades included the following basic operations [4]: weighing the initial components, loading the components into an induction melting furnace and heating, spraying a jet of the melt, removing the powder from the equipment and drying, sieving powder (Fig. 2).



Fig. 2. *Spraying process of copper-based powders by gas flow atomization of metal melt*

As a rule, powders of various fractions are obtained by air spraying. By varying the air pressure during spraying and the angle of inclination of the nozzles, it is possible to regulate the output of a given powder fraction to a certain extent. Studies have shown that the output of powder is 95%. Depending on the modes of spraying, the output of the sprayed powder of large fractions is 5-35% when using slot nozzles and fractions with a particle size less than 0.16 mm – up to 5-10%. Figure 3 shows the particle size distribution diagrams of tin-phosphorous bronze powders produced by means of this equipment.

When using these powders for the production of porous products, such a distribution is acceptable and almost all of the powder without remelting can be used at manufacturing site. However, for applying gas-thermal and gas-dynamic coatings onto worn-out surfaces or to protect them against corrosion, powders with particle sizes less than 100 μm are required. This leads to the remelting of powder with large particles and, accordingly, to significant additional energy costs. In this regard, a specialized spray unit was developed with a set of removable nozzles [5].

It is known that the main factors determining the powder dispersion are the viscosity, the surface tension of the melt and the gas flow energy [6]. The viscosity of the melt is regulated by the chemical composition of the alloy and the temperature of the melt, and the surface tension of the melt is regulated by the diameter of

the flowing jet of the melt. To obtain powders with particles less than 100 μm, it was decided to increase the relative gas flow rate. To solve this problem, a nozzle design was developed for spraying a metal melt by air based on a de Laval nozzle. A set of removable nozzles makes it possible to change the angle of gas attack in a wide range and change the area of their cross section (Fig. 4) [5].

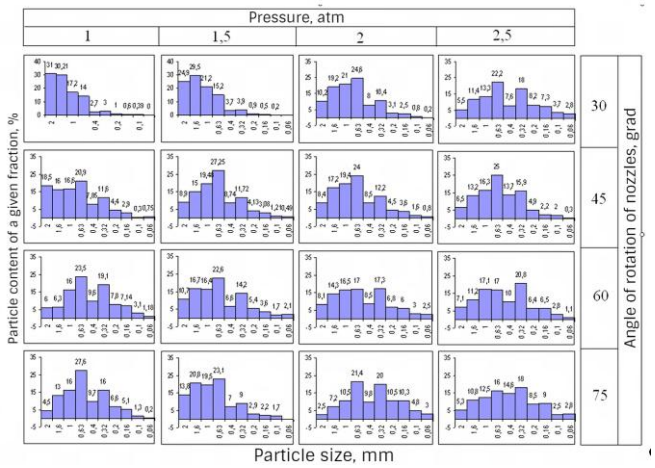


Fig. 3. Particle size distribution diagrams of the powder

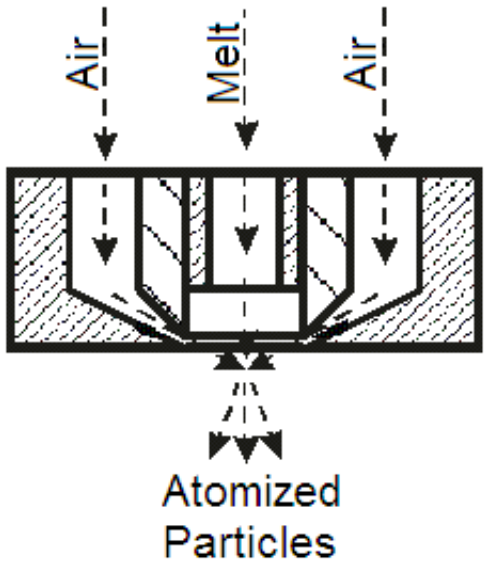


Fig. 4. *The nozzle for spraying based on the Laval nozzle*

The output of applicable powder with fractions less than 100 μm was more than 80% when using a specialized spraying unit to produce sprayed spherical powders of tin-phosphorous bronze BrSn10Ph1. Figure 5 shows the appearance of the particles of the manufactured BrSn10Ph1 brand bronze powder. The properties of tin-phosphorous bronze powders are shown in Table 1.

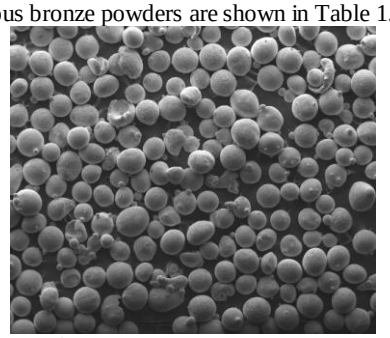


Fig. 5. *Powders of tin-phosphorous bronze with a particle size of less than 100 μm*

Table 1. *Properties of tin-phosphorous bronze BrSn10Ph1 powders.*

Fraction, μm	Bulk density, γ, g/cm^3	Flow rate τ, sec	Tap density, g/cm^3	Spherical shape factor
(-0.063+0.01)	5,30	9.80	5.70	0.95
(-0.1+0.063)	5,23	11.60	5.65	0,95
(-0.16+0.1)	5,10	12.10	5.52	0,95
(-0.2+0.16)	4,95	13.00	5.47	0,95
(-0.315+0.2)	4,90	17.10	5.40	0,95
(-0.4+0.315)	4,85	19.90	5.30	0,95
(-0.63+0.4)	4,80	28.00	5.25	0,95
(-1.0+0.63)	4,75	30.00	5,18	0,95

Similar results were obtained when studying the process of obtaining powders of the BrSn5Zn5Pb5, only taking into account the technological features when melting the melt in an induction furnace, namely the influence of carbon monoxide of one of the components – zinc [7-9]. The appearance of the bronze powder particles of the BrSn5Zn5Pb5 grade is shown in Figure 6, the properties are shown in Table 2.

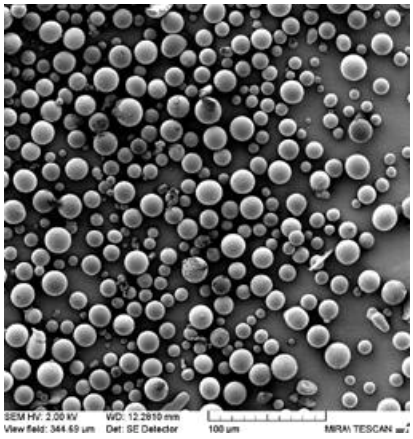


Fig. 6. *Appearance of the obtained bronze powder particles of the BrSn5Zn5Pb5 grade*

Table 2. *Values of bulk density, density after shaking, the ratio of density after shaking to the bulk density of BrSn5Zn5Pb5 powder.*

Fraction, μm	Bulk density, γ, g/cm^3	Flow rate τ, sec	Tap density, g/cm^3	The ratio of the density after shaking to the bulk density
(- 0,063 + 0,01)	5,26	9.80	5,60	1,065
(- 0,1 + 0,063)	5,16	11.60	5,55	1,076
(- 0,16 + 0,01)	5,11	12.10	5,51	1,078
(- 0,2 + 0,16)	5,06	13.00	5,49	1,085
(- 0,315 + 0,2)	4,90	17.10	5,42	1,106
(- 0,4 + 0,315)	4,85	19.90	5,38	1,109
(- 0,63 + 0,4)	4,80	28.00	5,36	1,117
(- 1,0 +0,63)	4,78	30.00	5,35	1,119

It should be noted that this equipment can produce powders of alloys based on copper and aluminum of other compositions used, for example, for restoring and strengthening the surfaces of crank-shaft necks, “fits” for rolling bearings, internal surfaces of slider bearings (provided that the coating length does not exceed the diameter of the hole), surfaces of transmission shafts, camshaft necks, wheel hubs, etc. [10].

The produced tin-phosphorus bronze and aluminum powders with a particle size of less than 100 μm were sprayed onto steel substrates by high-speed gas-flame spraying on TENA-Ppm equipment (Figure 7) using MAF (methyl-acetylene-allene fraction) as combustible synthetic gas.



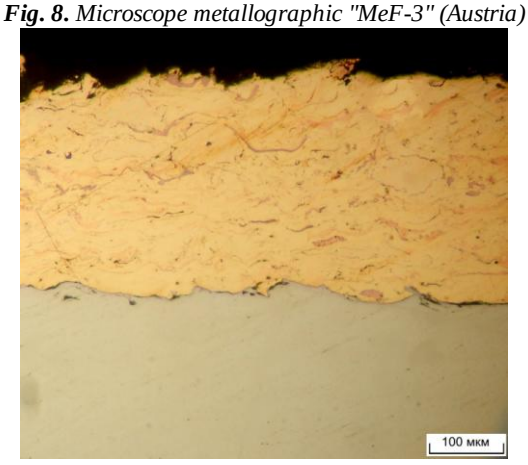
Fig. 7. *Chamber of semi-automatic spraying TENA-KPAN-1300 with the equipment of gas-flame spraying TENA-Ppm*

To study the strength of the joint of the coating with the surface of the steel plate, slots were made and metallographic studies were carried out on a metallographic high - temperature microscope "MeF-3" (Austria) (Figure 8). Studies of the structures have shown a strong formation of the coating and the absence of cracks and detachment. The structure of experimental coatings made of bronze powders BrSn10Ph1 and BrSn5Zn5Pb5 are shown in Figure 9.

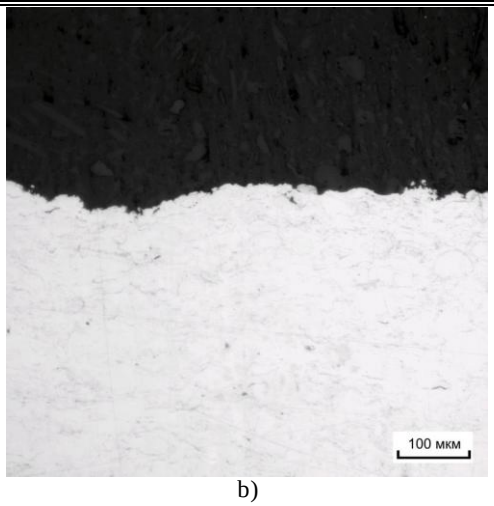


Analysis of the microstructures of the obtained coatings makes it possible to conclude that the quality of the sprayed coatings is high: the total porosity in the sprayed layer is much lower than the allowable 2%.

Fig. 8. *Microscope metallographic "MeF-3" (Austria)*



a)



b)

Fig. 9. *Microstructures of coatings applied to steel plates by gas-flame spraying from bronze powders of tin-phosphorous bronze BrSn10Ph1 ×100 (a) and lead BrSn5Zn5Pb5 (b)*

3. Conclusion

Information about the equipment design for producing sprayed powders based on copper and aluminum, intended for applying coatings by gas-flame spraying when strengthening new and restoring worn-out surfaces, as well as for the protection of parts for various functional purposes against corrosion, including crankshafts, transmission shafts, wheel hubs, camshafts, etc. is presented.

It is shown that the equipment provides powders with a high level of properties and powder output of fine fractions. The possibility of using the obtained powders of tin-phosphorous bronze BrSn10Ph1 and lead BrSn5Zn5Pb5 for applying high-quality sprayed coatings has been experimentally confirmed.

4. References

1. Ilyushchanka, A.Ph. Heavy Engineering, (2000), No. 2. P. 12-17 (A.Ph. Ilyushchanka, Y.D. Manoila, T.N. Tolstyak) (in Russian).
2. Vityaz, P.A. Theory and practice of coating application, Minsk: Belaruskaya navuka, (1998). P. 158 (P.A. Vityaz et al.) (in Russian).
3. Kaptsevich, V.M. Filtering materials: promising areas of application in the agro-industrial complex and modern production technologies, Minsk: BSATU, (2006). P.189 (V.M. Kaptsevich, L.S. Boginsky, R.A. Kusin, O.P. Reut) (in Russian).
4. Silaev, A.Ph. Dispersion of liquid metals and alloys, Moscow: Metallurgy, (1983). P. 144 (A.Ph. Silaev, B.D. Fishman) (in Russian).
5. Ilyushchanka, A. Small-sized equipment and nozzle with a Laval design for producing sprayed powders based on copper, Powder metallurgy, Minsk, Belaruskaya Nauka, Vol. 34, 2011, pp. 37-42. (A. Ilyushchanka, R. Kusin, I. Charniak, A. Kusin, D. Zhegzdrin, Y. Manoila, V. Kaptsevich).
6. Urvachev, V. Jewelry and art casting according to consumable models of copper alloys, Chelyabinsk, Metallurgy, 1991, p. 166 (V. Urvachev, V. Kocheikov, N. Gorina) (in Russian).
7. Brockmeier, K. Induction melting furnaces, trans. From German. Edited by Shevtsov M.E., Stolov M.Ya., Moscow, Energiya, 1972, p. 304 (K. Brockmeier) (in Russian).
8. Chursin V. Melting of copper alloys, Physical-chemical and technical foundations, Moscow, Metallurgy, 1982, p. 152 (V. Chursin) (in Russian).
9. Ilyushchanka, A. Production of powders of copper alloy (copper 85, tin 5, lead 5, zinc 5) by spraying a melt with a gas flow / *Machines. Technologies. Materals*. Sofia, Bulgaria, 2020, Year XIV. ISSUE 7. P. 280-282 (A. Ilyushchanka, I. Charniak, A. Kusin, D. Yarahovich, R. Kusin, M. Dechko, V. Marhanava).
10. Ilyushchanka, A.Ph. Advanced materials in agricultural engineering: monograph, Minsk: BSATU, (2009), P. 256 (A.Ph. Ilyushchanka, V.M. Kaptsevich, R.A. Kusin, A.M. Yarkovich, A.R. Kusin) (in Russian).

Knowledge for material science. Part II

Stefan Bushev
Bulgarian Academy of Science, Sofia, Bulgaria
Institute of Metal Science, Equipment and Technologies
with Hydro- and Aerodynamics Centre „Acad. Angel Balevski "
67 Shipchenski Prohod Blvd., 1574 Sofia, Bulgaria[2]
stbushev@abv.bg

Abstract: This article discusses the modern knowledge necessary for materials science. Modern scientific knowledge covers on the basis of the greatest scientific results; complete scientific knowledge: mathematics; mathematical physics; quantum mechanics (not relativistic and relativistic); quantum physics; quantum chemistry. Theory and modern tools for testing and monitoring with increasing resolution. High technologies. A research – type methodology has been obtained, but this methodology is also focused on interactions with business. Business research is not fundamental, but it can be very lengthy.

Keywords: MODERN SCIENCE KNOWLEDG, SCIENCE METHODOLOGY, BISINESS, HIGH THECNOLOGY

1. Introduction

In the first part, we looked at thermodynamics and solid state physics from the point of view of the theory of materials science and the engineering approach. There are great difficulties in using the modern knowledge necessary for materials science. Note we continue the numbering of figures and equations from the first part. The need to use heuristics is presented. The heuristic approach is an important tool to apply when creating powerful opportunities.

The aim of this work is to present the need and the great complexity of working with of modern scientific knowledge.

2. Quantum mechanics and Quantum physics

Quantum mechanics describe behavior of moving micro-particles [14]. To study their movement, new principles are introduced, corresponding to their complex duality [14].

The main task of physics by quantum physics seeks the answer to the questions [17]: What are the elementary components of matter? What are the fundamental controlling forces their behavior?

3.1 Quantum mechanics

According [14] to modern quantum theory of light, these two diametrically opposed points of view can be combined. The corresponding wave characteristics [14] (for example frequency and wavelength) are compared to corpuscular (energy, momentum). Corpuscular-wave dualism of microparticles is not possible to simultaneously determine their coordinates and pulses (velocities) in a given direction.

I

Corpuscular – wave dualism of electromagnetic wave (photon) comparability wavelenght and impulse

$$E_\gamma = hf = \frac{h\omega}{2\pi} = \hbar\omega, p_\gamma = \frac{h}{\lambda} = \frac{hk}{2\pi} = \hbar k, \hbar = \frac{h}{2\pi}. \quad (5, E_\gamma, p_\gamma)$$

$$\lambda = \frac{h}{p} = \frac{h}{mv}, \quad (5, \lambda)$$

II

$$(5, Heisenberg)\quad \begin{vmatrix}\Delta x\Delta p_x \geq h & \Delta x\Delta v_x \geq h/m\\ \Delta y\Delta p_y \geq h & \Delta y\Delta v_y \geq h/m\\ \Delta z\Delta p_z \geq h & \Delta z\Delta v_z \geq h/m\end{vmatrix}$$

$$\Delta E\Delta t \geq h. (5, 1, Heisenberg)$$

III

$$\Psi(x,y,z,t) = |\Psi|e^{i\Phi}. \quad (5, \Psi, |\Psi|, \Phi)$$

$$|\Psi|^2 = \frac{dW}{dV}; dW = |\Psi|^2 dV, (5, |\Psi|^2, dW)$$

$$W_\infty = \int_{V_\infty} dW = \int_{V_\infty} |\Psi|^2 dV = 1. (5, W_\infty)$$

IV

$$(5, \Psi \text{ must satisfy condition})\quad \Psi: \begin{cases} \text{limited;} \\ \text{continuous and unambiguous;} \\ \text{obey the principle of superposition:} \end{cases}$$

V

$$\Psi = \sum_{i=1}^{n} c_i \Psi_i, \quad \left(5, dualism, \begin{matrix}\text{Combines quantum}\\ \text{and wave properties}\end{matrix}\right)$$

where c_i are coefficients (complex numbers); n are the number of states with waves functions $\Psi_1, \ldots \Psi_n$.

VI

$$(5, Schrödinger)\quad -\frac{\hbar^2}{2m}\Delta\Psi(x,y,z,t) + U(x,y,z,t)\Psi(x,y,z,t) = i\hbar\frac{\partial\Psi(x,y,z,t)}{\partial t},$$

where m is particle mass; U is particle potential energy in the field in which it moves; $i = \sqrt{-1}$; *the Laplas operator* $\Delta\Psi = \left(\frac{\partial^2\Psi}{\partial x^2} + \frac{\partial^2\Psi}{\partial y^2} + \frac{\partial^2\Psi}{\partial z^2}\right)$. *At* $U = U(x,y,z)$, $\Psi(x,y,z,t) = \Psi(x,y,z)\varphi(t)$ *and we replace in eq.* $(5, Schrödinger)$ *and we will obtain:*

$$-\frac{\hbar^2}{2m}\Delta(\Psi\varphi) + U\Psi\varphi = i\hbar\frac{\partial(\Psi\varphi)}{\partial t}; \quad -\varphi\frac{\hbar^2}{2m}\Delta\Psi + U\Psi\varphi = i\hbar\frac{\partial\varphi}{\partial t} \quad |:\Psi\varphi$$

$$\Rightarrow -\frac{1}{\Psi}\frac{\hbar^2}{2m}\Delta\Psi + U = E = \frac{1}{\varphi}i\hbar\frac{\partial\varphi}{\partial t},$$

where E is the particle full energy and we obtain the:

$$(5, Schrödinger\ stationar\ equation)$$

$$\Delta\Psi(x,y,z) + \frac{2m}{\hbar^2}[E - U(x,y,z)]\Psi(x,y,z) = 0.$$

VII

Free microparticle motion (FMM)

$$\frac{\partial^2\Psi}{\partial x^2} + \frac{2m}{\hbar^2}E\Psi = 0. \quad \left(5, \begin{matrix}Schrödinger\\ FMM\end{matrix}\right)$$

$$E = T = \frac{mv^2}{2} = \frac{p^2}{2m} = \frac{\hbar^2k^2}{2m}. \quad (5, E, FMM)$$

$$\frac{\partial^2\Psi}{\partial x^2} + k^2\Psi = 0. \quad \left(5, 1, \begin{matrix}Schrödinger\\ FMM\end{matrix}\right)$$

$$\Psi(x) = Ae^{ikx} + Be^{-ikx} \text{ or } \Psi_1(x) = Ae^{ikx} \text{ and } \Psi_2(x) = Be^{-ikx}. \quad \left(5, 2, \begin{matrix}Schrödinger\\ solution\\ FMM\end{matrix}\right)$$

A, B are constants; $i = \sqrt{-1}$; Ψ_1, *and* Ψ_2 *are two monochromatic waves and* Ψ_2 *are two monochromatic waves* $\left(\lambda = \frac{h}{mv} = const\right)$ *propagating of two opposite directions: 1st in OX with amplitude A and 2nd in* $-OX$ *with amplitude B.*

Passage of a microparticle through a potential barrier

$$\frac{\partial^2\Psi}{\partial x^2} + \frac{2m}{\hbar^2}E\Psi = 0, \quad (5, \text{for areas 1 and 3 at } U = 0)$$

$$\frac{\partial^2\Psi}{\partial x^2} + \frac{2m}{\hbar^2}E\Psi - \frac{2m}{\hbar^2}U_0\Psi = 0. \quad (5, \text{for area 2, where } U = U_0)$$

$$\Psi_{1,3}(x) = A_{1,3}e^{ik_1x} + B_{1,3}e^{-ik_1x};$$

$$\Psi_2(x) = A_2e^{ik_2x} + B_2e^{-ik_2x}. \quad (5, \text{gemeral solution: 1, 2 and 3})$$

$A_1, A_2, A_3, B_1, B_2, B_3$ *are constants;* $k_1 = \sqrt{2mE}/h$ *and* $k_2 = \sqrt{2m(E-U_0)}/\hbar$ *is imaginary number at* $E < U_0$. $k_2 = ik$, *where* $k = \sqrt{2m(E-U_0)}/\hbar$ *and for* $\Psi_2(x)$ *we obtain:*

$$\Psi_2(x) = A_2e^{-k_2x} + B_2e^{k_2x}. \quad (5, solutions\ 2nd\ area)$$

$A_1e^{ik_1x}$ *is falling wavw,* $B_1e^{-ik_1x}$ *is reflected wave; probabilities of particle motion: to the barrier* $|A_1|^2$ *and in the opposite direction* $|B_1|^2$. *The reflection coefficient of the barrier is R:*

$$R = \frac{|B_1|^2}{|A_1|^2}. \quad (5, R)$$

$\Rightarrow$ *Similarly* $A_2e^{-k_2x}$ *and* $B_2e^{k_2x}$ *dsescribe the two waves and corresponding probabilities are* $|A_2|^2$ *and* $|B_2|^2$. *For area 3* $B_3 = 0$ *and* $\Psi_3(x) = A_3e^{ik_1x}$ *and the transperancy coefficient of the barrier is the ratio of the probabilites:*

$$D = \frac{|A_3|^2}{|A_1|^2}. \quad (5, R)$$

For a rectangular barrier with width l, the transparency coefficient D is determined by the formula:

$$D = D_0 e^{-2kl} = D_0 e^{-\frac{2l}{\hbar}\sqrt{2m(U_0-E)}}, \quad (5,1,D)$$

where $k = \sqrt{2m(U_0 - E)}/\hbar$ ***at*** $E < U_0$; $D_0 \sim 1$; ***m is the mass of the particle.***

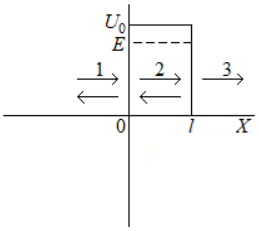


Fig.9 *Free micro-particle motion through potential barrier: width l and height U_0 barrier energy; space is divided into three areas: 1 ($x < 0$), 2 ($x \in (0, l)$) and 3 ($x > l$); direction of movement along the 0X axis; E is the total energy of a particle; the particle $E > U_0$ passes over the barrier, at $E < U_0$ it cannot pass through the barrier and reaches a height allowed by E. According to quantum mechanics, there is a probability $\neq 0$ ($E < U_0$) that the particle will cross the barrier and the motion is described by eq. (5, Schrödinger stationary equation).*

The transparency coefficient D depends on the values m l and (U_0-E), and with their increase the probability of the particle passing through the barrier decreases. Hence the conclusion that for macrobodies quantum mechanics passes into the classical one: particles with large mass do not pass through the barrier. ***Tunnel effect:*** *passage of a microparticle through a potential barrier.* A number of phenomena in physics are described by the tunnel effect: cold emission of electrons (separation of electrons from the surface of a metal under the action of an external electric field); α - decay of radioactive nuclei; contact phenomena at the boundary between solids and others. The tunnel effect is a specific phenomenon and is observed only at a very small width of the barrier (of the order of the dimensions of the atoms 10^{-10} m).

Experiments led to the creation of quantum mechanics: **1.** linear emission spectra of gases heated to high temperatures. The wavelengths are arranged in a series of lines; as J. Ballmer in 1885 year proposes an empirical formula for the visible region of the hydrogen spectrum $\lambda_n^{-1} = R(2^{-2} - m^{-2})$, at m>2, λ_n is the wavelength for the corresponding spectral line (*Ballmer series*) at n=3, 4, 5 and so on; $R=1{,}097.10^7 m^{-1}$ is *the Rydberg constant*. Ballmer's formula was summarized in 1888 by J. Rydberg $\lambda_n^{-1} = R(n^{-2} - m^{-2})$. Notation of the spectral lines of hydrogen in the visible part of: n = 3 is with H_α red; n=4 is with H_β blue; n=5 is with H_γ (H_δ) violets. In 1906 T. Lyman discovered such series for n = 1 in the ultraviolet region and in 1908 F. Pashen discovered for n = 3 in the infrared region for hydrogen**; 2.** The phenomenon of radioactivity was discovered by A. Becquerel in 1896: uranium salts emit highly penetrating invisible rays from charged α- and β-particles. In 1900, P. Viyar discovered another type of γ-beam without an electric charge**; 3.** In 1897 year J. Thomson discovered the electron and proved that cathode rays are a stream of negatively charged particles very close in characteristics to β-rays**; 4.** The listed experimental discoveries led to the conclusion that atoms are not indivisible particles and scientists began to study the structure of the atom through the discovery of new particles. Thus, in 1911, after studying the scattering of particles from various substances, E. Rutherford discovered that all the positive charge and almost all the mass was concentrated in the *nucleus* of the atom with dimensions of the order of 10^{-15} m; Rutherford proposed *the nuclear model of the atom*: a positively charged nucleus with an electron shell - electrons moving in closed orbits. The charge of the nucleus is equal in size to the total charge of all electrons. This model explains well: the scattering of α-particles by matter; allows to determine the charge q of the nucleus; it is shown that q = Ze, where Z is the ordinal number of the element in Mendeleev's periodic table multiplied by the elementary electric charge. *Contradictions in Rutherford's model: According to classical electrodynamics, any electric charge moving rapidly must emit electromagnetic waves. Each electron in the electric field of the nucleus has a potential energy $U \sim e^2/r$, where r is the radius of the corresponding orbit of the electron. The electron, moving around the nucleus, will continuously emit electromagnetic waves, which will gradually reduce the energy and its corresponding orbit until it falls on the nucleus, i.e. the atom will not be a stable system; the period and frequency of electromagnetic radiation is also constantly changing, i.e. the emission spectrum must be continuous. While the experiment shows that atoms emit a linear (discrete) spectrum*. The shortcomings of Rutherford's model were eliminated in a new quantum model of the atom proposed by N. Bohr in 1913 on the basis of its three postulates: **1.** ***an atom can exist only in certain steady states, each of which is characterized by a certain value of total energy.*** The stationary states correspond to certain stationary circular orbits in which the electrons move. ***When moving in these orbits, electrons do not emit electromagnetic waves***; **2.** ***When an atom passes from one steady state to another, a photon is emitted or absorbed.*** An atom emits a photon if an electron transitions from a higher energy state E_m to a lower energy state E_n or absorbs a photon by making a transition from a lower energy state to a higher energy state. ***The energy of the absorbed or emitted photon is equal to the difference in the energies of the two states:*** $\boldsymbol{E_\gamma = hf = |E_m - E_n|}$; **3.** the momentum of the electron in stationary orbits can have only discrete (quantized) values: $\boldsymbol{L_n = mv_n r_n = n\hbar;\ n = 1, 2, 3\ \ldots}$. Bohr's 1st postulate defines ***the stability of atoms***. Bohr's 2nd postulate is related to the observed ***discrete spectra of an atom and in accordance with Planck's quantum hypothesis for thermal radiation***. Bohr's 3rd postulate is not related to anything observed at that moment; it is a continuation of the idea of ***quantizing quantities in the microworld***. Its meaning was clarified 10 years later when de Broglie hypothesized ***the wave nature of microparticles***; It turns out that the 3rd postulate imposes ***the condition that an integer number of de Broglie waves be applied to each possible circular orbit of the electron***: $\boldsymbol{2\pi r_n = n\lambda_n;\ 2\pi r_n = n(h/mv_n) \Rightarrow mv_n r_n = n\hbar}$. In other words, the electron can only be found in such orbits whose length is a multiple of the de Broglie wavelength for the electron at the corresponding velocity.

To explain the structure of multi-electron atoms, two principles have been formulated: 1. **indistinguishability of elementary particles** - *all particles of one type are the same and cannot be distinguished from each other* (*for example, to be marked in some way*). Example with two identical balls as **A** is colored with paint and **B** is not; and say that the ball **A** is located to the left of **B**. When exchanging places, *another state of the system is obtained*! In the case of elementary particles, this is not possible - when exchanging the places of the particles, the same happens due to the principle of *indistinguishability*. The probabilities for realization of both conditions must be the same, i.e. the square of the modulus of the wave functions is obtained the same. This is possible if the two wave functions differ in sign: $\Psi(1, 2) = \pm\Psi(2, 1)$. The wave function of a system of identical particles is called symmetric if the sign is "+", i.e. $\Psi(1, 2) = \Psi(2, 1)$ and antisymmetric if $\Psi(1, 2) = -\Psi(2, 1)$. There is a significant difference in the behavior of systems of identical particles with symmetric and antisymmetric wave function. In a symmetric wave function, all particles in the system can be in the same quantum state (*this may be the state with the lowest energy*). Definition: **Bosons are identical particles in the same quantum state with the lowest energy and their spin is an integer multiple of ħ: 0, ħ, 2ħ, 3ħ, …**; 2. **Pauli exclusion principle for fermions**: in a system of identical fermions there cannot be two particles that are in the same quantum state. Definition: **Fermions are particles described by an antisymmetric wave function and have a half-spin ħ/2, 3ħ/2, 5ħ/2 ….** The electrons are fermions with spin *ħ/2* (therefore the spin quantum number can take values ±1/2), all electrons in the electron shell of a given atom must be in different quantum states. The behavior of bosons and fermions in quantum mechanics is described by quantum statistics - ***Bose-Einstein statistics*** for ***bosons***

$$\textbf{\textit{Bose}} - \textbf{\textit{Einstein distribution}}\ \mathfrak{l}^{b} = \frac{1}{e^{(E^{p}-\mu)/k_B T} - 1},$$

Fermi-Dirac statistics for ***fermions***

$$\textbf{\textit{Fermi}} - \textbf{\textit{Dirac distribution}}\ \mathfrak{l}^{f} = \frac{1}{e^{(E^{p}-\mu)/k_B T} + 1},$$

and ***Maxwell-Boltzmann statistic*** for ***ideal gas***

$$\textbf{\textit{Maxwell}} - \textbf{\textit{Boltzmann distribution}}\ \mathfrak{l}^{d} = \frac{1}{e^{(E^{p}-\mu)/k_B T}}\ \mathfrak{l}^{d} \ll 1,$$

Fundamentals of quantum mechanics

Principles of quantum mechanics

Quantum mechanics [14] described the micro-particles moving and the interaction between them. At microparticle experiments, macroscopic instruments interact with the microparticles and inevitably change their properties. Quantum mechanics allows to predict the experimental results [14]: *the possible values* of the measured physical quantity; *the probabilities* with which these values are obtained. *The* ***state*** of a system is defined *differently in each field of physics*. Generalization: *The state of the system must allow all measurable properties of this system to be found*. In classical mechanics, a system of bodies is characterized by a specific number of constants (mass, charges, inertial moments, etc.) and a specific number of variables (coordinates, velocities, moments of momentum, impulse moment, energies, etc.). The state a pure mechanical system of N materials points can describe of **(one multidimensional vector)** (*multiD vector*) with 6N components: 3N coordinates and 3N impulses. Knowing this vector, we can calculate the system: impulse moment; potential and kinetic energy [14]:

$$\vec{L} = \sum_{k=1}^{N} m_k \vec{r_k} \times \vec{v_k},\ V = \sum_{k=1}^{N} V(\vec{r_k}),\ T = \sum_{k=1}^{N} \frac{1}{2} m_k \vec{v_k}^2,\ \textbf{(4, L, V, and T)}$$

Where m_k, r_k, v_k are mass, coordinate and velocity of the point k. Newton's laws are:

(***Newton's laws***)
Newton's laws in one dimension 1D **[20]:**
Newton's first law: *If there is no forces acting on an object, it stays in the same state of motion.*
Newton's second law: *The sum of all the forces acting on an object determines the rate at which its momentum changes,* $F_{total} = dp/dt$.
Newton's third law: *Forces occur in opposite pairs. If object A interacts with object B, then A's force on B and B's force on A are related by* $F_{AB} = -F_{BA}$.

Properties for the state of a classical system [14]: (**Newton's laws**) with (*multiD vector*) and forces F acting on the particles, then we can find (*multiD vector*) at any subsequent moment, i.e. ***the classical state of the system*** is equivalent to (*multiD vector*), which allows the following three properties [14]:

-if we know the vector of the state of the system at a given moment t_0*, to find all quantities describing the system;*

-if we know the vector of the state of the system at a given moment t0, to find the vector of the state at any subsequent moment of time;

-we can find the state vector with a finite number of measurements.

The construction of the state of the system in classical mechanics cannot be used in quantum mechanics due to Heisenberg's uncertainty principle i.e. we do not know both the coordinates and the momentum of the particles [14]. In quantum mechanics *the three properties of the state remain in force*. Particle state in quantum mechanics is given with *wave function* $|\Psi(\vec{r},t)\rangle$, of the coordinate $\vec{r}$ and of the time [14].

Zero principle of quantum mechanics (state) [14]: *At any given time, the state of a quantum mechanical system is described by an abstract complex vector in Hilbert space, called a* ***state vector*** *or* ***wave function*** $|\Psi(q, t)\rangle$. The generalized coordinate of the system is q, i.e. set of all coordinates of the system. It is assumed that Ψ it is normalized:

$$\langle\Psi(q,t)|\Psi(q,t)\rangle = \int \Psi(q,t)^{*}\Psi(q,t)dt = 1. \qquad (5,1,\Psi)$$

It is necessary to emphasize [14] that the quantum-mechanical information for a system is not as complete as in classical mechanics *i*.e. to emphasize the meaning of the zero principle is the scheme

$$\underbrace{\left[\begin{array}{c}\textit{Classical - mechanical information}\\ \textit{in the one (multi D vector) contain}\\ \textit{all the necess information}\end{array}\right]}_{\textit{i.e. the change}}\ \begin{array}{c}\textit{Heisenberg's}\\ \textit{uncertainty}\\ \textit{principle}\end{array}\ \left[\begin{array}{c}\textit{Quantum mechanical information}\\ \textit{in the wave function } \psi \textit{ contain}\\ \textit{maximum possible information}\end{array}\right].$$

In classical physics with real functions of one or more variables represent the physical quantities for example: the coordinate $\vec{r}(t)$ as a function of time; the velocity $\vec{v}(t)$ is the first derivative in time t $\vec{v}(t) = \dot{\vec{r}}(t)$; the potential energy $V(\vec{r})$ is a function of the distance r; the kinetic energy T is a function of the mass m and the velocity $\vec{v}$: $T = (1/2)mv(\vec{r})^2 = \vec{p}^2/(2m)$, where $\vec{p} = m\vec{v}$ is the momentum of the particle, and the momentum is the vector product of the coordinate $\vec{r}$ and the momentum of the particle $\vec{p}$: $\vec{L} = \vec{p} \times \vec{r}$. Replacing functions in classical mechanics with operators in quantum mechanics based on:

First principle of quantum mechanics (operators) [14]: *A linear Hermitian operator A is compared to each physical quantity*$\hat{A}$*. The functional dependences in classical physics remain unchanged, and the physical quantities are replaced by the corresponding operators.*

Operators of fundamentals physicals quantities [14]. The main operators in quantum mechanics are:

- $\hat{r} = r;$ $\quad (5,\hat{r});\left(\begin{array}{c}\textit{operator}\\ \textit{coordinate}\end{array}\right)$
- $\hat{p} = -i\hbar\hat{\nabla} = -i\hbar\dfrac{\partial}{\partial r} = -i\hbar grad_r;$ $\quad (5,\hat{p});\left(\begin{array}{c}\textit{operator}\\ \textit{impuls}\end{array}\right)$
- $\hat{L} = \hat{r} \times \hat{p};$ $\quad (5,\hat{L});\left(\begin{array}{c}\textit{operator}\\ \textit{moment of}\\ \textit{impulse}\end{array}\right)$

- $\hat{T} = \dfrac{\hat{p}}{2m} = -\dfrac{\hbar^2}{2m}\hat{\Delta},$
  $where\ \hat{\Delta} = \hat{\nabla}^2 = \dfrac{\partial^2}{\partial x^2} + \dfrac{\partial^2}{\partial y^2} + \dfrac{\partial^2}{\partial z^2};$ $\quad (5,\hat{T});\left(\begin{array}{c}\textit{operator}\\ \textit{kinetic}\\ \textit{energy}\end{array}\right)$
- $\hat{V}(\hat{r}) = V(r);$ $\quad (5,\hat{V});\left(\begin{array}{c}\textit{operator}\\ \textit{potintial}\\ \textit{energy}\end{array}\right)$
- $\hat{H} = \hat{T} + \hat{V}(\hat{r});$ $\quad (5,\hat{H});\left(\begin{array}{c}\textit{operator}\\ \textit{full energy}\\ \textit{Hamiltonian}\end{array}\right)$
- spin S $\left(\begin{array}{c}\textit{there is no}\\ \textit{classic analog}\end{array}\right).$ $\quad (5,\hat{S});\left(\begin{array}{c}\textit{operator}\\ \textit{spin}\end{array}\right)$

The first of quantum mechanics gives the relationship between the operators describing the physical quantities and the real numbers that are measured in the experiment.

Second principle of quantum mechanics (admissible values): *When measuring a physical quantity A, only numerical values* α_n *can be obtained, which are eigenvalues of the operator* $\hat{A}$ *of this quantity* [14].

The eigenvalues [14] of the Hermitian operator $\hat{A}$ are real, which determines the use of Hermitian operators to represent physical quantities, i.e. postulates that in the physical experiment only those values of the physical quantities belonging to the spectrum of the respective operator are measured. In the discrete spectrum, the experiment will measure only these discrete values [14]. The values measured in the experiment depend on the state of the system and the probabilities for each of the eigenvalues in that state. Prediction of experimental results in quantum mechanics is probabilistic; classical physics experimental results are predicted with absolute certainty [14].

Third principle of quantum mechanics (probabilities) [14]: *In the state* $|\Psi\rangle$ *of the quantum system, the probability when*

measuring a physical quantity A to obtain the eigenvalue α of the operator $\hat{A}$, corresponding to the eigenstate $|a\rangle$, is $\boldsymbol{p(\alpha) = |\langle a|\Psi\rangle|^2}$.

For a continuous spectrum $p(\alpha)$ is the probability density in $[\alpha, \alpha + d\alpha]$ eq. (5, ***p***); Decomposition of the wave function Ψ in the basis eigenfunctions $|\boldsymbol{a}\rangle$ of the operator $\hat{A}$ eq. (5,$|\Psi\rangle$); Possible interpretation of Eq. (5, $|\Psi\rangle$) is a representation of the fact that in the state Ψ of the quantum system the physical quantity has no definite value, and the vector of the system is a superposition of the eigenvectors of $\hat{A}$ *i.*e. the system exists simultaneously in all eigenstates of $\hat{A}$ as the probability is in the state $|a_n\rangle$ e $|c_n|^2 = |\langle a_n|\Psi\rangle|^2$ [14]. The probabilistic interpretation of the coefficients c_n justifies the normalization of the wave function eq. (5, 1,Ψ), which means that the total probability of finding the system in this basis is 1 eq. (5, $\langle\Psi|\Psi\rangle$); If the system state is eigenvector of $\hat{A}$ *i.*e. $|\Psi\rangle=|a_n\rangle \Rightarrow |c_n|^2 =1$ and $c_n = 0$. Therefore, the probability of obtaining the value α_n in the measurement is equal to 1, and for all other values the probability is 0. At that reason it is said, that eigenstates of the operator $\hat{A}$ the physical quantity *A has a certain value* [14]. ***Classical statistical physics [14]*:** We emphasize that probability is widely used, but in a different sense. It works with ensembles containing a large number N of particles. It is assumed that at any given time each particle has a well-defined coordinate and velocity; we simply do not have accurate information about them due to the large number of particles. One particle to have coordinate in $\boldsymbol{[x, x+\delta x]}$ and velocity in $\boldsymbol{[v, v+\delta v]}$; the number of particles in the ensemble that fall within these intervals is $\boldsymbol{n_M < N}$ with probability: $\boldsymbol{P_i = n_M/N}$, $\forall\ i \in [1, M]$. ***Quantum mechanics [14]:*** Quantum mechanics: a quantity A gives a specific non-averaged value in the general case when the system is not in a single vector of $\hat{A}$. In the experiment, an averaged probability distribution value is obtained from the eigenvalues $\boldsymbol{\alpha_n}$ of $\hat{A}$ with a certain probability $\boldsymbol{|c_n|^2}$. The probability in quantum mechanics to measure the eigenvalue $\boldsymbol{\alpha_n}$ is the number of measurements $\mathbf{N_{meas}}$ in which we obtain $\boldsymbol{\alpha_n}$ divided by the number of the total number of measurements $\mathbf{N_{tot}}$ *i.*e. $\boldsymbol{\alpha_n = N_{meas}/N_{tot}}$. The average value of the quantity *A* in the state $|\Psi\rangle$ is eq. ($\langle A\rangle$), in normalized $|\Psi\rangle$ it $\langle\Psi|\Psi\rangle = 1$ and $\langle A\rangle = \langle\Psi|\hat{A}|\Psi\rangle$. Use eq. (5, $|\Psi\rangle$) and we have the eq. (5, $\langle\Psi|\hat{A}|\Psi\rangle$), where we use the orthonormal of the basis $\langle a_k|a_n\rangle = \delta_{kn}$. Because according to the second principle of quantum mechanics α_n the values obtained in the measurement of the magnitude A, and $|c_n|^2$ according to the third principle is the probability of measuring this value α_n, this results in a well-known formula for the mean value. Because the operator $\hat{A}^\dagger$ is Hermitian, $\hat{A}^\dagger = \hat{A}$ then the average value is real $\hat{A} = \Re$ and we have eq. (5, $\langle\mathbf{A}\rangle^*$) [11].

$$p(\alpha)d\alpha = |\langle a|\Psi\rangle|^2 d\alpha, \qquad (5, p)$$

$$|\Psi\rangle = \sum_n c_n|a_n\rangle, \text{where } c_n = \langle a|\Psi\rangle, \qquad (5,|\Psi\rangle)$$

$$1 = \langle\Psi|\Psi\rangle = \sum_k \sum_n c_k^* c_n \langle a_k|a_n\rangle = \sum_k \sum_n c_k^* c_n \delta_{kn} = \sum_n |c_n|^2, \qquad (5,\langle\Psi|\Psi\rangle)$$

$$\langle A\rangle = \bar{A} = \frac{\langle\Psi|\hat{A}|\Psi\rangle}{\langle\Psi|\Psi\rangle}, \qquad (5,\langle A\rangle)$$

$$\langle\Psi|\hat{A}|\Psi\rangle = \sum_k \sum_n c_k^* c_n \langle a_k|\hat{A}|a_n\rangle = \sum_k \sum_n c_k^* c_n \langle a_k|a_n\rangle = \sum_n |c_n|^2 a_n = \langle A\rangle, (5,\langle\Psi|\hat{A}|\Psi\rangle)$$

$$\langle A\rangle^* = \frac{\langle\Psi|\hat{A}|\Psi\rangle^*}{\langle\Psi|\Psi\rangle^*} = \frac{\langle\Psi|\hat{A}|\Psi\rangle}{\langle\Psi|\Psi\rangle} = \langle A\rangle. \qquad (5,\langle A\rangle^*)$$

$(5, p)$ — CONTINUOUS SPECTRUM PROBABILITY DENCITY $[\alpha, \alpha + d\alpha]$

$(5,|\Psi\rangle)$ — DECOMPOSITION OF Ψ IN BASIS $|a_n\rangle$ OF EIGENVALUES

$(5,\langle\Psi|\Psi\rangle)$ — TOTAL PROBABILITY 1 OF THE SYSTEM TO BE ON THIS BASIS

$(5,\langle A\rangle)$ — AVERAGE VALUE OF MAGNITUDE $\hat{A}$ IN STATE Ψ

$(5,\langle\Psi|\hat{A}|\Psi\rangle)$ — USED BY $|\Psi\rangle$ DECOMPOSITION EIGENVALUE $\hat{A}$

$(5,\langle A\rangle^*)$ — AVERAGE REAL VALUE $\hat{A} \in \Re$

Equation (5, $\langle\mathbf{A}\rangle^*$) provides the ability to predict the statistical result (i.e. a large number of measurements) from the physical experiment in quantum mechanics [14].

Fourth principle of quantum mechanics (postulate for measurement) [14]: *If at the measurement of a physical quantity A is get the eigenvalue α of the operator $\hat{A}$, corresponding to the eigenvalue $|a\rangle$, then after the measurement the quantum system is in the state $|a\rangle$.*

The act of measurement prepares the system in the measured state $|a\rangle$, i.e. *the wave function* $|\Psi\rangle$ *"collapses" in the state* $|a\rangle$ [14]. The Copenhagen interpretation of quantum mechanics: before the act of measurement, the quantum system may be in superposition of eigenvalues of the operator $\hat{A}$, but the measurement causes the system to "choose" one of them in which to "collapse". It is *a random process*. It follows that a quantum system can be prepared in any eigenstate of $|a\rangle$ eigenstate of the operator $\hat{A}$: a sufficient number of measurements are made until we get the eigenvalue of α, which will signal that the system is in the desired state $|a\rangle$ [14]. This is due to the fact that: our instruments are macroscopic; the measurement itself changes the microscopic system due to the fact that the instrument is much larger than it and in the process of measurement the microparticle inevitably interacts with the instrument. *This is another difference from classical physics, where the properties of bodies are measured without the bodies being changed* [14].

In recent years, ways have been found and demonstrated to measure some quantum systems without destroying them: *demolition-free measurement bubble without breaking* [14]. Today, measurement is an automated process and is an objective process of microparticle/device interaction [14].

Relation between **commutation of two operators** and *the simultaneous measurability of the corresponding physicals quantities* [14]: 1-st measurement of the physical quantity *A* gives the eigenvalue α of the operators $\hat{A}$ then the system is in its eigenstate $|a\rangle$: eq. (5, Ψ collapse $|a\rangle$, $\boldsymbol{[A, A] = 0}$), the wave function $|\Psi\rangle$ is collapse in its eigenstate $|a\rangle$; at 2-nd measurement of the same quantity *A* will give the same value $|a\rangle$, because $|\Psi\rangle\equiv|a\rangle$ [14]. The mathematical equivalent of that fact is, that every operator commutates with itself: $\boldsymbol{[A, A] = 0}$; Measurements of two quantities firs of A after B: at commutation of the two operators $\hat{B}$ and $\hat{A}$, $[\hat{B}, \hat{A}] = 0 \Rightarrow$ both operators have the same eigenstates $|b\rangle\equiv|a\rangle$ i.e. wave function Ψ collapse in $|a\rangle$, which is eigenstate of the operator $\hat{B}$; which means that after measurement of B the system remains in $|a\rangle$ [14]. In that state $|a\rangle$ the quantities A and B have a certain value i.e. 2they can to be measured together; or analogically when 1st B measure and so on, see eq. (5,*a*,$[\hat{A}, \hat{B}]$=0) and (5,*b*,$[\hat{B}, \hat{A}] = 0$); At not commutations operators $\hat{A}$ and $\hat{B}$ then they have different eigenstates. When measuring A $\Rightarrow|\Psi\rangle$ collapses in $|a\rangle$, which is no longer eigenvalue of the operator $\hat{B}$, but is a kind of superposition of eigenvalues of $\hat{B}$ [14]. When measuring $\hat{B}$ the wave function $|\Psi\rangle=|a\rangle$ will collapses in other state $|b\rangle$ of eigenstates of the $\hat{B}$ such of $|b\rangle\neq|a\rangle$. Therefore, quantities $\hat{A}$ and $\hat{B}$ ***cannot be measured together*** [14]. If we measure 1st *A* after *B* then the system will first be in state $|a\rangle$ and then in $|b\rangle$ and then vice versa, B is measured, then A is measured, then the system is first in state $|b\rangle$, then it is in state $|a\rangle$ see eq. (5, *c*) and eq. (5, *d*) i.e. ***different final state*** [14].

$$|\Psi\rangle \xrightarrow{\hat{A}} |a\rangle, \qquad \left(5, \begin{matrix}\Psi\ collapse|a\rangle \\ [A, A] = 0\end{matrix}\right)$$

$$|\Psi\rangle \xrightarrow{\hat{A}} |a\rangle \xrightarrow{\hat{B}} |a\rangle, \qquad (5, a, [\hat{A}, \hat{B}] = 0)$$

$$|\Psi\rangle \xrightarrow{\hat{B}} |a\rangle \xrightarrow{\hat{A}} |a\rangle, \qquad (5, b, [\hat{B}, \hat{A}] = 0)$$

$$|\Psi\rangle \xrightarrow{\hat{A}} |a\rangle \xrightarrow{\hat{B}} |b\rangle, \qquad (5, c, [\hat{A}, \hat{B}] \neq 0)$$

$$|\Psi\rangle \xrightarrow{\hat{B}} |b\rangle \xrightarrow{\hat{A}} |a\rangle, \qquad (5, d, [\hat{B}, \hat{A}] \neq 0)$$

The maximum set of quantities that can be measured simultaneously (corresponding to mutually commutating) is called *a complete set of dynamic variables* of the system [14].

Fifth principle of quantum mechanics (evolution) [14]. *The evolution of the wave function of a quantum system with a Hamiltonian $\hat{H}$ in time is determined by Schrödinger's equation*:

$$i\hbar\frac{\partial|\Psi\rangle}{\partial t} = \hat{H}|\Psi\rangle, \qquad \textbf{(5, Schrödinger,}\Psi\textbf{)}$$

where $\boldsymbol{\hbar = h/2\pi = 1{,}054\times10^{-34}}$ **J.s** is the reduced Planck constant.

Eq. (5, Schrödinger,Ψ) is also called *the wave equation*, it is a linear homogeneous equation partial differential equation in time (first order) and coordinates (second order) [14]. This is a *parabolic* partial differential equation that is *numerically unstable* and requires special methods for numerical integration. Eq. (5, Schrödinger,Ψ) is differential equation of first order at the time than *the wave function* $|\Psi(t)\rangle$ *in every one moment is defined unambiguously by the wave function* $|\Psi(t_0)\rangle$ *at a previous moment* $t_0<t$. This property expresses **the principle of causality** in quantum mechanics. *Mathematical methodology* [14]: 1. The full use of mathematics: Example: Theorem of Emmy Noether [17]. Any finite–parametric transformation, depending on s constant parameters of the coordinates and field function zeroing the variation of the action functional, provide that the equation that the equations of motion are satisfied, corresponds to s dynamic invariants, i.e. time–conservation combinations of field functions and their derivatives. This theorem is also in classical mechanics [30].2. Mathematical physics: Algebra [31] Abstractly, formally or axiomatically, presenting new concepts in group theory, field theory, normalization theory, ideal theory and algebra theory, and presents internal connections. Many interesting is algebraic topology. 3. The application of mathematics in theory of material science. Here is a clear request for the application mathematics and mathematical physics to describing first and second order phase transition. Connection between the theory of thermal conductivity are: Stefan type tasks [1, 22 and 23]. The application mathematics, and mathematical physics is done through powerful computing infrastructure. Such a software product is CASTEP [**2 and 5**].

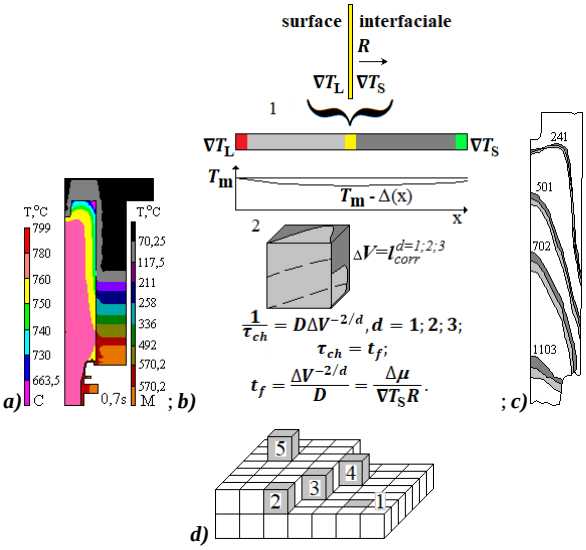


Fig. 10 *Mathematical methodology for* ***first order phase transition*** *(material science): 1. The full use of mathematics; 2. Mathematical physics; 3. Specific interest to application:* ***a)*** *Stefan–Schwartz solidification of (cast/mold) 3D FEM ;* ***b)*** *Multiscale approach: 1 Stefan's task [22]:* $\lambda_{S(L)}$ *thermal conductivity coefficients;* $\nabla T_{S(L)}$ *– temperatures gradients at the interphase surface and R – speed of movement;2* $T_m - \Delta(x)$ *super-cooled zone* $\Rightarrow \Delta V$ *correlation volume,* τ_{ch} *– characteristic time, D – diffusion coefficient,* t_f *– solidification local time of correlation volume,* $\Delta\mu$ *– thermodynamic driving force;* ***c)*** *technological solidification 3D FEM;* ***d)*** *[**39**] 1 – atom embedidded into the outermost crystal plane, 2 – atom embedidded into the step edge, 3 – atom in a* ***half****-crystal (kink) position, 4 – atom adsorbed at the step, 5 – atom adsorbed on the crystal face.*

$$\textbf{Classical mathematical methdology on the works [9; 1 and 40; 38 and 39]}$$

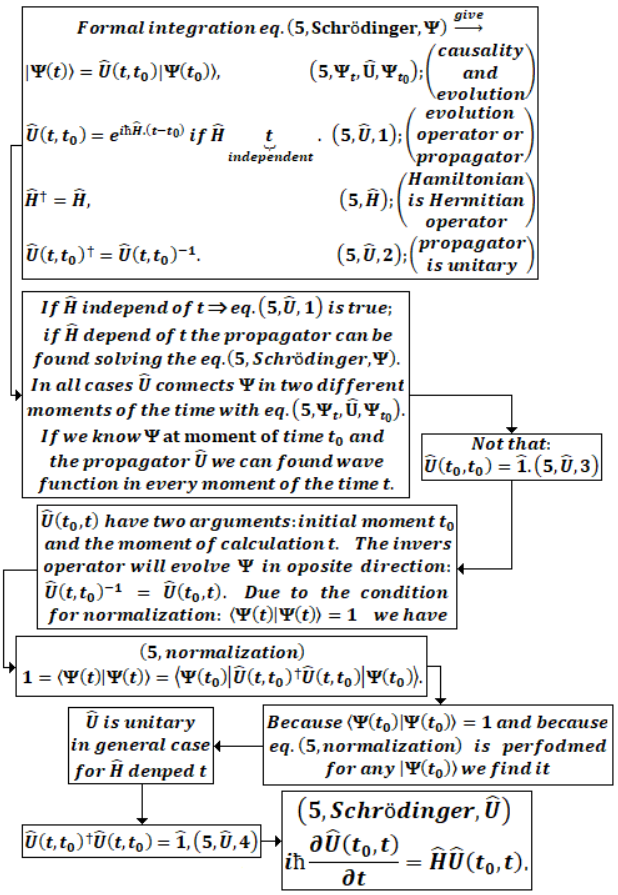
$$\lambda_S \nabla T_S - \lambda_L \nabla T_L = \rho_S Q_m R, \qquad (\textit{Flemings}, [9])$$

$$\frac{dx_S}{dt}\frac{1}{L_S}\left[\lambda_S \frac{\partial T}{\partial x}_{|x_S-0} - \lambda_L \frac{\partial T}{\partial x}_{|x_L+0}\right], \frac{dx_L}{dt}\frac{1}{L_L}\left[\lambda_S \frac{\partial T}{\partial x}_{|x_S-0} - \lambda_L \frac{\partial T}{\partial x}_{|x_L+0}\right], \left(\begin{matrix}\textit{Bushev}\\ \textit{Georgiev}\end{matrix}, [1, 40]\right)$$

$$\dot{Z}_n(\tau) = \sum_m^M [f_{mn}(\tau)Z_m(\tau) - f_{nm}(\tau)Z_n(\tau)] + K_n(\tau) - L_n(\tau) \; for \qquad (\textit{Kashchiev}, [38])$$

$$\Theta_1 = 1 - exp\left[-\pi N_S \left(\int_0^t v(t')\,dt'\right)^2\right]. \qquad \left(\textit{Markov}\,[39], \begin{matrix}\textit{1st monolayer}\\ \textit{surface}\\ \textit{coverd}\end{matrix}\right)$$

For eq. (Kashchiev [38]): Z_n, f_{mn}, f_{nm}, K_n, L_n – complex number of n atoms, frequencies of attachment/detachment of atoms for nucleus, transient frequencies of entry and exit of the system from ready complexes; for eq. (Markov, [39]) Θ_1 – 1st monolayer covered, N_S – saturation nucleus density; *v* – rate of advance of steps. Kashchiev's equation is designet for variable supercooling. It provides basis information for different supercooling of the total of nuclei of the new phase and number of atoms or particle make up the nuclei. Knowing the number of particles that make up the nuclei, we can apply the lattice models or software product CASTEP [2 and 5]: for an ideal crystal or for real polycristals. The mathematical methodology within Fig. 10 and (Flemings [9], Bushev and Georgiev [1 and 40], Kashchiev [38], Markov [39]) present a multi–scale from macro- to average level i.e. the need of quantum mechanics:



Explain of the math methodology [14]: For a fixed t_0 and t is an independent variable, we can replace eq. (5, Ψ_t, $\hat{U}$, Ψ_{t0}) in eq. (5, Schrödinger, Ψ) as we obtain (5, Schrödinger, $\hat{U}$) with initial condition eq. (5, $\hat{U}$, 3) [14]. Therefore, the propagator eq. (5, $\hat{U}$, 1) satisfies the Schrödinger equation with an initial condition that does not depend on the state of the system, unlike the Schrödinger equation eq. (5, Schrödinger,Ψ) for the wave function. Note [14] the operator equation eq. (5, Schrödinger,$\hat{U}$) is much more difficult to solve than solving eq. (5, Schrödinger,Ψ). The reason is that solving eq. (5, Schrödinger,$\hat{U}$) for $\hat{U}(t_0, t)$ is equivalent to solving eq. (5, Schrödinger,Ψ) for an arbitrary initial condition for $|\Psi(t)\rangle$ [14].

Heisenberg's relation for uncertainty: States with certain values of physical quantities

Clasical Mechanics	Quantum Mechanics
$D_A = (A - \bar{A})^2$ $D_A = \frac{1}{N}\sum_{k=1}^{N}(A_k - \bar{A})^2$ $A_1, A_2, \ldots, A_N$; *A and* $\bar{A} = \sum_{k=1}^{N} A_k / N.$	$\hat{D}_A = (\hat{A} - \hat{A}\hat{1})^2, \hat{A}: \hat{A}^\dagger = \hat{A}.$ $\langle \hat{D}_A \rangle = \langle \Psi | \hat{D}_A | \Psi \rangle =$ $\left\langle \Psi \middle| (\hat{A} - \hat{A}\hat{1})^2 \middle| \Psi \right\rangle =$ $\left(\Psi, (\hat{A} - \hat{A}\hat{1})^2 \Psi\right) =$ $\left((\hat{A} - \hat{A}\hat{1})\Psi, (\hat{A} - \hat{A}\hat{1})\Psi\right) =$ $\|(\hat{A} - \hat{A}\hat{1})\Psi\|^2 \geq 0.$

If $\langle\widehat{D}_A\rangle$=0 of physical quantity A i.e. $\left(\hat{A}-\bar{A}\hat{1}\right)$ or$\hat{A}|\Psi\rangle=\bar{A}|\Psi\rangle$, A certain value in state $|\Psi\rangle$, which is one of the eigenstates $|a_n\rangle$ of the operator $\hat{A}$: $|\Psi\rangle = |a_n\rangle$. And more the average value of A is the eigenvalue of $\hat{A}$ in this state: $\bar{A}=\alpha_n$. For physical quantities $A\neq B$ has simultaneously defined values, such as only those states $|a_n\rangle$, which are simultaneously eigenstates of the respective operators $\hat{A}$ and$\hat{B}$:

$$\hat{A}|a_n\rangle=\alpha_n|a_n\rangle,\ \ \hat{B}|a_n\rangle=\beta_n|a_n\rangle. \qquad (5, \hat{A}\ and\ \hat{B})$$

From eq. (5, $\hat{A}$ and$\hat{B}$) that it follows at commutation of the operators $\hat{A}$ and $\hat{B}$ *i.e.* $[\hat{A},\hat{B}]$ = 0 and they have the same eigenvectors, they can have simultaneously certain values i.e. *they can be* ***measured simultaneously*** *with any accuracy* if the quantum system is in any eigenstates of $\hat{A}$ and$\hat{B}$. **Definition:** *A set of physical quantities is called* ***complete*** *if the respective operators switch with each other and this set cannot be extended*. **Definition:** *A set of physical quantities is called* ***complete*** *if the respective operators' commutation with each other and this set cannot be extended.*

Heisenberg's relation for uncertainty **math schemes are [14]: For two not commutation operators $\hat{A}$ and $\hat{B}$ i.e. $[\hat{A},\hat{B}]\neq 0$**

$$used\ \hat{D}_A=\left(\hat{A}-\bar{A}\hat{1}\right)^2, \hat{D}_B=\left(\hat{B}-\bar{B}\hat{1}\right)^2, \qquad (5, \hat{D}_A, \hat{D}_B)$$

$$[\hat{A},\hat{B}]=i\hat{C}, \qquad (5, i\hat{C})$$

$$\hat{C}=-i[\hat{A},\hat{B}]=-i(\hat{A}\hat{B}-\hat{B}\hat{A}),$$

$$\hat{C}^{\dagger}=i(\hat{A}\hat{B}-\hat{B}\hat{A})^{\dagger}=i(\hat{B}\hat{A}-\hat{A}\hat{B})=\hat{C}. \qquad (5, \hat{C})$$

$$\hat{\Delta}_A=\hat{A}-\bar{A}\hat{1}, \hat{\Delta}_B=\hat{B}-\bar{B}\hat{1}\Rightarrow \hat{D}_A=\hat{\Delta}_A^2, \hat{D}_B=\hat{\Delta}_B^2, \qquad (5, \hat{\Delta}_A^2, \hat{\Delta}_B^2)$$

$$[\hat{\Delta}_A,\hat{\Delta}_B]=i\hat{C}. \qquad (5, i\hat{C})$$

$$\langle\hat{D}_A\rangle=\langle\Psi|\hat{\Delta}_A^2|\Psi\rangle=\|\hat{\Delta}_A\Psi\|^2,$$

$$\langle\hat{D}_B\rangle=\langle\Psi|\hat{\Delta}_B^2|\Psi\rangle=\|\hat{\Delta}_B\Psi\|^2. \qquad \left(5, \begin{matrix}\langle\hat{D}_A\rangle,\\ \langle\hat{D}_B\rangle\end{matrix}\right)$$

$$|\langle a|b\rangle|\leq\|a\|\|b\|, and\ |\Im(z)|\leq|z|. \qquad (5, Inequalities, 1\ and\ 2)$$

$$Use\ inequalities: 1^{st}\left[\begin{matrix}scalar\ product\\ of\ 2\ vectors\\ is\ product\ of\\ its\ lengths\end{matrix}\right]; 2^{nd}: \begin{matrix}\Im(z)=(z-z^*)/(2i)\\ |z|=\sqrt{\Re(z)^2+\Im(z)^2}.\end{matrix}\Rightarrow$$

$$\sqrt{\langle\hat{D}_A\rangle\langle\hat{D}_B\rangle}=\|\hat{\Delta}_A\Psi\|\|\hat{\Delta}_B\Psi\|\geq|\langle\hat{\Delta}_A\Psi|\hat{\Delta}_B\Psi\rangle|\geq|\Im(\langle\hat{\Delta}_A\Psi|\hat{\Delta}_B\Psi\rangle)|=$$

$$|(\langle\hat{\Delta}_A\Psi|\hat{\Delta}_B\Psi\rangle-\langle\hat{\Delta}_A\Psi|\hat{\Delta}_B\Psi\rangle^*)/2i|=\frac{1}{2}|\langle\hat{\Delta}_A\Psi|\hat{\Delta}_B\Psi\rangle-\langle\hat{\Delta}_B\Psi|\hat{\Delta}_A\Psi\rangle|=$$

$$\frac{1}{2}|\langle\Psi|\hat{\Delta}_A\hat{\Delta}_B\Psi\rangle-\langle\Psi|\hat{\Delta}_B\hat{\Delta}_A\Psi\rangle|=\frac{1}{2}|\langle\Psi|[\hat{\Delta}_A,\hat{\Delta}_B]|\Psi\rangle|=$$

$$\frac{1}{2}|\langle\Psi|i\hat{C}\,|\Psi\rangle|=\frac{1}{2}\langle C\rangle. \qquad \left(5, \sqrt{\langle\hat{D}_A\rangle\langle\hat{D}_B\rangle}\right)$$

And finally it obtained

$$\Delta_A=\sqrt{\langle\hat{D}_A\rangle},\ \Delta_B=\sqrt{\langle\hat{D}_B\rangle},\ \Rightarrow \qquad \left(5, \begin{matrix}uncertainty\\ \Delta_A,\Delta_B\end{matrix}\right)$$

$$\Delta_A\Delta_B\geq\frac{1}{2}\langle C\rangle. \qquad \left(\begin{matrix}Heisenberg\\ 5, uncertainty\\ A\ and\ B\end{matrix}\right)$$

Heisenberg's ratio uncertainty of two quantities A and B [20]. ***Heisenberg uncertainty ratio: examples: coordinates and momentum; commutation*** $[\hat{x},\hat{p}_x]=0$. Very important example Heisenberg uncertainty. The commutation of the operators of the coordinate $\hat{x}$ and the momentum $\hat{p}_x=-i\hbar(d/dx)$ is $[\hat{x},\hat{p}_x]$ = 0; the mathematical presentation is eq.(5, $[\hat{x},\hat{p}_x]$=0) because eq.(5, 1, $[\hat{x},\hat{p}_x]$=0) in that case $\Rightarrow \hat{C}=\hbar\hat{1}$ and $\hat{C}=\hbar$. Therefore, the Heisenberg ratio of coordinate and momentum (5, Heisenberg) i.e.

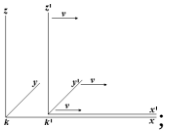
$$\left.\begin{matrix}[\hat{x},\hat{p}_x]=\hat{x}\hat{p}_x-\hat{p}_x\hat{x}=-i\hbar\left(x\frac{d}{dx}-\frac{d}{dx}x\right)=\\ -i\hbar\left(x\frac{d}{dx}-x\frac{d}{dx}-1\right)=i\hbar, \qquad (5, [\hat{x},\hat{p}_x]=0)\\ \frac{d}{dx}[xf(x)]=f(x)+x\frac{df(x)}{dx}. (5, 1, [\hat{x},\hat{p}_x]=0)\end{matrix}\right| \begin{matrix}(5, Heisenberg)\\ \left.\begin{matrix}\Delta_x\Delta_{p_x}\geq\hbar/2\\ \Delta_y\Delta_{p_y}\geq\hbar/2\\ \Delta_z\Delta_{p_x}\geq\hbar/2\\ \Delta E\Delta t\geq\hbar/2\end{matrix}\right\}.\end{matrix}$$

we have inequalities shown see (4, Heisenberg). The inequality (5, Heisenberg) shows that in quantum mechanics it does not allow the simultaneous measurement with absolute accuracy of the coordinate and momentum of a particle. The ratio $\Delta_x\Delta p_x\approx\hbar$ is a fundamental physical limitation and cannot be overcome by increasing the accuracy of measuring instruments. However, ħ is a very small number to reach in an experiment, but there are already experiments testing the ratio of Heisenberg (albeit in other variables).

2.1.2 Einstein methodology [21] very important

Principle of relativity (in a limited sense) [21]: if, with respect to **K**, **K**/ is a uniformly moving coordinate system devoid of rotation, ⇒ natural phenomena follow their course with respect to **K**/ exactly according to the same laws as with respect to **K [21]**.

Contradiction [21]: the law of **c** with the principle of relativity; avoid: by modifying the relationship between *place (Δl) and time (Δt) to* ***K***/ *and* ***K*** i.e. transformation [21] law for *Δl* and *Δt* quantities of an event passing from one **K**/ to the other **K**; (see Scheme 1):



Scheme.1.;

for use **„Lorentz transformation" K**, for Δl/, Δt/ use **„Galileo's transformation"** as „Galileo's transformation" [21] is derived from „Lorentz transformation" in which **c** is replace by the sign for ∞:

Lorentz transformation

$$x'=\frac{x-vt}{\sqrt{1-\frac{v^2}{c^2}}}, y'=y, z'=z, t'=\frac{t-\frac{v}{c^2}x}{\sqrt{1-\frac{v^2}{c^2}}}.$$ **Galileo's transformation** $x'=x-vt, y'=y, z'=z, t'=t$.

Mathematical–physical model for the law of transformation between (x, y, z, t) and (x/, y/, z/, t/) [21]; Substituting x with the value of **c**t in the 1st and 4th equations of „Lorentz transformation" we get the connetion between **K** and **K**/ [21]:

$$x=ct\Rightarrow \begin{matrix}x'=\frac{x-vt}{\sqrt{1-\frac{v^2}{c^2}}},\\ t'=\frac{t-\frac{v}{c^2}x}{\sqrt{1-\frac{v^2}{c^2}}},\end{matrix} \Rightarrow x'=ct'$$

. Thus **c** is the same with respect to **K**/ [21]. When the light rays move in another direction, the result is the same [21].

Heuristic value of the theory of relativity from the experiment of the two postulates [21]: 1. The principle of relativity is valid; 2. The speed of light propagation in vacuum is considered to be equal to the constant **c** [21]. When combining the postulates, the law of transformation is obtained for the perpendicular (⊥–lar) coordinates, x, y, z, and time t, which constitute the processes of nature. For this we did not receive the „translation of Galileo ", but unlike the class of mechanics, we receive the „translation of Lorentz "[21]. Postulate 2 [21] *has been accepted by actual (1920) knowledge and has become an important methodology*. Knowing the „Lorentz translation ", it is combined with the principle of relativity and the theory is summarized as follows [21]: Each general law [21] of nature must be constructed in such a way as to be transformed into a law of exactly the same form, when instead of the space–time variables x, y, z, t of the initial coordinate system **K**, the space–time variables x/, y/ z/ t/ are introduced to a new space **K**/. Thus, the relationship between the variables (x, y, z, t) and (x/, y/, z/,t/)is given by the „translation of Lorentz " [21]. *It is a definite mathematical condition that the theory of relativity requires a natural law, and by virtue of this the theory becomes a valuable heuristic aid in the search for general natural laws [21].* If a general natural law is found that does not satisfy this condition, then at least one of the two basic assumptions of the theory would be refuted [21]

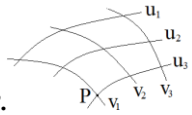
Basic for physics are the two laws of conservation [21]: the law of conservation energy; law of conservation mass; quite dependent on each other. Classical mechanics [21] is modified to comply with the requirements of the special theory of relativity: mainly the laws of

fast motions with velocities of matter v not much less than of **c**; only the rapid motions of ions and electrons [21]. The body has the same energy ≡ the body with mass ($\boldsymbol{m + E_0/c^2}$) moving with speed v; the inertial mass varies depending on the change in body energy. ***The inertial mass of a system of bodies can be considerred as a measure of its energy [21]***. The law of conservation of mass [21] of the system becomes identical with the law of conservation of energy and is only provide that the system neither receives nor radiates energy [21]. Faraday–Maxwell success [21] in interpreting electromagnetic action from a distance led physicists to believed that there were no such thigs as instantaneous remote action (without the involvement of a mediating medium [21]) such as Newton's law of gravitation [21]. According to theory of relativity, remote action at the speed of light always replaces the place of instantaneous remote action or remote action with final transmission speed [21]. This is due to the fact that velocity **c** plays a major role in this theory. The theory of relativity for contraction [21] of the ether is correct; according to theory there is no „particularly preferred "(unique) coordinate system since the introduction of another idea [21]. Michelson and Morley's mirror system has shrunk to a coordinate system at rest relative to the sun [21].

The special principle of relativity [21]: ***the principle of the physical relativity of all uniform motion***.

The 4D spatio–temporal continuum of the theory of relativity, in its most essential formal properties, shows a clear connection with the 3D continuum of Euclid's geometry space. An important connection, the coordinate of time t is replaced by the imaginary quantity $\sqrt{-1}\cdot ct$. Natural laws that meet the requirements of the special theory of relativity take mathematical forms in which the coordinate of time plays the same role as the three spatial coordinates. Formally, these four coordinates in Euclidean geometry.

Gauss co–odrinates:



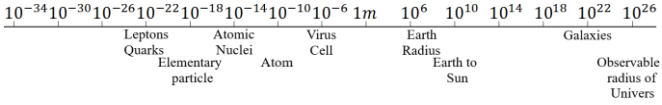
Scheme.2.

Scheme 2 shows an arbitrary surface with an „infinitely dense" grid of coordinate curves u– v–curves; Each point P and its neighbor P/ are represented by: $\boldsymbol{P: u, v;\ P: u + du, v + dv}$. According to Gauss $\boldsymbol{ds^2 = g_{11}du^2 + 2g_{12}dudv + g_{22}du^2}$, where g_{11} g_{12} g_{22}, depend in a specific way on the u– and v–curves. If the points on the surface form a Euclidean continuum, only in this case the points x_1, x_2, x_3, x_4, can be connected to the points on the continuum and we just have $\boldsymbol{ds^2 = dx_1^2 + dx_2^2 + dx_3^2 + dx_4^2}$.

General principle of relativity [21]: All reference bodies **K**, **K/**, etc., are equivalent for describing natural phenomena (formulation of the general laws of nature), regardless of their state of motion [21]. The coordinate system of Gauss takes the place of a reference body. And the fundamental idea of the general principle of relativity: "*All Gaussian co-ordinate systems are essentially equivalent for the formulation of the general laws of nature*."

2.2 Quantum physics

Leander Litov [17] from the infinity small to the infinity large



Physics (from the ancient Greek φυσικός (physical) - "natural", *φύσις* (physical) "nature") is a natural science that studies the general and fundamental laws that determine the structure and evolution of the material world [19]. Physics has two great sections: *Theoretical* and *Experimental*, which develop mutually. *Theoretical physics* are mathematical models whose results are confirmed by physical experiments. *Mathematical physics* was separated from theoretical physics more than 2000 years ago. The creation of *quantum mechanics* and *the theory of relativity* defines a new meaning of mathematical physics [18]. *Quantum physics* is a branch of theoretical physics that combines: quantum mechanics; quantum field theory with applications in particle physics; nuclear physics; high energy physics, and other; quantum optics; and subsections of solid-state quantum theory or quantum statistics.

Quantum physics is necessary to understand the properties of *solids*, *atoms*, *nuclei*, *subnuclear particles* and *light* i.e. and ***understanding quantum principles has necessitated fundamental changes in the way people view nature*** [17]. The main task of physics is to try to answer two fundamental questions [17]: **1.** What are the elementary components of matter? 2. What are the fundamental forces controlling fiery behavior? *Quantum physics* considers both questions through *the maximum generalization*: from the infinite small (elementary particles) to the infinitely large physics (Universe) [17]. What is the universe made of? The modern answer is: 4% normal matter; 23% Dark matter; 73% dark energy [17].

Elementary particle - for it there is no experimental evidence for the existence of an internal structure, i.e. it is not composed of smaller particles. Elementary particles [17 and 18]: **Fermions**: **1. *Quarks***: Upper (u-quarks), Lower (d-quarks), Strange (s-quarks), Charming (c-quarks), Bottom (b-quarks), Top (t-quarks); **2. *Leptons***: Electron, Positron, Muon, Taon, Nutrino, Antineutrino; **Bosons**: Photon, W boson, Z boson, X boson, Y boson, Higgs boson, Graviton, Gluon; **Hadrons**: **1. Mesons**: Peony; **2. *Baryons***: Proton, Neutron. Peony (short for pi (π meson) are three elementary particles: π^0, π^+ and π^-, which are the lightest mesons and are formed by a quark and an antiquark. It is known that ***each particle type has a similar antiparticle*** *with the same mass but with opposite charge* (for example *electric charge*) [17 and 18]. Elementary particles are the basic building blocks of matter. Hadron is a particle that interacts strongly. Hadrons are made of quarks, but differ in type and number. The quarks connect in the hadrons by gluons exchange.

The elementary particles are classified on the basis of their mass until the creation of ***the standard model***: ***leptons*** (from Greece leptos - small, light); ***mesons*** (from Greece mesos - middle); ***baryons*** (from Greece baris - heavy) see Fig.10

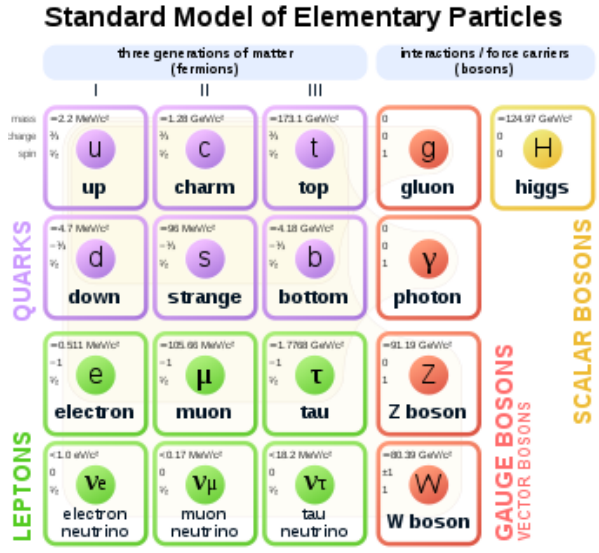


Fig. 11 *of [19] in the right column are the calibration bosons and the Higgs boson and see Table 2 of [17]. Gravity is not included in the standard model.*

The theoretical standard model [17, 18 and 19] is construction describing the strong, electromagnetic and weak interactions of all elementary particles

Table 2. The fundamental interactions in nature [17].

Interaction	Current theory	Transportable particles	Relative strength	Long-distance behavior
Strongly	Quantum chromodynamics	Gluons	10^{38}	1
Electromagnetic	Quantum electrodynamics	Photons	10^{36}	$1/r^2$
Weak	Electroweak theory	W and Z bosons	10^{25}	$e^{-m_{w,z}r}/r$
Gravitational	Theory of Relativity	Gravitoni	1	$1/r^2$

Gravity is not included in the standard model. Basics of the standard model [17÷19]: **1b**. All known matter consists of fundamental particles: 6 leptons (electron, muon tau-lepton and three generations of neutrinos) and 6 quarks (u, d, s, c, b, t), uniting in three generations of fermions; **2b**. Quarks participate in strong, electromagnetic and weak interactions; charged leptons (electron, muon, tau-lepton) - in weak and electromagnetic interactions; neutrino - only in weak interactions; **3b**. The carriers of the three interactions (strong, electromagnetic and weak) are the calibration bosons: 8 gluons for strong interaction (symmetry group SU (3)); 3 heavy gauge bosons (W, W, Z) for weak interaction (symmetry group SU (2)); one photon for the electromagnetic interaction (symmetry group U (1)). These interactions arise and are a consequence of the postulate: our world is symmetrical with respect to three types of calibration transformations; **4b**. The weak interaction can mix fermions of different generations, leading to instability of all particles except the lightest, and to such effects as disruption of CP invariance and neutrino oscillations. ***External parameters for the standard model are*** [17 and 19]: ***lepton masses*** (3 parameters, the neutrino is assumed to be massless) and *the quarks* (6 parameters), which are interpreted as constants of the interaction of their fields with the Higgs boson field; ***the parameters of the CKM-matrix of quarks***, which are interpreted as constants of the interaction of quarks with the electroweak field; *two parameters uniquely related to* ***the Higgs boson***; *three interaction constants* related to ***the calibration groups U (1), SU (2) and SU (3)*** and characterizing the relative intensity of the electromagnetic, weak and strong interactions. The standard model a combination of electromagnetic and weak interaction was formulated by S. Glashow, S. Weinberg and A. Salam, and was completed by P. Higgs, a spontaneous symmetry violation explaining the origin of the mass of the elementary particles [17, 18 and 19].

Methodology [21]: Schrödinger equation → Klein-Gordon equation → Dirac equation; introduced with next simple scheme on the base [21, 35, 20 and 32]; Very simple scheme idea of our methodology [21]: Schrödinger equation → Klein-Gordon equation → Dirac equation; introduced with next simple scheme on the base [21, 20, 33 and 32];

$$\left(\begin{array}{c}\textit{Similarly Relativism or}\\ \text{Not the E } \textit{is associated}\\ \textit{the operator } i\hbar\partial/\partial t\end{array}\right)\Rightarrow\left[\begin{array}{c}\textit{That means that time dependent}\\ \textit{in state of define energy is}\\ e^{-iEt/\hbar}.\end{array}\right]$$

$$\Downarrow$$

$$\left[\begin{array}{c}\textit{That relationship between}\\ \textit{energy and frequency is}\\ \textit{than Plank}-\textit{Einsteins}\\ \textit{relation } E=\hbar\omega.\end{array}\right]\Leftarrow\left[\begin{array}{c}\textit{That allows the energy to be}\\ \textit{associated with angular}\\ \textit{frequency } \omega\rightarrow e^{-i\omega t/\hbar}.\end{array}\right]$$

$$1\left[i\hbar\frac{\partial\Psi}{\partial t}=-\frac{\hbar^2}{2m}\Delta\Psi\right]\rightarrow 2\left[\begin{array}{c}\textbf{Solution:}\\ \Psi=ce^{-iEt/\hbar}\psi\end{array}\right]$$

$$3\left[-\frac{1}{c^2}\frac{\partial^2\Psi}{\partial t^2}+\nabla^2\Psi=\left(\frac{mc^2}{\hbar c}\right)^2\Psi\right]\leftarrow$$

$$4\left[\begin{array}{c}\textit{solution}\\ \Psi=ce^{-iEt/\hbar}\psi\end{array}\right]$$

$$5\left[-\hbar^2c^2\nabla^2\Psi+m^2c^4=E^2\Psi\right];$$

1 Schrödinger equation; 2 solutions; 3 Klein-Gordon equation; 4 solutions; 5 Hamiltonian eigenvalue problem (criteria of energy); and the end Dirac proposed that for a particle like an electron, (and other spin 1/2 elementary particles like quarks, it turned out,) the square root produces a simple linear combination of the individual square root terms [20]:

$$\sqrt{(mc^2)^2+\sum_{i=1}^{3}(\hat{p}_i)^2}=\alpha_0mc^2+\sum_{i=1}^{3}\alpha_i\hat{p}_ic$$

.

We must also present the potential of Yukawa [33]: $+or-g^2\frac{e^{-\lambda r}}{r}$ where g is a constant with the dimension of electric charge, i.e., cm.3/2 sec.−1, gr.1/2 and with the dimension cm.−1.

Quantum mechanics; Solid state physics [3] are old fundamental knowledge. Engineering knowledge based on fundamental knowledge is presented in [13 and 29]. A long period of time has passed in engineering research (or engineering physics) to the obtained engineering results. Work [7] is also of great importance for the circular economy. With the zone melting method; and the results in [7] are also associated with a significant environmental effect. Engineering studies are important for the phase stability and performance of casting [7]. The use of modern testing tools in [7] and even more so in mathematical experiments based on quantum [**2 and 5**]it will be studied as [7] will be very simplified.

There is a very good methodological coincidence between metal science [8] and solid state physics [11]; there is also a methodological coincidence between [8] and [9]. In [9] it is measured supercooled per melt. Thus develop Stefan's task [1] of taking into account the latent heat of melting connects fundamental theory and engineering research.

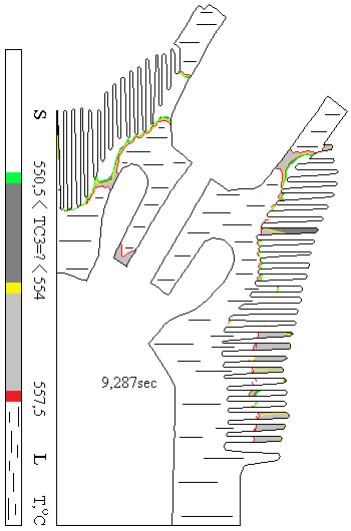


Fig.12. *First order phase transition in complex geometry by finite elements method. This result combine with result of Fig.10 and Classical mathematical methodology on the works [9, 1and40, 38 and 39] and CASTEP [2 and 5] introduce the idea of multi–sale approach/*

Now can use heuristic methods. I [12] a very good study of heuristic rules for the formation of laws was made. A basic cycle [12] is proposed: ***problem–method–solution***, respectively ***hypothesis–conclusions–verification***. Heuristics rules by American physicist Holton and Roller present seven steps for formulating laws [12]. 1. Knowledge of modern science; 2. Close knowledge of natural experience and observation; 3. Reaching the question or problem; 4. Preliminary knowledge of the type of expected solution; 5. Specific concepts that analyze the problem situation; 6. Emergence of a working hypothesis, by trying the simplest hypothesis, various independent checks are made; before accepting an experimental result of significance, never consider the hypothesis as beyond and necessarily reevaluate an reformulate the old knowledge in the light of the new; 7. Design and perform experiments that are more specific and better specific and better controlled.

General consideration of [38] the classical density approach and [39] is good base approaching simultaneous use with CASTEP.

It is well known that mathematics [16, 25, 26, 30, 31] is decisive for science; an area of accumulated knowledge becomes a science after applying mathematics to it. Mathematical physics is also evolving, for example quantum mechanics intervenes in hitherto classical fields [27]. The difficulty in the development of knowledge is the verification of consistency in old knowledge and complex assessments of nuances in knowledge [24, 27, 28, 32, 36, 37].

3. Conclusions - Materials Science Knowledge

Modern materials science requires research to work with complete modern knowledge. Much work is being done in the direction of the theory of maximum unification [34 and 35]: 1. Multi – scale approach. In (34) an approach to the theory of everything is given; based on very large scientific results and the means of mathematics. 2. Synergetic. In [35] the quantum theory of the field in a solid body is used and the theory of excitation is considered. According to Haken, the term synergetic means a union of sciences.

Acknowledgements

This work was supported by the European Regional Development Fund within the OP "Science and Education for Smart Growth 2014 - 2020", Project CoE "National center of mechatronics and clean technologies", № BG05M2OP001-1.001-0008-C08.

Everything written is well known. But the great difficulties come from the need to work very quickly and especially professionally with modern scientific and engineering knowledge.

4. Reference

1. S. Bushev, V. Georgiev, Developing the solution of Stefan's Problem, Comptes rendus de l'Academie bulger des Science, 47, No 3, 1994, 9-12.
2. S. J. Clark, M. D. Segall, C. J. Pickard, P. J. Hasnip, M. I. J. Probert, K. Refson, M. C. Payne, First principles methods using CASTEP, Z. Kristallogr. **220** (2005) 567-570.
3. Ch. Wert, R. Thomson, Physics of Solids, Peace, Moscow (1969). (In Russian)
4. Ch. Kittel, Introduction to Solid State Physics, Fourth Edition, John Wiley and Sons, Inc., Science, Moscow, 1978. (In Rusian)
5. *en.wikipedia.org › wiki › CASTEP* and CASTEP www.castep.org ;
6. Enrico Fermi, Thermodynamics, Prentice-Hall, New York, 1937, second stereotype edition, Publishing House of Kharkov University, 1973. (In Russian)
7. A. Maneva, Thesis of PhD: Study of the structure and properties of castings of aluminum alloys depending on the ratio between primary and secondary alloys, BAS, IMSETCHA, Sofia, 2013. (In Bulgarian)
8. A. Balevski, Metal science, Technics, Sofia, 1962. (In Bulgarian)
9. M. Flemings, Solidification processing, Peace, Moscow, 1977. (In Russian)
10. G. Schulze, Metal physics, Peace, Moscow, 1971.
11. M. Borisov, K. Marinova, Introduction to Solid State Physics Part One, Science and Art, Sofia, 1977. (In Bulgarian)
12. A. Polikarov, Methodology of scientific knowledge, Science and Art, Sofia, 1972.
13. B Crowell, Simpel Nature An introduction to Physics for Engineering and Physical Science Students, www.lightandmatter.com
14. N. V. Vitanov, www.course.quantum-bg.org/
15. J., Ismael, "Quantum Mechanics", *The Stanford Encyclopedia of Philosophy* (Winter 2020 Edition), Edward N. Zalta (ed.), forthcoming URL = https://plato.stanford.edu/archives/win2020/entries/qm
16. E. H. Hristov, Notes Mathematical models in physics, Sofia, 2003. http://www.store.fmi.uni-sofia.bg/fmi/companal/hristov mmfa
17. L. Litov, Quantum physics, https://www.atomic.phys.uni-sofia.bg/lectures; and L. Litov, The Higgs boson or how the mass is born? 2014, https://www.uni-sofia.bg/print/view/full
18. https://www.bg.wikipedia/org/wiki/физика https://www.bg.wikipedia/org/wiki/елементарна_частица https://www.bg.wikipedia/org/wiki/адрон
19. https://bg.wikipedia.org/wiki/Стандартен_модел
20. Leon van Dommelen, Quantum Mechanics for Engineers, https://www.umich.edu/~ners312/courselibrary/dommelen
21. A. Einstein, Relativity: the special and general theory, Henry Holt and Company, New York, 1920.
22. J. Stefan. ¨Uber die verdampfung und die auflˉosung als vorgūange der diffusion. Annalen der Physik und Chemie, 277(12):725–747, 1890.
23. C. Schwarz, *Arch. Für Eisenhüttwesen*, H. 3, p. 139- 148, Sept 1931.O.B.M.
24. . J. C. Baez, M. Stay, Physics, Topology, Logic and Computation: A Rosetta Stone, arXiv:0903.0340v3 [quant-ph] 6 Jun 2009 (not that 0903.4540-1)
25. K. Svozil, Mathematical methods of theoretical physics, Sixth Edition, February 2019. arXiv:1203.4558v8 [math-ph] 1 Feb 2019 (not that 1508.0358-1)
26. M. Lein, Differential Equations in Mathematical Physics, university of Toronto. arXiv:1508.03834v1 [math-ph] 16 Aug. 2015 (not that 1508.03834-1)
27. K. Reuter, C. Stampfl, M. Scheffler, Ab initio atomistic thermodynamics and statistical mechanics of surface properties and functions. arXiv: cond-mat/0404510v1 [cond-mat.mtrl-sci] 21 Apr 2004. not that 0404510v1)
28. E. Scholz, The changing concept of matter in H. Weyl's thought, 1918 – 1930. arXiv:math/0409576v1 [math.HO] 29 Sep 2004 (not that0409576v1_2004)
29. R. E. Smallman, R. J. Bishop, Modern Physical Metallurgy and Materials Engineering, Butterworth-Heinemann, Oxford, 1999. ISBN 0 7506 4564 4
30. V. I. Arnold, Mathematical methods of classical mechanics, Moscow, Science, 1979. (In Russian)
31. B. L. Van Der Wander, Algebra, Moscow, Science, 1976. (In Russian)
32. K. Suto, Derivation of a Relativistic Wave Equation more Profound than Dirac's Relativistic Wave Equation, Applied Physics Research; Vol. 10, No. 6; 2018.
33. H. Yukawa, PTP, 17, 48 1935
34. G. Gremaud, The crystalline ether, third version of the <<popularized>> book, revised and corrected, May 2021.
35. H. Haken, QUNTENFELDTHEORIE DES FESTKÖRPERS, B. G. Teubner, Studgard, 1973. (In Russian)
36. S. H. Simon, Lecture Notes for Solid State Physics, Oxford University, January 9, 2012.
37. A. Neumaier, D. Westra, Classical and quantum mechanics, via Lie algebras, University of Vienna, April 14, 2011.
38. D, Kashchiev, Nucleation, Butterworth-Heinemann, Oxford, 2000. ISBN 0 7505 4682 9
39. I. V. Markov, Crystal Growth for Beginners: Fundamentals crystal growth and epitaxy, 2-nd edition, World Scientific Publishing Co. Pte. Ltd, 2003. ISBN 981-238-245-3
40. S. Bushev, Theoretical model of structure formation in die casting, XXII International scientific technical conference "Foundry 2015", 16-17.04.2015, Pleven, Bulgaria, y. XXIII, ISSUE 3 (166), April 2015. ISSN: 1310 – 3946